



Stockholm  
University

# Master Thesis

Degree Project in  
Geology 60 hp

**U-Pb zircon geochronology and petrogenesis of igneous  
conglomerate clasts and mafic rocks in the NE Yukon-Koyukuk  
basin, Alaska: with implications for their source terrane**

Charlotte Fredriksson



Stockholm 2019

Department of Geological Sciences  
Stockholm University  
SE-106 91 Stockholm

U-Pb zircon geochronology and petrogenesis of  
igneous conglomerate clasts and mafic rocks in the  
NE Yukon-Koyukuk basin, Alaska: with implications for their  
source terrane

**Charlotte Fredriksson**

## Abstract

The formation of the Brooks Range fold and thrust belt in northern Alaska is believed to have occurred when an island arc collided with the North American passive margin in Late Jurassic to Early Cretaceous time. The Brooks Range is flanked to its south by the huge Cretaceous Yukon-Koyukuk basin, filled with thick sedimentary deposits such as conglomerates bearing intermediate-mafic igneous clasts and igneous outcrops of island arc affinity exposed in the centre of the basin. These igneous outcrops belong to the Middle Jurassic and Early Cretaceous Koyukuk Arc terrane, which together with mafic thrust sheets of the oceanic Angayucham terrane and ophiolite klippen associated with the Brooks Range orogen, is believed to represent what is left of the island arc involved in the arc-continent collision. Tectonic interpretations of the Yukon-Koyukuk basin vary from a post-accretionary hinterland basin to a syncollisional forearc basin of the Koyukuk Arc terrane, consequently the basin conglomerate clasts have been inferred to be debris eroded from the Jurassic-Cretaceous arc itself. This investigation into the ages(s), petrogenesis, and tectonic setting(s) associated with igneous conglomerate clasts and mafic rocks from the northeastern part of the Yukon-Koyukuk basin (the Kobuk Koyukuk sub-basin) will test the hypothesis that these clasts are erosional products of the Koyukuk Arc. Whole-rock geochemistry shows that the majority of the clasts have elevated fluid mobile trace elements such as large ion lithophile elements and light rare earth elements relative to non-fluid mobile high field strength elements, which is consistent with subduction zone magmatism and similar to the Koyukuk Arc terrane. The mafic rocks and remaining clasts have chemistry of enriched to normal mid-ocean ridge basalts indicative of spreading-ridge magmatism and consistent with the oceanic Angayucham terrane. U-Pb geochronology of magmatic zircons from the island arc clasts yield Late Triassic ( $213 \text{ Ma} \pm 2$ ) and Early Jurassic ( $195 \text{ Ma} \pm 1$ ) crystallization ages which clearly pre-date the Koyukuk Arc terrane, thus discounting any relationship between them. Geochronology and juvenile isotope chemistry show that the intermediate-mafic igneous clasts in the northeastern Yukon-Koyukuk basin conglomerate record erosion of a Late Triassic to Early Jurassic island arc.

# Table of Contents

<b>1. Introduction</b> .....	<b>1</b>
<b>2. Geological Background</b> .....	<b>4</b>
<b>3. Geological Setting</b> .....	<b>6</b>
3.1 Kobuk Koyukuk sub-basin .....	6
3.2 Koyukuk Arc terrane.....	7
3.3 Angayucham terrane and Brooks Range ophiolite .....	8
3.4 Cretaceous plutonism .....	9
<b>4. Sampling and Petrography</b> .....	<b>10</b>
4.1 Sampling .....	10
4.2 Petrography.....	10
<b>5. Analytical Methods</b> .....	<b>12</b>
5.1 The U-Pb isotopic dating .....	12
5.2 Neodymium isotopes .....	13
5.3 Lead isotopes.....	15
5.4 Isotopic reservoirs .....	15
5.5 Geochronological analyses.....	16
5.6 Isotopic analyses .....	17
5.7 Whole-rock geochemistry .....	18
<b>6. Analytical Results</b> .....	<b>18</b>
6.1 Whole-rock geochemistry .....	18
6.2 Data correlation to neighboring terranes .....	26
6.3 Tectonic environment and magma series.....	26
6.4 U-Pb geochronology.....	28
6.5 Isotope geochemistry .....	29

<b>7. Discussion .....</b>	<b>31</b>
7.1 Age, petrogenesis and tectonic environment.....	31
7.2 Mantle source(s) .....	35
7.3 Correlation(s) to potential sources .....	39
7.4 Triassic-Jurassic island arc magmatism .....	40
7.5 Kobuk Koyukuk Basin source terranes .....	43
<b>8. Conclusions .....</b>	<b>44</b>
<b>Acknowledgements .....</b>	<b>45</b>
<b>References .....</b>	<b>46</b>
<b>Appendices .....</b>	<b>53</b>
A. Thin section descriptions and images.....	53
B. Analytical parameters and conditions (geochronological and isotopic analyses) ...	67
C. Bivariate diagrams and rock classification (whole-rock geochemistry).....	70
D. U-Pb data table (geochronology) .....	72



# 1. Introduction

The geology of Alaska includes numerous geological terranes of diverse origin that were amalgamated by tectonic processes and document the tectonic growth of Alaska. Tectonic accretion began no earlier than the Jurassic (Moore and Box, 2016) and is still active today along the Aleutian subduction zone of southern Alaska where the Pacific plate subducts beneath the North American plate (Figure 1). Large mountain ranges and widespread syn- and post-tectonic sedimentary basins generally constitute the landscape of Alaska. One of several mountain ranges is the east-west trending Brooks Range fold and thrust belt located in northern Alaska (Figure 1) which is thought to be the result of Late Jurassic to Early Cretaceous arc-continent collision (Box & Patton, 1989; Patton & Box, 1989; Miller & Hudson, 1991; Moore and Box, 2016). The Brooks Range orogen is flanked by two sedimentary basins: the syn-orogenic Colville foreland basin to the north and the Yukon-Koyukuk basin to the south (Figure 1). Compared to the well-studied Colville basin, little is known regarding the formation of the Yukon-Koyukuk basin from the regional studies of the late 80ies (e.g., Patton & Box, 1989; Box & Patton, 1989).

In west-central Alaska the Yukon-Koyukuk basin is regionally extensive and broadly triangular in shape with outcrops of Middle Jurassic and Early Cretaceous igneous rocks of the Koyukuk Arc terrane (KAT, see Figure 1) in its central parts (Box & Patton, 1989; Patton et al., 2009). The KAT is a fragment of the intra-oceanic arc terrane that is thought to have collided with the passive North American continental margin in the Mesozoic (Box & Patton, 1989; Patton & Box, 1989; Moore & Box, 2016). Tectonic interpretations of the Yukon-Koyukuk Basin vary widely, from a syn-collisional forearc basin (e.g., Patton & Box, 1989; Till et al., 1993) to a post-accretionary hinterland basin developed due to mid-Cretaceous lithosphere extension (e.g., Miller & Hudson, 1991; Hoiland et al., 2018). The KAT separates the Yukon-Koyukuk basin into two sub-basins, the Kobuk Koyukuk sub-basin to the north and east, and the Lower Yukon sub-basin to the southwest (Nilsen, 1989). This investigation focuses on the Kobuk Koyukuk sub-basin (KKB).

The KKB is bordered by the KAT to the south-southwest and by Proterozoic to Paleozoic continental rocks of the Brooks Range and the Ruby terrane to the north and east, respectively. Rimming the northern and eastern part of the basin is a narrow belt of Late Devonian to Early Jurassic oceanic rocks representing the Angayucham terrane which structurally separates the Brooks Range and Ruby terrane continental rocks from the KKB (Figure 1) (Pallister et al., 1989). Early Jurassic to Middle Jurassic oceanic rocks constitute the Brooks Range ophiolite (Figure 1), preserved in thrust sheets within the Brooks Range orogen (Moore et al., 1993; Harris, 1995; Gottschalk et al., 1998; Box et al., 2019). The Brooks Range ophiolite overlies the Angayucham terrane (Pallister et al., 1989; Harris, 1995) and the terranes differ from each other in both age and geochemical composition, which have led to the suggestion that they do not represent the same ophiolite sequence (Harris, 1995). The

relationship between the Angayucham terrane and Brooks Range ophiolite remains uncertain and diverse interpretations exist.

The KKB is filled with sedimentary deposits eroded from its borderlands. Included in these deposits are fluvial conglomerates bearing clasts of igneous and sedimentary origin, deposited in marine-nonmarine environments (Patton et al., 2009). While most of the mafic debris comes from the oceanic Angayucham terrane, the intermediate – mafic igneous clasts have been inferred to be arc products eroded from the KAT (e.g. Box & Patton, 1989; Patton et al., 2009). The age(s) (fossils and K-Ar dating) and whole-rock chemistry of the KAT were determined and published by Box & Patton (1989), but there are no chemical/geochronological analyses on the clast material that conclusively relate them to the KAT.

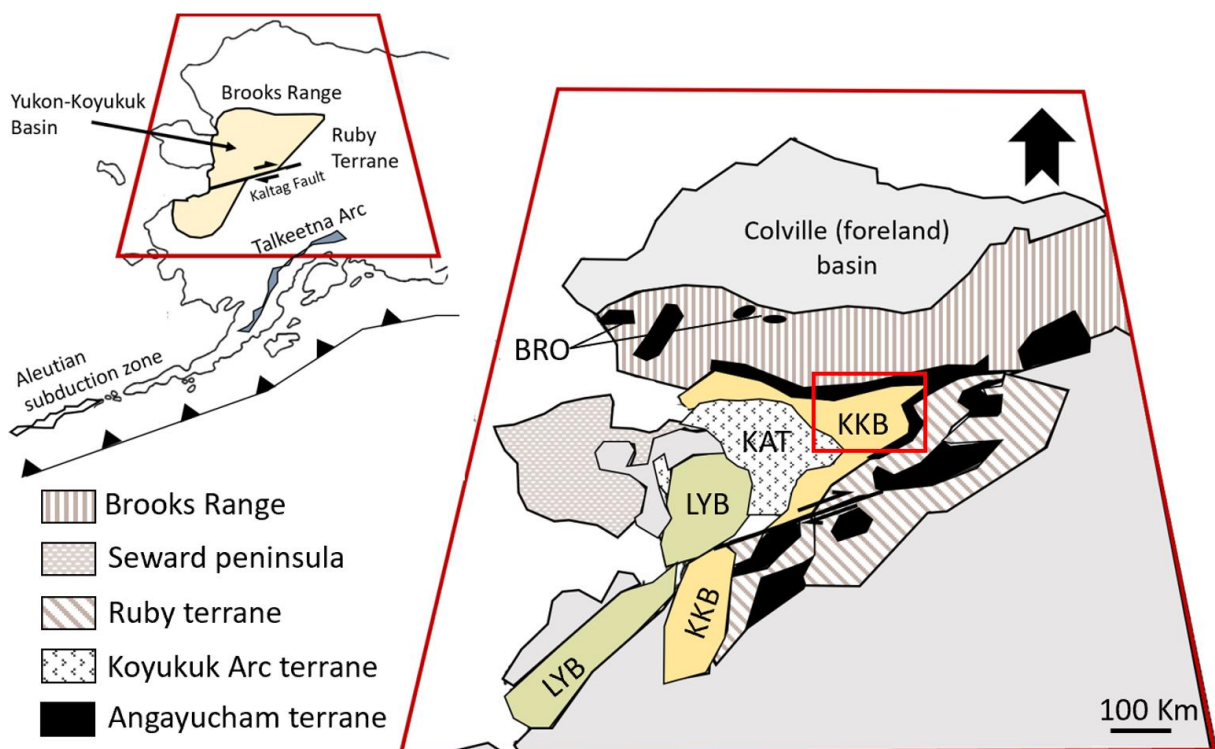


Figure 1. Terrane and basin map of Alaska. Note that only the most easterly part of the Aleutian subduction zone is shown in the inset and that the black triangles indicate the direction of plate subduction (modified from Patton & Box, 1989). Simplified geological map modified from O'Brien et al. (2017) [after Moore and Box (2016)]. The red rectangle marks the location of figure 3 and the sample locations from this study. Abbreviations: **KAT**-Koyukuk Arc terrane; **KKB**- Kobuk Koyukuk sub-basin; **LYB**- Lower Yukon sub-basin; **BRO**- Brooks Range ophiolite.

A recent study by O'Brien et al. (2017) presented detrital and magmatic zircon U-Pb geochronology and Lu-Hf isotope analyses from sandstone and from three gabbroic clasts. All samples in the study were collected from the Cretaceous conglomerate in the north-eastern part of the KKB. O'Brien et al. (2017) concluded that the material represented an eroded Middle Triassic – Late Jurassic (240-160 Ma) juvenile intra-oceanic arc terrane, such as an island arc system developed on oceanic crust with or without minor amounts of crustal/sedimentary input. This raises the question whether the KKB clasts are in fact erosional products of the KAT, or if they originate from an older island arc terrane.

Consequently, diverse interpretations exist regarding both the mechanism of KKB basin formation and the nature of the source terranes to the igneous conglomerate clasts filling it. This study investigates the age(s), petrogenesis and tectonic setting(s) associated with 25 igneous conglomerate clasts and 3 mafic outcrop samples from the north-eastern part of the KKB with the aim to test the hypothesis that the igneous clasts in the Cretaceous conglomerate are erosional products of the Middle Jurassic- Early Cretaceous KAT. Determining the provenance and age(s) of these igneous clasts are important for understanding the tectonic history of the region which is closely related to the formation of the Yukon-Koyukuk basin. The data produced is of great significance for ongoing research into the timing of, and mechanisms for, the Yukon-Koyukuk basin formation. In order to test this hypothesis, the following has been performed:

- 1) U-Pb geochronology of magmatic zircons to determine crystallization age(s) of the clasts.
- 2) Whole-rock geochemistry to distinguish between magma series and tectonic formation environments.
- 3) Preliminary analyses of neodymium and lead isotopic compositions to provide additional petrogenetic information regarding magma source reservoir(s) for distinguishing between oceanic and continental contributions.
- 4) The integration of the geochemical and isotope data with the geochronological data from the clasts and outcrop to provide information about the source terrane(s) from which the igneous samples were derived, thus allowing comparison with existing data from the KAT and neighboring terranes (e.g. Angayucham terrane).

## 2. Geological Background

The formation of the Brooks Range fold and thrust belt initiated when an oceanic island arc collided with the passive margin of North America in the Mesozoic (Patton & Box, 1989; Box & Patton, 1989; Miller & Hudson, 1991; Gottschalk et al., 1998; Hoiland et al., 2018). This resulted in a northward propagating fold and thrust belt composed of several imbricate terranes that were thrust over each other during convergence; together these thrust sheets form a number of east-west trending belts (Gottschalk et al., 1998; Hoiland et al., 2018). From south to north these belts consist of the oceanic rocks of the Angayucham terrane followed by metamorphosed continental margin sediments such as the Greywacke belt, Phyllite belt and Schist belt, and finally the oceanic rocks of the Brooks Range ophiolite comprising the structurally highest allochthon (Figure 2) (Gottschalk et al., 1998; Vogl, 2003).

The arc-continent collision is recorded by widespread high pressure-low temperature (HP/LT) blueschist facies metamorphism in the hinterland of the fold and thrust belt (southern part of the Brooks Range) and in the Ruby terrane to the east (Till et al., 1988; Toro et al., 1996). The HP/LT metamorphic event is especially evident in the Brooks Range Schist belt (Gottschalk et al., 1998) and believed to represent parts of the continental margin that was partially subducted beneath the Angayucham terrane during convergence (Patton & Box, 1989). Large parts of the blueschist rocks have been overprinted by later greenschist facies metamorphism which peaked in the Cretaceous around  $114 \pm 5$  Ma (U-Pb zircon ages by Hoiland et al., 2018). This overprinting has led to difficulties in dating the HP/LT event due to resetting of datable minerals, such as micas (Hoiland et al., 2018). Efforts to date the blueschist facies metamorphism have been made by several authors (e.g. Rb-Sr ages by Armstrong et al., 1986; K-Ar dates by Turner et al., 1979; Ar-Ar plateau age by Christiansen & Snee, 1994) and the HP/LT event is inferred to be Middle to Late Jurassic in age.

Despite agreement regarding how the Brooks Range formed, there are still debates regarding both the timing of convergence and the origin and relationship between the terranes involved. Diverse tectonic models have been proposed to explain the collisional event(s) and the metamorphism across the region (e.g. Box & Patton, 1989; Miller & Hudson, 1991). Some authors (e.g. Box & Patton, 1989; Patton & Box, 1989; Moore and Box, 2016) suggest that the Middle Jurassic to late Early Cretaceous KAT collided with the North American passive continental margin in Late Jurassic to Early Cretaceous time (c. 145-130 Ma, K-Ar mineral ages in Box & Patton, 1989) due to southward subduction (present day coordinates) of the passive continental margin beneath the KAT. Others (e.g. Miller & Hudson, 1991; O'Sullivan et al., 1997; O'Brien et al., 2017) propose that an older Middle Triassic to Late Jurassic (240 – 160 Ma; U-Pb zircon ages in O'Brien et al., 2017) oceanic island arc collided with the North American passive continental margin. Advocates for the latter model suggest that the volcanic history of the KAT is too young (c. 175-118 Ma; K-Ar mineral ages in Box & Patton, 1989) to be compatible with the timing of convergence and compressional deformation in the Brooks

Range, which according to Turner et al. (1979) and Armstrong et al. (1986) initiated prior to 160 Ma. Miller & Hudson (1991) argued for a model that includes a Triassic-Jurassic arc on the basis that there is no known source region for the early syn-orogenic deposits found in the Colville Foreland Basin (northern Brooks Range) (Figures 1 and 2). These deposits include abundant Middle Jurassic volcanic (felsic-intermediate) and plutonic (tonalitic to gabbroic) debris believed to be of arc affinity (Mayfield et al., 1978; Wilbur et al., 1987; Miller & Hudson, 1991). In a study of gabbroic clasts and sandstones from the northeastern KKB O'Brien et al. (2017) concluded that similar detritus represented erosional products of a Middle Triassic – Late Jurassic (240-160 Ma) oceanic arc terrane. Despite the different sampling locations in Miller & Hudson (1991) and O'Brien et al. (2017), these samples display similar ages (Jurassic) and compositions (gabbroic). Both Miller & Hudson (1991) and O'Brien et al. (2017) have suggested that the Triassic-Jurassic oceanic arc was part of an extensive arc-system that included the Talkeetna/Bonanza Arc terrane (207-172 Ma; U-Pb ages in Greene et al., 2006) of southern Alaska (Figure 1). This arc-system was likely active outboard of the western margin of North America during the Early to Middle Jurassic (Plafker et al., 1989; Miller & Hudson, 1991; Greene et al., 2006).

Diverse tectonic models regarding the formation of the Yukon-Koyukuk basin vary from a syn-collisional forearc basin (KKB) to a backarc-basin (Lower Yukon sub-basin) associated with accretion of the KAT (e.g., Patton & Box, 1989; Till et al., 1993; Moore and Box, 2016) to a post-accretionary hinterland basin developed due to mid-Cretaceous lithosphere extension (e.g. Miller & Hudson, 1991; Hoiland et al., 2018). Advocates for the latter model suggest that the formation of the Yukon-Koyukuk basin coincided with the exhumation and greenschist metamorphic overprinting of HP/LT rocks in the southern Brooks Range, and that this event was due to an episode of large magnitude mid-Cretaceous lithosphere extension. This event is also believed to have caused normal faulting of obducted oceanic thrust sheets such as the Angayucham terrane and Brooks Range ophiolite. Opponents (e.g. Till et al., 1993) suggest that the timing of the extensional event overlapped with a period of contractional deformation and that the evidence for the proposed large magnitude extension is restricted to the southern flank of the Brooks Range. The numerous tectonic models used to explain the formation of the Yukon-Koyukuk basin (recently summarized by Hoiland et al., 2018) include northward- or southward-directed subduction and a combination of the two (subduction polarity reversal). In addition, the pre-collisional position of the allochthonous thrust sheets in the Brooks Range (such as the Angayucham terrane and Brooks Range ophiolite) relative to the subduction system remains disputed - did they develop in a forearc or backarc tectonic setting?

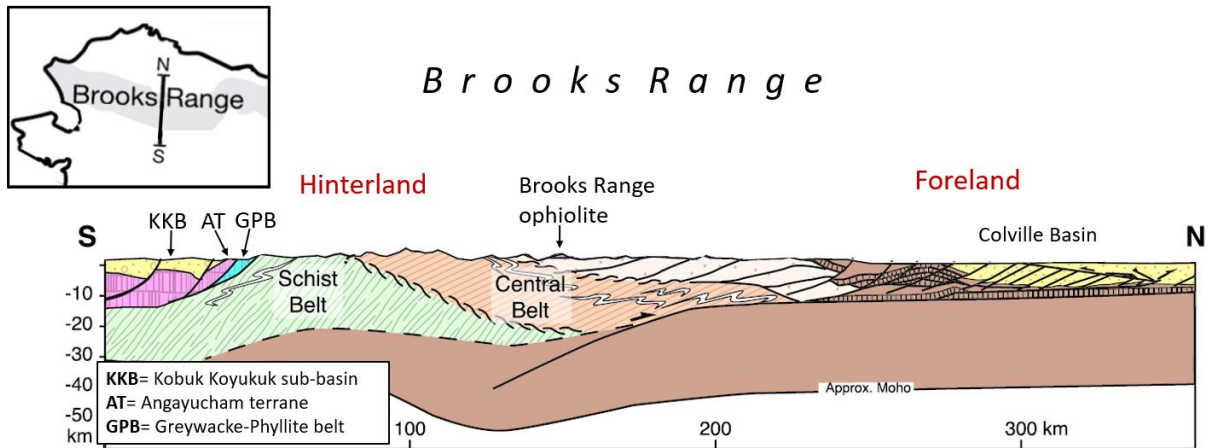


Figure 2. Simplified cross section of the Brooks Range fold and thrust belt (after Hoiland et al., 2018). The inset shows the line of the section. Note the relative positions of the accreted terranes with the KKB in the south relative to the oceanic rocks of the Angayucham terrane and the more distal Brooks Range ophiolite in the central part of the section.

### 3. Geological Setting

#### 3.1 Kobuk Koyukuk sub-basin

Samples for this study were collected from the northeastern part of the KKB, the northern sub-basin of the Yukon-Koyukuk basin (Figures 1 and 3). The stratigraphy of the KKB consists of several Cretaceous sedimentary units named and described by Patton et al. (2009) (Figure 3). The lower part of the sequence (Kvg) comprises mudstone and fine-grained conglomeratic graywacke with mafic-intermediate volcanic and intrusive clasts, along with small amounts of chert, felsic plutonic rocks and metamorphic debris. Fossils of late Early Cretaceous marine mollusks supports a marine depositional environment (Patton et al., 2009). Kvg is widely distributed throughout the whole KKB (Figure 3).

Kvg is structurally overlain by the more scattered and less abundant Kmc unit which occurs along the northern and southeastern margins of the KKB (Figure 3). Kmc consists of a poorly sorted conglomerate with clasts varying in size from pebble to cobble (Patton et al., 2009). The conglomerate clasts are mainly mafic volcanic - intrusive rocks, chert and some smaller amounts of felsic plutonic rocks together with quartz and limestone, all embedded in a graywacke-mudstone groundmass. The conglomerate indicates that the material was transported in a fluvial setting, however, marine mollusks found in some parts of the unit might suggest that the conglomerate was later deposited in a marine environment (Patton et al., 2009).

The Kvg and Kmc units are subsequently overlain by the structurally highest unit (Kqc) which, like Kmc, is positioned along the northern and southeastern margins of the KKB (Figure 3) (Patton et al., 2009; O'Brien et al., 2017). The Kqc unit comprises a well-sorted conglomerate

with clasts of quartz and metamorphosed greywacke in a groundmass mixture of quartz- and mica-rich metamorphic detritus. Clasts of limestone schist, chert and metamorphosed mafic igneous material, are also present but in minor amounts. The presence of plant fossils and coal indicates that these fluvial sediments were deposited in a non-marine environment. The sedimentary sequence of the KKB is believed to reflect a great amount of erosion that progressively exposed the deeper parts of the over-thrusted terranes, thus recording the unroofing history of the Brooks Range and Ruby Terrane (e.g., Patton et al., 2009; O'Brien et al., 2017).

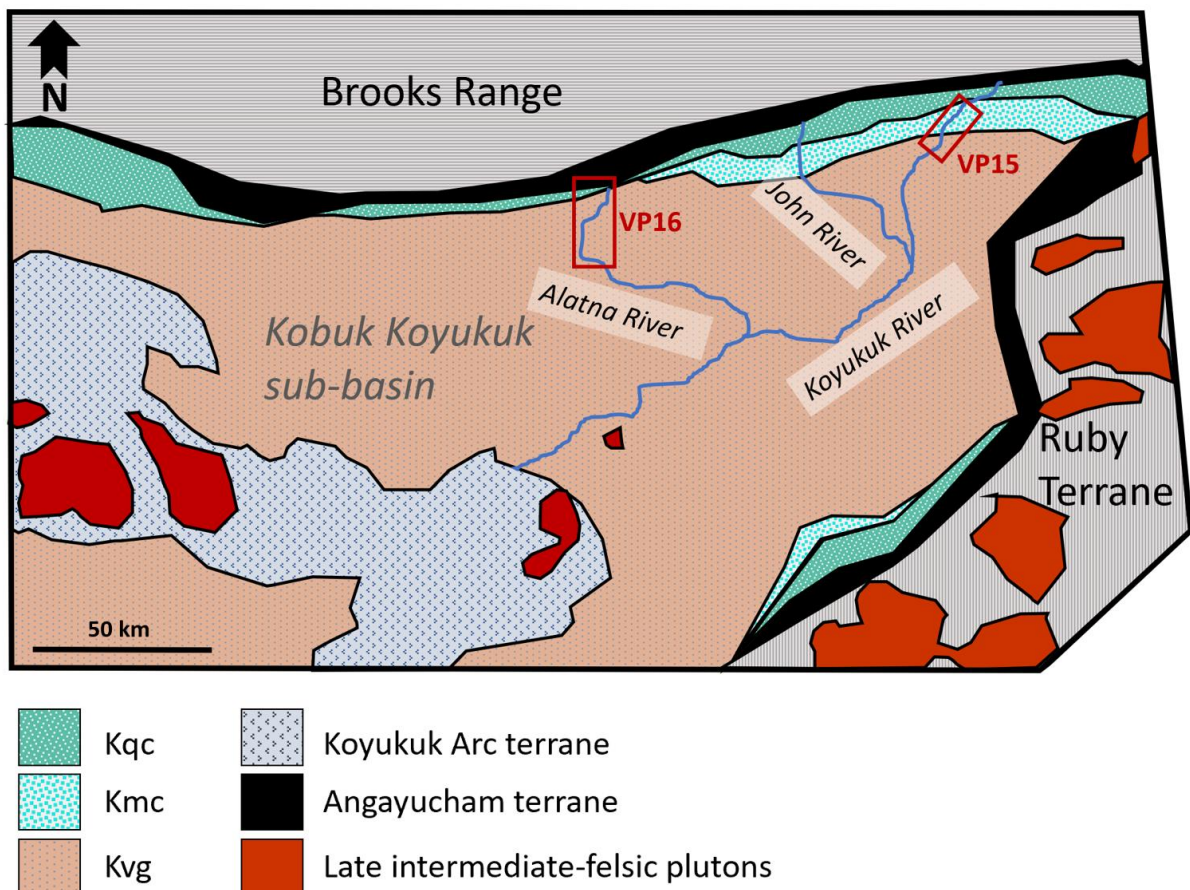


Figure 3. Simplified geological map of the northeastern part of the KKB (after Patton et al., 2009). Sample traverse locations along the Alatna River (VP16) to the west and along the Koyukuk River (VP15) to the east are represented by red rectangles. Note the KKB geological units relative to adjacent terranes.

### 3.2 Koyukuk Arc terrane

The KAT consists of Mesozoic plutonic, volcanic and volcanoclastic rocks that crop out in an arcuate structural high in the center of the Yukon-Koyukuk basin (Box & Patton, 1989; Patton et al., 2009). An initial study of the KAT made by Box & Patton (1989) recognized four stratigraphic units: Unit 1 includes pre-Middle Jurassic (fossil ages) basaltic flows, diabase, gabbro, and ultramafic intrusive rocks together with limestone and chert; Unit 2 consists of

Middle - Late Jurassic (173 - 154 Ma, K-Ar mineral ages) intermediate to felsic plutonic rocks; Early Cretaceous (137 - 125 Ma, K-Ar mineral ages) mafic to intermediate volcanic flows, volcanoclastic and minor intrusive rocks constitute Unit 3; Unit 4 includes Early Cretaceous (123-118 Ma, K-Ar mineral ages) mafic to intermediate volcanic and volcanoclastic rocks. According to Box & Patton (1989) units 2, 3 and 4 preserve whole-rock chemistry indicative of island arc subduction zone magmatism. That is - enrichment in fluid-mobile large ion lithophile elements (LILEs) (e.g. Sr, K, Rb and Ba) and light rare earth elements (LREEs) (e.g. La and Ce), and a relative depletion in high field strength elements (HFSEs) (e.g. Nb, Ta, Hf, Zr and Ti). The ultramafic to mafic igneous rocks of Unit 1 lack the HFSE depletion relative to LILEs and LREEs displayed by the other units and according to Box & Patton (1989) rocks of unit 1 have geochemistry suggestive of a backarc or seamount setting. Unit 3 was further divided into six sub-Groups (3a-3f) based on their geographic position and similarities in rare earth element patterns. LREE to heavy REE (HREE) ratios increase between the sub-units, from low ratios (c. 1) and flat chondrite normalized REE patterns of sub-unit 3a, to higher ratios (>1) and steeper chondrite normalized REE patterns of sub-unit 3f. The KAT includes members of the four most common magma series: tholeiitic (units 1, 3a and 3b), calc-alkaline (units 2, 3c, 3d and 3e) and alkaline to shoshonitic (units 3f and 4). All rocks of the KAT have been affected by secondary hydrothermal alteration (Box & Patton, 1989).

### 3.3 Angayucham terrane and Brooks Range ophiolite

The Late Devonian to Early Jurassic Angayucham terrane comprises several thrust sheets consisting of rocks typical of the upper part of an ophiolite section, such as pillow basalt, diabase, basaltic tuff and radiolarian chert (Pallister et al., 1989; Patton & Box, 1989; Harris, 1995). This group of faulted basaltic rocks dips steeply towards and beneath the Yukon-Koyukuk basin (Patton & Box, 1989) and has been variably affected by low grade metamorphism such as prehnite-pumpellyite to lower greenschist facies (Pallister et al., 1989). In a study of the east-west trending belt of the Angayucham terrane in the southern Brooks Range, Pallister et al. (1989) recognized three units based on poorly constrained fossil ages: Jurassic basalt, Triassic basalt and Paleozoic (mixture between Paleozoic and Mesozoic ages) basalt. Major and trace element classification of these units showed them to be mostly tholeiitic (a few were alkaline) with geochemistry varying between N-MORB and E-MORB. The Triassic basalt which occupies the central part of the Angayucham belt has relatively flat chondrite normalized REE patterns (LREE to HREE ratios c. 1), whereas the Paleozoic(?) basalt (north of the Triassic unit) and the Jurassic basalt (south of the Triassic unit) both have LREE enriched patterns (LREE to HREE ratios >1). None of the units record island arc chemistry and Pallister et al. (1989) suggested the Angayucham terrane to represent either a seamount or an oceanic island.

In contrast to the Angayucham terrane, the Brooks Range ophiolite (Figures 1 and 2) mainly consists of intrusive rocks typical of a lower ophiolite section, such as dunite, harzburgite, wehrlite, layered cumulate gabbro and isotropic gabbro (Box & Patton, 1989; Patton & Box,

1989; Harris, 1995). The Brooks Range ophiolite forms the structurally highest part of the orogen and is comprised of six klippen - fragments that are left after erosion of a once extensive thrust sheet (Harris, 2004). Studies of the Brooks Range ophiolite indicate geochemical characteristics between island arc and MORB (Harris, 1995). This arc-MORB transitional chemistry has been recognized from volcanic rocks in modern forearc settings, such as the Indonesian Banda arc (Harris, 1992; Harris, 1995). Thus, it was suggested that the Brooks Range ophiolite represents the obducted forearc region of the oceanic island arc (KAT?) that collided with North America (Patton & Box, 1989; Harris, 1995).

New data from Box et al. (2019) include geochemical and geochronological (U-Pb zircon ages) results from the Brooks Range ophiolite. Their results show that basaltic rocks, diabase dikes and intermediate-felsic intrusions cutting the ophiolite have island arc chemistry. The intermediate-felsic intrusions which cross-cut the older basaltic rocks and diabase dikes gave ages of  $161 \pm 2$  to  $164 \pm 3$  Ma and are not co-genetic with the basaltic rocks and diabase dikes. The later has trace element chemistry typical of island arc tholeiites with relatively flat chondrite normalized REE patterns, while the former have steeper and more enriched REE patterns. Due to the similar ages, Box et al. (2019) also suggested that the Brooks Range ophiolite might be the forearc to the KAT. As no new analyses exist for the Angayucham terrane, its relationship to the Brooks Range ophiolite remains uncertain.

### 3.4 Cretaceous plutonism

Significant amounts of KKB sediment originates from the southern part of the Brooks Range and the northeast-southwest trending Ruby terrane. The majority of the Ruby terrane consists of metasedimentary rocks similar to those of the Brooks Range (O'Brien et al., 2017). Late Early to early Late Cretaceous (118–98 Ma, U-Pb and K-Ar ages; Miller, 1989; Roeske et al., 1995, 1998) intermediate to felsic plutons intrude all units of the Ruby terrane (including the Angayucham terrane) and parts of the Yukon-Koyukuk basin including the KAT, but not the Brooks Range (Figure 3). According to Miller (1989) the plutonic rocks of the Ruby terrane differ from those that intrude the Yukon-Koyukuk basin in both composition and age. The chemical composition of the plutons intruding the Ruby terrane indicate that these were likely products of melting the continental crust. The plutons intruding the Yukon-Koyukuk basin, as opposed to those intruding the Ruby terrane, have compositions that suggest melting of either oceanic mantle material or melting of a more evolved version of such material. Despite originating from different sources, both plutonic suites are calc-alkaline (Miller, 1989; Arth et al., 1989). According to Miller (1989) the Ruby plutons are about 16-20 Ma older than those in the Yukon-Koyukuk basin.

## 4. Sampling and Petrography

### 4.1 Sampling

The samples used in this study (25 conglomerate clasts and 3 outcrop samples) were collected from six sampling sites in the northeastern part of the Kobuk Koyukuk sub-basin by Prof. Victoria Pease in the years 2015 and 2016. The 2016 samples are preceded by “VP16” and were collected from five sites (22, 23, 24, 25 and 26) along the Alatna River (Figure 3). The 2015 samples are preceded by “VP15” and were sampled from a site near the Koyukuk River (Figure 3). The samples collected at site VP16-22 (a, b and c) were sampled from mafic outcrops. The outcrop samples consist of basaltic flows and pillow basalt (Figure 4A). All VP16 samples from site 23-26 are conglomerate clasts collected from the Kvg unit (Figure 4B). Likewise, the VP15 samples also consist of conglomerate clasts but these were collected from the Kmc unit.



Figure 4. **A)** Nice pillow basalt outcrop with white calcite filled amygdalae. **B)** Conglomerate clast from the Kvg unit. Note the size of the clast which is typical for most of the collected clast samples.

### 4.2 Petrography

Except for a few felsic samples, most samples are of mafic to intermediate composition and intrusive or hypabyssal, with medium to coarse grained phaneritic textures; however, there are also a few extrusive samples with porphyritic or fine grained aphanitic textures. In thin-section, the samples have similar primary mineralogy dominated by plagioclase ( $\pm$  alkali-feldspar in the more evolved samples), pyroxene,  $\pm$  hornblende and iron oxide(s). All samples have been affected to some degree by low-grade hydrothermal alteration documented by secondary replacement minerals such as chlorite, calcite, epidote, actinolite, prehnite, serpentine and sericite/saussurite. Veins and amygdalae in the volcanic samples are commonly filled with secondary calcite and/or chlorite (Figure 4A). Thin-section descriptions and microphotographs of the samples are provided in Appendix A.

The mafic Alatna River outcrop samples (22a, -b, -c) are represented by pillow basalt, basaltic flow and gabbro. The pillow basalt sample (VP16-22c) consists of skeletal pyroxene and plagioclase crystals indicating extremely rapid cooling and disequilibrium. The basalt has an intergranular texture with calcite filled and flow oriented amygdales. The gabbroic sample displays a sub-ophitic texture of plagioclase laths partly enclosed by fractured pyroxene (CPX) (Figure 5A). Plagioclase, pyroxene and iron oxide(s) constitute the primary mineralogy for the outcrop samples, and the secondary hydrothermal alteration mineralogy includes calcite, chlorite and sericite.

The conglomerate clasts from the Koyukuk River (VP15-10, -11, -12 and -13) are all mafic and consist of basalt and microgabbro (dolerite). The basalts vary from pyroxene phenocrysts in a fine grained matrix to sub-ophitic with plagioclase laths partially enclosed by pyroxene (CPX), interstices are commonly filled with secondary chlorite and calcite. Some of the basalts have skeletal plagioclase laths indicating extremely rapid cooling and disequilibrium (Figure 5B). Microgabbros are equigranular with an intergranular texture of randomly oriented plagioclase laths and pyroxene occupying the interstices. Pyroxene is commonly replaced by secondary actinolite (uralitization), chlorite and/or serpentine to varying degrees. Iron oxides(s) are common in all samples.

The conglomerate clasts sampled along the Alatna River include mafic to felsic compositions, with most of them being mafic. Intrusive to hypabyssal samples dominate and commonly consist of plagioclase, pyroxene (CPX), hornblende and iron oxide(s). Uralitization of pyroxene and sericitization/saussuritization of plagioclase and alkali-feldspar are common (Figure 5C). Hornblende is occasionally replaced by chlorite and/or actinolite. Biotite is completely replaced by chlorite. Felsic minerals such as alkali-feldspar and quartz are common in the more evolved samples. The volcanic samples include basalt to andesite and are generally porphyritic with a trachytic matrix of flow-oriented plagioclase microlites. The porphyritic basalts have large pyroxene (CPX) phenocrysts and the andesites have phenocrysts of plagioclase and/or alkali-feldspar. Two of the samples have enclaves with mineralogy distinct from the groundmass indicating that they might represent mixing of magmas. One sample is volcanoclastic and consists of brecciated sub-angular felsic igneous rock fragments mainly visible under the polarizing microscope (Figure 5D). All conglomerate samples have been affected by low grade hydrothermal alteration, some more than others.

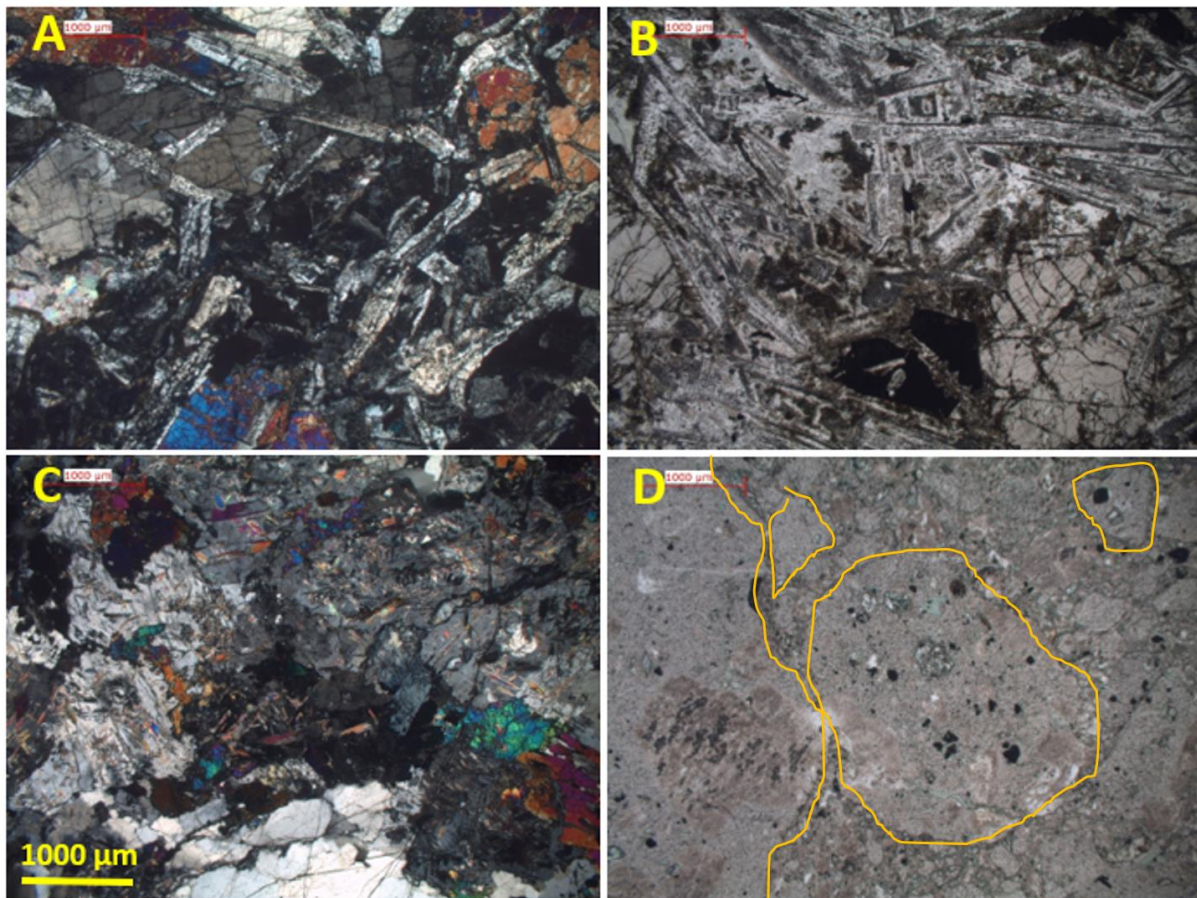


Figure 5. Thin section microphotographs using plane polarized light (PPL) and cross polarized light (XPL) of **A)** Basaltic outcrop sample displaying a sub-ophitic texture of randomly oriented plagioclase laths that are partly enclosed by larger pyroxene grains - CPX with 1<sup>st</sup> to 2<sup>nd</sup> order birefringence (XPL); **B)** Koyukuk River basalt showing skeletal plagioclase (PPL); **C)** granodiorite with quartz and saussurite (epidote) alteration of feldspar (XPL); **D)** volcaniclastic breccia with sub-angular felsic rock fragments (PPL).

## 5. Analytical Methods

### 5.1 The U-Pb isotopic dating

The U-Pb dating method is based on the decay of the radioactive parent isotopes  $^{238}\text{U}$  and  $^{235}\text{U}$  to the stable and radiogenic daughter isotopes  $^{206}\text{Pb}$  and  $^{207}\text{Pb}$ , respectively. Each of the uranium parent isotopes have their separate decay chain including several intermediate daughter isotopes with a stable lead isotope as the end product. The decay chain of  $^{238}\text{U}$  is called the uranium series and the decay chain of  $^{235}\text{U}$  is referred to as the actinium series. By measuring the amount of the uranium parent isotope and the amount of the lead daughter isotope in a mineral and assuming a closed system, it is possible to calculate the time it has taken the parent to produce the radiogenic daughter (Faure & Mensing, 2005). For an igneous rock with a single-stage cooling history this calculated time would approximate when the mineral being analyzed crystallized from its melt. The age calculation is based on secular equilibrium, meaning that the parent isotope decreases at the same rate as the daughter

isotope is being produced. Secular equilibrium is achieved when a mineral has remained in a closed system since it crystallized, i.e.- no loss/gain of daughter product (Faure & Mensing, 2005). A date can be calculated for either the uranium and/or actinium series using the isochron equations (Equations 1 and 2, respectively). The isochron equations are based on the individual decay constants ( $\lambda$ ) of each series, the initial lead ratio ( $i$ ) and the measured radiogenic lead isotopes and parent uranium isotopes normalized to stable and non-radiogenic lead ( $^{204}\text{Pb}$ ), also called 'common' lead. When analyzing zircon with a negligible amount of initial lead in its crystal structure, Equations 1 and 2 can be simplified to Equations 3 and 4 (assuming that a correction for common lead can be made) (Schoene, 2014).

$$\left(\frac{^{206}\text{Pb}}{^{204}\text{Pb}}\right) = \left(\frac{^{206}\text{Pb}}{^{204}\text{Pb}}\right)_i + \left(\frac{^{238}\text{U}}{^{204}\text{Pb}}\right) (e^{\lambda t} - 1) \quad (1)$$

$$\left(\frac{^{207}\text{Pb}}{^{204}\text{Pb}}\right) = \left(\frac{^{207}\text{Pb}}{^{204}\text{Pb}}\right)_i + \left(\frac{^{235}\text{U}}{^{204}\text{Pb}}\right) (e^{\lambda t} - 1) \quad (2)$$

$$\left(\frac{^{206}\text{Pb}}{^{238}\text{U}}\right) = (e^{\lambda t} - 1) \quad (3)$$

$$\left(\frac{^{207}\text{Pb}}{^{235}\text{U}}\right) = (e^{\lambda t} - 1) \quad (4)$$

If the independent dates calculated for the uranium and actinium series are the same, then the date is said to be concordant and will plot on the concordia curve in a concordia diagram. Discordant dates are those that plot outside the concordia curve. Discordance indicate that the mineral has been affected by some form of open system behaviour, such as loss of lead and/or uranium (Schoene, 2014). Loss of lead or intermediate daughter isotopes are related to radiation damages in the crystal structure, while loss of uranium is commonly associated with chemical weathering due to the mobility of uranium under oxidising conditions (Faure & Mensing, 2005). Due to elemental interference of atomic mass 204 the ICP-MS will measure both  $^{204}\text{Hg}$  and  $^{204}\text{Pb}$ . By measuring mass 202 which corresponds to  $^{202}\text{Hg}$  and assuming a natural ratio of  $^{202}\text{Hg}/^{204}\text{Hg}$  of 4.35, it is possible to calculate how much of mass 204 is represented by  $^{204}\text{Hg}$ . The amount of common lead is then calculated by subtracting the  $^{204}\text{Hg}$  from the total 204 mass that has been measured (Morrison and Murphy, 2006).

## 5.2 Neodymium isotopes

The REEs group of trace elements share similar chemical and physical properties and generally form ions with a +3 charge. The REEs samarium (Sm) and neodymium (Nd) are incompatible elements and are preferentially fractionated into melts rather than solid phases (referring to mantle minerals). The lower atomic number and larger atomic radius of Nd makes it slightly more incompatible than Sm, resulting in Nd being more fractionated into the liquid phase than Sm. Thus, an evolved rock that has gone through magma differentiation, such as a granite in the continental crust, will initially have lower Sm/Nd ratio than a less evolved/depleted rock, such as a mantle peridotite or a basalt of the oceanic crust (Faure & Mensing, 2005).

Sm and Nd are related to each other by the decay of the radioactive isotope  $^{147}\text{Sm}$  to the stable radiogenic daughter isotope  $^{143}\text{Nd}$ . This means that the amount of radiogenic  $^{143}\text{Nd}$  in a rock increases over time as  $^{147}\text{Sm}$  decays. Radiogenic  $^{143}\text{Nd}$  is commonly measured against non-radiogenic  $^{144}\text{Nd}$ , and with time as  $^{147}\text{Sm}$  decays, the  $^{143}\text{Nd}/^{144}\text{Nd}$  ratio will increase. Thus, depleted mantle rocks and mantle derived melts that have higher concentrations of samarium relative to neodymium will end up with a higher  $^{143}\text{Nd}/^{144}\text{Nd}$  ratio than evolved rocks such as granites (in which samarium is less abundant relative to neodymium). The  $^{143}\text{Nd}/^{144}\text{Nd}$  ratio can therefore be used as a good indicator for involvement of crustal material in basaltic genesis. Involvement of crustal material could be input of sediment into subduction zones or assimilation of continental crust by intruding magmas.  $^{143}\text{Nd}/^{144}\text{Nd}$  ratios are commonly compared to the present isotope ratio of the chondrite uniform reservoir (CHUR) which represents the average composition of chondrites (estimated by DePaolo & Wasserburg, 1976). CHUR is thought to represent the neodymium composition of the Earth's initial mantle and assumes that the early Earth had the same composition as chondrites (Ellam, 2016). Due to the very small difference of incompatibility between Sm and Nd, the variation in  $^{143}\text{Nd}/^{144}\text{Nd}$  ratios between different rock types and mantle reservoirs is generally small. Thus, to facilitate the interpretation of the data the  $^{143}\text{Nd}/^{144}\text{Nd}$  ratio is commonly transformed to the epsilon neodymium notation ( $\epsilon\text{Nd}$ ) as defined by DePaolo & Wasserburg (1976).  $\epsilon\text{Nd}$  is calculated using Equation 5 (Faure & Mensing, 2005).

$$\epsilon^0(\text{Nd}) = \left[ \frac{(^{143}\text{Nd}/^{144}\text{Nd})_R^0 - (^{143}\text{Nd}/^{144}\text{Nd})_{\text{CHUR}}^0}{(^{143}\text{Nd}/^{144}\text{Nd})_{\text{CHUR}}^0} \right] \times 10^4 \quad (5)$$

where  $O$  = present day and  $R$  = rock/mineral.

A sample may have an  $\epsilon\text{Nd}$  value that is either positive, negative or zero. A value of zero would equal the present-day CHUR  $^{143}\text{Nd}/^{144}\text{Nd}$  ratio. A positive value means that the sample is enriched in radiogenic  $^{143}\text{Nd}$  and indicates a depleted mantle origin with a high Sm/Nd ratio, such as rocks of the oceanic crust. A negative  $\epsilon\text{Nd}$  value is typical of more evolved rock types such continental crust which originates from partial melts with a low Sm/Nd ratio.

The  $^{147}\text{Sm}/^{144}\text{Nd}$  enrichment relative to CHUR is called the fractionation factor ( $f^{\text{Sm}/\text{Nd}}$ ) and is calculated using Equation 6. It is the  $^{147}\text{Sm}/^{144}\text{Nd}$  analogue for  $\epsilon\text{Nd}$ . A positive value indicates a depleted mantle source with a Sm/Nd ratio higher than CHUR and a negative value indicates an enriched mantle or crustal source with Sm/Nd ratio lower than CHUR (DePaolo and Wasserburg, 1976).

$$f^{\text{Sm}/\text{Nd}} = \left[ \frac{(^{147}\text{Sm}/^{144}\text{Nd})_R^0}{(^{147}\text{Sm}/^{144}\text{Nd})_{\text{CHUR}}^0} \right] - 1 \quad (6)$$

where  $O$  = present day and  $R$  = rock/mineral.

The  $\epsilon Nd$  and  $f^{Sm/Nd}$  can be used to calculate the  $\epsilon Nd_t$  at a time  $t$  ( $\epsilon Nd_t$ ), where  $t$  is generally the age of the rock and will thus represent the initial  $\epsilon Nd$  value of the sample.  $\epsilon Nd_t$  is calculated using **Equation 7** (DePaolo and Wasserburg, 1976).

$$\epsilon Nd_t = \epsilon Nd^0 - Q_{Nd} f^{Sm/Nd} \times t \quad (7)$$

where  $0 = \text{present day}$  and  $Q_{Nd} = 25.09 \text{ Ga}^{-1}$  when  $^{146}\text{Nd}/^{144}\text{Nd}$  is normalized to 0.7219.

### 5.3 Lead isotopes

Lead occurs as non-radiogenic  $^{204}\text{Pb}$  (common lead) and several radiogenic isotopes. The radiogenic lead isotopes include  $^{206}\text{Pb}$ ,  $^{207}\text{Pb}$  and  $^{208}\text{Pb}$  which are produced by the radioactive decay of  $^{238}\text{U}$ ,  $^{235}\text{U}$  and  $^{232}\text{Th}$ , respectively. Due to the large ionic radius of uranium and thorium, these elements are generally incompatible within mantle solid phases, resulting in their fractionation into the melt/fluid phase(s). Thus, they commonly end up enriched in the more evolved silica-rich rock types of the continental crust. Enrichment of lead is commonly measured as a ratio of radiogenic lead ( $\text{Pb}^*$ ) to common lead ( $\text{cPb}$ ) ( $^{206}\text{Pb}/^{204}\text{Pb}$ ,  $^{207}\text{Pb}/^{204}\text{Pb}$  and  $^{208}\text{Pb}/^{204}\text{Pb}$ ) (Faure, 1986). Due to the radioactive decay of the parent isotopes uranium and thorium, sources enriched in these elements become progressively enriched in radiogenic lead with time consequently leading to increased  $\text{Pb}^*/\text{Pb}_c$  ratios. Low uranium and thorium concentrations in the mantle makes the lead isotopic system a sensitive indicator of crustal or sedimentary input in mantle derived melts and they are important for petrogenetic studies of basaltic rocks (Todd et al., 2015). It has been discovered that contamination of non-magmatic lead is common in rock samples and that contamination can be caused by both natural processes such as seawater alteration or by man-made processes such as sampling and laboratory preparation (e.g., McDonough & Chauvel, 1991; Todd et al., 2015). Contamination can result in ambiguous results and false interpretations, and despite high reproducibility the results can be inaccurate (McDonough & Chauvel, 1991; Todd et al., 2015). It has therefore been suggested that acid leaching should be applied to samples before the isotope analyses. Acid leaching is a technique to remove non-magmatic lead contamination from a sample without removing the sample's primary lead signature (Todd et al., 2015).

### 5.4 Isotopic reservoirs

The isotope ratios (e.g.  $^{143}\text{Nd}/^{144}\text{Nd}$ ,  $^{206}\text{Pb}/^{204}\text{Pb}$ ,  $^{207}\text{Pb}/^{204}\text{Pb}$  and  $^{208}\text{Pb}/^{204}\text{Pb}$ ) of a sample have implications for the isotopic characteristics of the source region from which the melt was extracted (Rollinson, 1993). Due to the small mass difference between these pairs of radiogenic isotopes they do not fractionate during magma differentiation (e.g. crystal fractionation and partial melting) and therefore preserve the isotopic character of the mantle source region (Faure & Mensing, 2005). Zindler & Hart (1986) identified four principal mantle reservoirs believed to define mantle compositional end-members. They suggested that the

isotopic compositions seen in mantle derived rocks on Earth today can be explained by a variety of mixing processes between these end-members. These four end-members include: depleted mantle (DM), high- $\mu$  (HIMU), enriched mantle type I (EMI) and enriched mantle type II (EMII). Their characteristics are presented in Table 1.

Table 1. Isotopic mantle reservoirs.

	$^{147}\text{Sm}-^{143}\text{Nd}$	$^{238}\text{U}-^{206}\text{Pb}$	$^{235}\text{U}-^{207}\text{Pb}$	$^{232}\text{Th}-^{208}\text{Pb}$	
<b>Depleted mantle</b>	High Sm/Nd; high $^{143}\text{Nd}/^{144}\text{Nd}$ (positive epsilon)	Low U/Pb; low $^{206}\text{Pb}/^{204}\text{Pb}$ (c. 17.2-17.7)	Low U/Pb; low $^{207}\text{Pb}/^{204}\text{Pb}$ (c. 15.4)	Th/U=2.4±0.4; low $^{208}\text{Pb}/^{204}\text{Pb}$ (c. 37.2-37.4)	Presumed depleted upper mantle. Typically the dominant source of many MORBs.
<b>HIMU</b>	Intermediate Sm/Nd (<0.51282)*	High U/Pb; high $^{206}\text{Pb}/^{204}\text{Pb}$ (>20.8)	High U/Pb; high $^{207}\text{Pb}/^{204}\text{Pb}$	High Th/Pb	Mantle source enriched in U and Th relative to Pb which has lead to high Pb*/Pbc ratios due to long periods of incubation in the mantle.
<b>EM I</b>	Low Sm/Nd; $^{143}\text{Nd}/^{144}\text{Nd}$ <0.5112*	Low U/Pb; $^{206}\text{Pb}/^{204}\text{Pb}$ = (17.6-17.7)	Low U/Pb; $^{207}\text{Pb}/^{204}\text{Pb}$ = (15.46-15.49)	Low Th/Pb; $^{208}\text{Pb}/^{204}\text{Pb}$ = (38.0-38.2)	Recycled altered oceanic crust and marine sediment.
<b>EM II</b>	Low Sm/Nd; $^{143}\text{Nd}/^{144}\text{Nd}$ = (0.511-0.5121)*	High $^{207}\text{Pb}/^{204}\text{Pb}$ and $^{208}\text{Pb}/^{204}\text{Pb}$ at a given $^{206}\text{Pb}/^{204}\text{Pb}$			Recycled altered oceanic crust and terrigenous sediment.

Notes – Table adapted from Rollinson (1993) showing the characteristics of the isotopic mantle reservoirs with present day isotope ratios shown in parentheses (values from Zindler & Hart, 1986).

\* Normalized to  $^{146}\text{Nd}/^{144}\text{Nd} = 0.7219$ .

## 5.5 Geochronological analyses

A total of eleven samples (eight conglomerate clasts and three outcrop samples) were prepared for U-Pb geochronology using igneous zircon and/or baddeleyite (Table 2). The first steps of sample preparation included crushing, milling, heavy mineral separation using a Wilfley water table and removal of magnetic minerals (no heavy liquid separation was needed). All samples yielded zircon of varying size, but none yielded baddeleyite. Due to the small size of the zircon crystals in most samples, only three samples (VP16-23e, VP16-25a and VP16-26f) with large zircon crystals (>20 $\mu\text{m}$ ) were mounted and analysed via LA-ICP-MS. The zircons from each of these three samples were handpicked onto a glass disc and mounted in epoxy resin (left for 48 h to solidify). The mount was then polished to expose the centres of the zircon grains and subsequently carbon coated before scanning electron microscopy (SEM) and cathodoluminescence (CL) imaging. CL images (acceleration voltage of 15 kV) were taken in order to study the internal structures of the zircon grains and select analytical locations within grains for laser ablation-inductively coupled plasma-mass spectrometric (LA-ICP-MS)

analyses. Polishing, carbon coating and CL imaging (SEM) were performed at the Swedish Museum of Natural History. U-Pb geochronology was performed using a New 193 nm ArF excimer laser coupled to a Thermo XSeries II quadrupole ICP-MS at the Petro Tectonics analytical facility in the Department of Geological Sciences, Stockholm University. A spot size of 20  $\mu\text{m}$  was used for the reference materials and samples. Analytical parameters and conditions are presented in the Appendix B. The Plešovice zircon natural reference material was used for instrument calibration. The international standard FC-5z from the Duluth Gabbro was used to monitor instrument performance. The U-Pb data were reduced using Iolite with the VisualAge add-on (Petrus & Kamber, 2012) running on Igor Pro. The routine for downhole fractionation correction of Paton et al. (2010) was also applied. Ambiguous analyses were excluded by filtering the samples using following criteria: discordance (>10%), age precision (>10% Ma), and common lead ( $^{204}\text{Pb}$ ) content (>100 counts per second). The common lead content was obtained by assuming a  $^{202}\text{Hg}/^{204}\text{Hg}$  natural ratio of 4.35. Due to the low common lead ( $^{204}\text{Pb}$ ) content in the samples no correction was performed. All U-P data plots have been made using Isoplot 3.75 (Ludwig, 2012).

## 5.6 Isotopic analyses

Analyses of neodymium isotopes were made for 12 samples, including ten conglomerate clasts and two outcrop samples (Table 2). The same 12 samples were also analysed for lead isotopes in a pilot study. Analytical parameters and conditions are presented in Appendix B.

The neodymium isotope analyses were performed on a Thermo Scientific TRITON thermal ionization mass spectrometer (TIMS) at the Laboratory of Isotope Geology, Swedish Museum of Natural History. Total spiking with a mixed  $^{149}\text{Sm}/^{150}\text{Nd}$  spike was used and concentrations and ratios were reduced assuming exponential fractionation. Samarium concentrations were determined in multi-collector static mode on rhenium double filaments and neodymium was run in static mode on double rhenium filaments using rotating gain compensation. Samarium and neodymium ratios were corrected for mass fractionation by the normalizing factors  $^{147}\text{Sm}/^{148}\text{Sm} = 1.33386$  and  $^{146}\text{Nd}/^{144}\text{Nd} = 0.7219$ , respectively. The method was validated by the measurement of the standard reference materials La Jolla and BCR-2. The external precision for  $^{143}\text{Nd}/^{144}\text{Nd}$  as judged from values for La Jolla standard was 18 ppm. Accuracy correction was applied since the mean  $^{143}\text{Nd}/^{144}\text{Nd}$  ratio was  $0.511867 \pm 09$  ( $n=12$ ). Consequently, measured  $^{143}\text{Nd}/^{144}\text{Nd}$  ratios have been brought in accordance with reference standard measurements by subtraction of 0.3 epsilon units.

The lead isotope analyses were performed on a Nu plasma (II) multi-collector (MC) ICP-MS using an Aridus II desolvator introduction system at Vegacenter, Swedish Museum of Natural History. Samples were measured at  $\sim 30$  ppb in 0.3M  $\text{HNO}_3$  + 10 ppb thallium (Tl). Thallium was added to the sample solution to correct the measured ratios for mass fractionation.

Uptake rate was  $\sim 100 \mu\text{L}/\text{min}$  and uptake of sample measurements was 80 sec with a wash out time of 100 sec. Before every analysis the baselines were measured for 60 sec in order to

subtract them from individual mass signals during data reduction. Each analysis consisted of 2 blocks of 25 cycles integrating 10 sec per cycle.

All values have been normalized to the NBS-981 standard (n=12) that was measured repeatedly during the analyses and were used to evaluate the accuracy and external reproducibility of the measurements (relative to published standard values from Todt et al., 1996). As leaching was not performed the possibility of lead contamination (from seawater alteration and/or sampling processing) should be considered and care must be taken when interpreting the lead isotope data.

## 5.7 Whole-rock geochemistry

Whole-rock geochemical analyses and loss on ignition (LOI) were performed on all 28 samples (25 conglomerate clasts and three outcrop samples) (Table 2). The analyses were performed in the spring of 2017 and the data were split between three bachelor theses (e.g., Fredriksson, 2017; Kubiak, 2017 and Nilsson, 2017). For this master thesis the entire raw data set has been re-processed and re-interpreted.

Major and minor element analyses were performed on a Rigaku ZSX Primus II X-ray Fluorescence (XRF) spectrometer on homogenised fused glass discs. Matrix matched international reference materials AGV-2, BCR-2 and RGM-1 were used as internal standards and run every 10<sup>th</sup> sample to confirm instrument performance. Trace element analyses were performed on homogenised fused glass (XRF discs) using LA-ICP-MS. NIST 612 glass was used as the external reference material (primary standard) and BCR-2 and SARM-1 reference materials were used as secondary standards to confirm instrument performance. For a more detailed method description see Fredriksson (2017). The XRF and LA-ICP-MS analyses were done at the Petro Tectonics analytical facility.

# 6. Analytical Results

## 6.1 Whole-rock geochemistry

Whole rock geochemical results are given in Table 3 and bivariate plots of the major oxides versus SiO<sub>2</sub> are presented in Appendix C. The LOI analysis record volatile contents varying between 1.5 – 8.1 wt.%. LOI values are consistent with the occurrence of H<sub>2</sub>O and CO<sub>2</sub>-rich alteration minerals, such as micas and calcite, but also with primary hydrous minerals such as hornblende. Silica varies from 49-53 wt.% with some analyses as low as 45 wt.% and a few analyses as high as 55 to 70 wt.%. Al<sub>2</sub>O<sub>3</sub> varies between 15-20 wt.% and displays no covariation with increasing SiO<sub>2</sub> content. Fe<sub>2</sub>O<sub>3</sub>, MgO and CaO contents decrease with increasing SiO<sub>2</sub> content and vary between 3-14 wt.%, 1-10 wt.% and 3-16 wt.%, respectively. Both TiO<sub>2</sub> and MnO define decreasing trends with increasing SiO<sub>2</sub> and vary between 0.28-2.54 wt.% and 0.05-0.25 wt.%, respectively. P<sub>2</sub>O<sub>5</sub> is generally below detection and is not discussed further. Na<sub>2</sub>O

shows an increasing but scattered trend with increasing SiO<sub>2</sub> and varies between 2-6 wt.%. K<sub>2</sub>O is generally low (0.04-3.0 wt.%) very scattered and shows no covariation with SiO<sub>2</sub>.

Due to mobility of several of the major elements during alteration (displayed by the scatter in K<sub>2</sub>O and Na<sub>2</sub>O vs SiO<sub>2</sub>), the classification and discrimination diagrams used in this study are based on elements that are relatively immobile during alteration (except under the most

*Table 2. Sample summary including geological unit, sample location and analyses performed.*

<b>Sample</b>	<b>Map Unit</b>	<b>Coordinates</b>		<b>Whole-rock chemistry</b>	<b>Geochron.</b>	<b>Isotope</b>
VP15-10	kmc	67°04.037'N	150°58.54'W	yes	yes	yes
VP15-11	kmc	67°04.037'N	150°58.54'W	yes	no	no
VP15-12	kmc	67°04.037'N	150°58.54'W	yes	yes	no
VP15-13	kmc	67°04.037'N	150°58.54'W	yes	yes	yes
VP16-22a	Outcrop	67°00.865'N	153°21.53'W	yes	yes	yes
VP16-22b	Outcrop	67°00.865'N	153°21.53'W	yes	yes	no
VP16-22c	Outcrop	67°00.865'N	153°21.53'W	yes	yes	yes
VP16-23a	kvg	66°56.569'N	153°24.933'W	yes	no	yes
VP16-23c	kvg	66°56.569'N	153°24.933'W	yes	no	no
VP16-23d	kvg	66°56.569'N	153°24.933'W	yes	yes	no
VP16-23e	kvg	66°56.569'N	153°24.933'W	yes	yes	no
VP16-23g	kvg	66°56.569'N	153°24.933'W	yes	no	yes
VP16-24a	kvg	66°56.322'N	153°26.385'W	yes	no	yes
VP16-24b	kvg	66°56.322'N	153°26.385'W	yes	no	yes
VP16-24c	kvg	66°56.322'N	153°26.385'W	yes	no	no
VP16-24d	kvg	66°56.322'N	153°26.385'W	yes	no	yes
VP16-24e	kvg	66°56.322'N	153°26.385'W	yes	no	no
VP16-24f	kvg	66°56.322'N	153°26.385'W	yes	yes	no
VP16-25a	kvg	66°55.687'N	153°30.33'W	yes	yes	no
VP16-25b	kvg	66°55.687'N	153°30.33'W	yes	no	no
VP16-25c	kvg	66°55.687'N	153°30.33'W	yes	no	no
VP16-25d	kvg	66°55.687'N	153°30.33'W	yes	no	yes
VP16-25f	kvg	66°55.687'N	153°30.33'W	yes	no	no
VP16-25g	kvg	66°55.687'N	153°30.33'W	yes	no	no
VP16-26a	kvg	66°52.005'N	153°35.531'W	yes	no	no
VP16-26b	kvg	66°52.005'N	153°35.531'W	yes	no	yes
VP16-26e	kvg	66°52.005'N	153°35.531'W	yes	no	no
VP16-26f	kvg	66°52.005'N	153°35.531'W	yes	yes	yes

Table 3. Major and minor element chemistry.

Sample ID	VP15-10	VP15-11	VP15-12	VP15-13	VP16-22a	VP16-22b	VP16-22c
	Micro-gabbro	Basalt	Basalt	Micro-gabbro	Gabbro	Basalt	Basalt
<i>Major Elements, Anhydrous (wt. %)</i>							
SiO <sub>2</sub>	49.2	47.1	50.2	51.5	49.0	45.9	48.7
Al <sub>2</sub> O <sub>3</sub>	14.8	18.2	16.6	15.8	14.9	15.7	16.2
Fe <sub>2</sub> O <sub>3</sub>	12.44	8.39	14.20	11.87	12.11	13.42	9.80
MgO	6.4	6.8	3.8	5.7	7.0	8.0	9.4
CaO	11.1	16.3	8.2	8.7	10.0	10.8	12.0
Na <sub>2</sub> O	2.9	1.9	4.0	4.1	4.1	3.6	2.9
K <sub>2</sub> O	0.76	0.12	0.64	0.41	0.06	0.04	0.04
TiO <sub>2</sub>	2.0	0.9	2.1	1.6	2.5	2.2	0.7
MnO	0.23	0.18	0.20	0.23	0.19	0.22	0.20
P <sub>2</sub> O <sub>5</sub>	<0.112	<0.027	<0.089	<0.086	<0.111	<0.108	<0.019
LOI (wt. %)	2.3	3.9	3.0	2.5	3.7	5.8	3.7
<i>Trace Elements (ppm)</i>							
Ba	132	31.4	566	337	445	153	65.3
Cr	140	132	43	69	142	522	343
Cs	0.47	0.08	3.87	0.33	1.17	0.28	0.08
Cu	107	13	26	17	79	112	174
Hf	3.49	1.05	2.91	2.54	2.79	3.05	0.97
Nb	9.7	1.1	6.3	5.5	11.6	19.4	1.2
Ni	40	39	16	29	53	194	119
Pb	6.51	0.46	0.88	1.49	1.64	0.74	0.27
Rb	16.4	1.42	12.0	7.81	5.74	0.42	0.35
Sc	43.1	40.3	31.7	39.9	40.9	39.0	47.4
Sr	605	284	409	168	246	130	36.8
Ta	0.56	0.07	0.38	0.31	0.67	1.11	0.08
Th	1.17	0.11	0.67	0.64	0.81	1.11	0.09
U	0.36	0.07	0.33	0.32	0.28	0.26	0.03
V	290	203	505	309	336	300	257
Y	30.8	16.1	31.6	31.0	26.6	21.7	16.2
Zr	141	37.3	107	95.3	107	116	31.7
La	10.3	1.88	7.28	6.60	8.27	9.36	1.24
Ce	24.4	5.18	17.7	16.1	19.5	21.7	3.71
Pr	3.61	0.95	2.76	2.55	2.97	3.27	0.66
Nd	17.1	5.2	14.0	13.2	14.8	15.9	3.9
Sm	5.1	1.9	4.4	4.2	4.4	4.5	1.5
Eu	1.87	1.16	1.66	1.48	1.69	1.69	0.69
Gd	5.3	2.5	4.9	4.8	4.8	4.5	2.1
Tb	0.892	0.419	0.831	0.792	0.765	0.716	0.424
Dy	5.8	2.9	5.7	5.5	5.0	4.4	3.0
Ho	1.21	0.642	1.25	1.16	1.04	0.848	0.648
Er	3.5	1.8	3.6	3.4	3.0	2.4	2.0
Tm	0.49	0.26	0.52	0.49	0.41	0.30	0.29
Yb	3.33	1.86	3.64	3.33	2.78	2.13	2.04
Lu	0.44	0.25	0.51	0.47	0.38	0.29	0.29

VP16-23a	VP16-23c	VP16-23d	VP16-23e	VP16-23g	VP16-24a	VP16-24b	VP16-24c	VP16-24d	VP16-24e	VP16-24f
Micro-gabbro	volcaniclastic breccia	Micro-gabbro	Diorite	Grano-diorite	Gabbro	Gabbro	Mixed basalt?	Micro-gabbro	Basalt	Gabbro
51.9	63.1	50.8	52.8	69.8	51.2	56.5	50.6	51.3	51.0	52.6
17.1	16.0	16.6	18.9	14.7	17.1	15.0	16.4	16.1	18.5	15.7
10.96	6.39	12.45	9.62	3.49	10.17	11.38	11.93	8.73	8.95	10.55
6.2	3.1	6.1	2.8	1.5	6.5	4.4	6.1	7.7	8.1	6.4
8.0	3.2	7.4	9.0	4.8	10.6	5.9	8.5	10.9	6.8	8.8
3.5	4.6	4.1	3.6	4.3	2.5	4.2	4.6	2.3	4.7	3.4
0.48	2.69	0.63	1.94	0.80	0.76	1.27	0.71	2.14	0.31	1.02
1.5	0.6	1.6	0.9	0.4	1.0	1.1	0.8	0.6	1.3	1.1
0.24	0.17	0.25	0.15	0.14	0.19	0.23	0.22	0.19	0.22	0.22
<0.112	<0.138	<0.088	0.22	<0.102	<0.056	<0.088	<0.124	<0.046	<0.108	<0.073
4.0	3.6	4.8	6.0	3.0	4.0	1.5	3.3	3.2	3.1	3.8
267	433	330	344	81.7	312	552	146	790	175	386
158	61	96	75	156	133	58	101	176	191	126
0.23	0.20	0.34	0.74	0.19	0.30	0.37	0.13	0.47	0.21	0.53
51	26	130	84	15	48	16	131	97	72	74
2.64	3.03	2.34	2.67	3.87	1.29	2.20	1.55	0.96	2.75	1.99
3.1	2.9	2.3	3.6	2.0	1.2	2.4	1.6	1.5	1.8	2.2
56	9	41	24	25	48	18	37	59	108	39
1.51	2.08	2.13	1.62	1.43	1.14	0.67	2.39	1.29	1.99	0.90
7.46	47.7	10.5	34.3	14.1	16.9	25.9	9.87	44.9	4.32	21.7
40.5	14.8	45.6	31.7	15.7	40.3	35.5	43.8	39.9	34.3	42.1
293	240	359	443	267	373	410	1363	430	196	402
0.19	0.24	0.16	0.22	0.15	0.08	0.16	0.10	0.08	0.14	0.14
0.46	2.05	0.33	1.88	1.57	0.46	1.17	0.99	0.56	0.30	0.50
0.21	1.28	0.16	0.72	0.62	0.19	0.40	0.53	0.15	0.28	0.18
273	146	358	298	99.7	271	284	332	191	240	270
23.9	19.5	23.3	20.5	24.2	16.5	24.5	16.8	12.0	27.5	23.6
103	109	82.3	94.0	142	46.4	80.9	54.1	36.6	114	73.7
5.07	10.8	5.11	13.4	8.89	4.37	7.03	9.15	4.76	4.89	5.27
12.8	23.9	12.7	29.4	19.3	9.81	15.6	19.6	9.75	13.6	12.3
1.99	3.45	2.11	4.36	2.96	1.48	2.29	2.88	1.36	2.28	1.90
10.5	15.8	11.0	20.1	13.7	7.5	11.2	14.0	6.6	11.7	9.9
3.4	3.9	3.4	4.9	3.7	2.4	3.5	3.7	1.9	4.1	3.2
1.36	1.18	1.32	1.35	1.10	0.96	1.12	1.29	0.73	1.46	1.20
3.7	3.5	3.9	4.3	3.9	2.6	3.8	3.5	2.1	4.3	3.8
0.708	0.543	0.735	0.658	0.589	0.436	0.649	0.509	0.339	0.728	0.622
4.9	3.4	4.9	4.0	4.0	3.0	4.3	3.2	2.2	4.9	4.4
1.03	0.715	1.05	0.799	0.833	0.655	0.915	0.663	0.452	1.05	0.927
3.0	2.1	2.9	2.2	2.5	1.9	2.8	1.8	1.3	3.2	2.8
0.42	0.31	0.42	0.30	0.36	0.27	0.42	0.27	0.18	0.47	0.44
3.20	2.31	3.04	2.28	2.72	1.80	2.72	1.82	1.28	3.21	2.67
0.44	0.35	0.43	0.33	0.42	0.25	0.42	0.25	0.18	0.44	0.38

VP16-25a	VP16-25b	VP16-25c	VP16-25d	VP16-25f	VP16-25g	VP16-26a	VP16-26b	VP16-26e	VP16-26f
Grano-diorite	Andesite	Basalt	Granite	Diorite	Basalt	Andesite	Gabbro	Gabbro	Diorite
67.2	60.8	45.3	69.7	58.3	50.9	54.6	50.8	49.8	58.0
17.4	14.6	19.8	16.5	15.8	17.1	18.7	16.2	17.1	15.0
3.76	6.08	12.62	2.76	10.52	13.16	7.37	11.84	10.47	6.03
0.9	3.0	9.9	1.1	4.4	3.4	4.6	6.0	7.3	6.7
4.9	8.4	8.3	3.0	5.4	8.3	4.9	9.7	10.4	10.0
4.3	5.8	2.2	5.7	3.1	4.3	5.7	3.2	2.7	3.0
1.07	0.40	0.86	0.84	0.71	0.47	3.03	0.71	1.03	0.62
0.3	0.6	0.7	0.3	1.2	2.0	0.8	1.4	0.9	0.4
0.12	0.22	0.24	0.05	0.25	0.24	0.21	0.22	0.18	0.15
<0.048	<0.091	<0.069	<0.039	0.25	<0.16	<0.084	<0.098	<0.037	<0.013
1.6	8.1	6.3	1.5	4.4	6.9	4.7	1.8	1.9	1.6
336	81.5	155	382	186	272	455	646	1729	141
174	65	468	173	112	44	113	104	127	315
0.20	0.13	0.19	0.18	0.07	0.61	0.06	0.87	0.97	0.13
10	11	62	97	207	117	6	155	156	12
3.44	2.38	1.08	3.24	3.10	3.36	2.63	2.08	1.18	1.11
3.1	1.8	0.5	10.3	2.7	3.7	1.7	2.0	1.0	1.0
13	14	191	22	25	16	37	38	51	79
2.15	1.35	1.55	2.63	3.08	3.15	3.77	1.27	0.76	1.16
29.8	9.93	11.2	20.4	7.41	7.96	28.7	12.9	19.2	10.8
7.1	21.3	38.3	8.1	33.2	41.3	31.8	42.9	43.7	35.5
612	124	323	566	260	328	147	405	294	313
0.19	0.13	0.03	0.75	0.17	0.22	0.13	0.12	0.07	0.06
1.49	0.94	0.25	5.52	1.15	0.92	0.72	0.37	0.27	0.54
0.76	0.66	0.18	2.29	0.63	0.35	0.33	0.18	0.12	0.30
45.3	130	229	59.7	285	464	179	332	275	134
15.1	16.7	15.8	10.0	35.0	28.4	22.7	25.4	15.8	10.3
144	87.7	37.6	135	99.7	119	90.0	73.7	39.8	42.5
13.2	4.79	5.32	19.0	13.9	9.28	7.67	6.19	2.80	3.84
26.0	9.83	11.2	30.6	33.2	20.3	17.8	14.2	6.69	7.51
3.51	1.87	1.83	3.28	5.01	3.14	2.75	2.25	1.11	0.952
15.1	9.5	9.7	12.0	24.5	15.5	13.3	11.7	5.9	4.2
3.2	2.8	2.8	2.3	6.5	4.6	3.5	3.7	2.0	1.3
1.09	0.78	1.01	0.77	1.77	1.70	0.93	1.36	0.83	0.51
2.8	2.7	3.0	2.0	6.6	4.9	3.8	4.1	2.5	1.5
0.412	0.436	0.458	0.285	1.07	0.914	0.644	0.720	0.435	0.268
2.5	3.0	3.0	1.6	6.5	5.8	4.2	4.9	3.0	1.9
0.527	0.658	0.628	0.329	1.38	1.22	0.878	1.01	0.646	0.396
1.6	2.0	1.8	1.0	3.8	3.6	2.7	2.9	1.8	1.2
0.24	0.30	0.24	0.15	0.52	0.51	0.40	0.39	0.26	0.16
1.91	2.13	1.71	1.13	3.78	3.72	2.79	2.86	1.77	1.30
0.31	0.30	0.24	0.17	0.55	0.52	0.41	0.41	0.26	0.19

Notes - Major and minor elements were determined by XRF and are presented as wt.% oxide. International reference standards were used to evaluate the quality of the measurements. Accuracy for the major oxides was generally better than 1% error except for MnO and P2O5 that were better than 2% and 10% error, respectively. The precision for the major oxides was better than 1% RSD. Trace elements were analysed by LA-ICPMS and are presented in parts per million (ppm). Accuracy for the trace elements were better than 10% error, except for Ni and Hf that were better than 13% error. Precision for the trace elements was generally within 1-5% RSD. Structurally bound H2O was determined by loss on ignition analysis (LOI). Abundances preceded by '<' are below detection limits.

extreme conditions) such as  $\text{TiO}_2$  and some trace elements (Ta, Nb, Hf, Zr, Th, Y and the REEs). Rock classification based on whole-rock geochemistry uses the updated Zr/ $\text{TiO}_2$  vs Nb/Y classification diagram of Pearce (1996) for altered volcanic rocks, originally after Winchester & Floyd (1977) (Appendix C). All samples plot in the sub-alkaline field in the Zr/ $\text{TiO}_2$  vs Nb/Y classification diagram and vary in composition from gabbro to granite for the intrusive samples and from basalt to andesite for the extrusive samples; however, gabbro and microgabbro samples dominate.

Since the Zr/ $\text{TiO}_2$  vs Nb/Y classification diagram was originally constructed for extrusive and high level intrusive volcanic rocks (including volcanoclastic rocks with minor amounts of non-volcanogenic material) (Winchester & Floyd, 1977), extra care was taken during the classification of the intrusive samples. The intrusive samples were additionally plotted on a total alkali vs silica (TAS) diagram of Cox et al. (1979) adapted by Wilson (1989) (Appendix C). Both classification diagrams give similar results.

The incompatible trace elements of the samples are plotted in multi-element and REE diagrams (Figures 6 and 7) normalized to the normal mid-ocean ridge basalt (N-MORB) of Sun & McDonough (1989). The samples divide into Groups based on similarities in trace element patterns and immobile element abundances. Note that samples indicating the possibility of physical contamination (e.g., petrographic magma mixing/volcanoclastics) are plotted as dotted lines or with X symbols. Notation of the three samples (VP16-23e, VP16-25a and VP16-26f) analyzed for U-Pb geochronology are included in all diagrams.

**Group 1** (black symbols) includes the Alatna River outcrop samples (VP16-22) and Koyukuk River clasts (VP15). The samples have variable trace element contents and have been subdivided into Group 1a and Group 1b.

**Group 1a** (VP16-22a, VP16-22b, VP15-10, VP15-12, VP15-13) show variably LILE enrichment (e.g. Sr, K, Rb and Ba;  $\text{Rb}_{\text{NMORB}} = 3\text{-}29$ ) (Figure 6A). The samples in Group 1a are similar to enriched-MORB (E-MORB). Generally, the samples lack HFSE depletion (e.g. Ta, Nb) relative to the LREEs (La and Ce) [ $(\text{Nb}/\text{La})_{\text{NMORB}} = 0.9\text{-}2.2$ ] and all have low LILE/HFSE ratios [ $(\text{Rb}/\text{Nb})_{\text{NMORB}} = 0.1\text{-}7.9$ ] (Figure 6A). Group 1a is enriched in LREE relative to HREE [ $(\text{La}/\text{Yb})_{\text{NMORB}} = 2.4\text{-}5.4$ ] and in middle REE (MREE) relative to HREE [ $(\text{Sm}/\text{Yb})_{\text{NMORB}} = 1.4\text{-}2.5$ ] (Figure 6B). Their geochemical signature is summarized in Table 4.

**Group 1b** (VP15-11 and VP16-22c) differs from Group 1a in having trace element patterns similar to, but slightly more depleted than, N-MORB (normalized abundances  $<1$ ). Group 1b

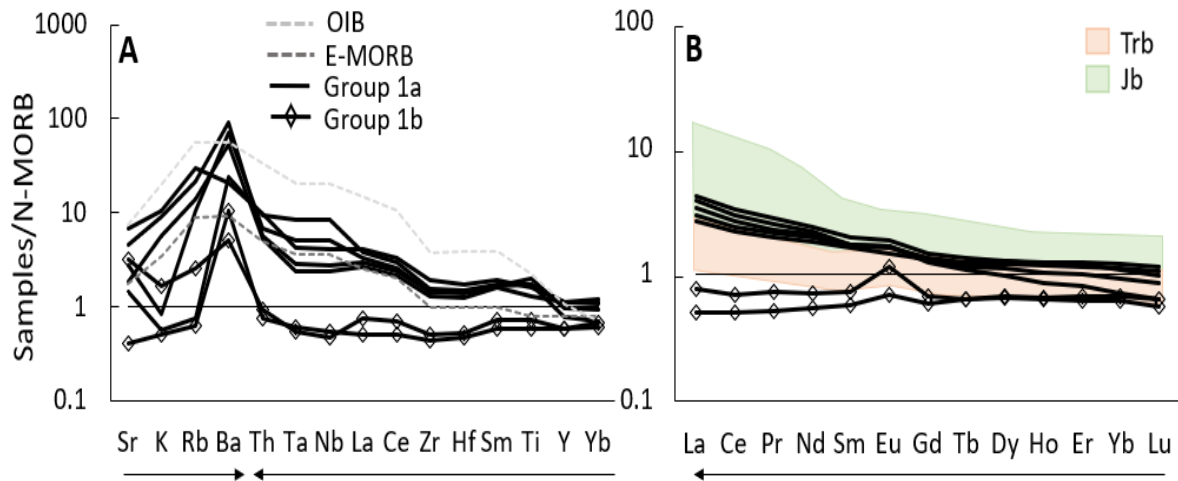


Figure 6. Group 1 (Alatna outcrop and Koyukuk River samples) trace element chemistry normalized to N-MORB (after Sun & McDonough, 1989). **A**) Multi-element diagram with LILEs on the left and HFSEs on the right (after Pearce, 1983). Black arrows on the abscissa indicate direction of increasing incompatibility. Note that N-MORB normalized trace element compositions of OIB and E-MORB are plotted for reference (dashed lines) (OIB and E-MORB reference values from Sun & McDonough, 1989). **B**) REE composition of Group 1 samples (relative to N-MORB). Note the Triassic and Jurassic basalts of the Angayucham terrane (from Pallister et., 1989) are shown for reference. **Trb** = Triassic basalt, **Jb**= Jurassic basalt.

have LILE concentrations similar to N-MORB ( $Rb_{NMORB} = 1-3$ ) (Figure 6A). Group 1b shows no distinct HFSE depletion (e.g. Ta, Nb) relative to the LREEs (La and Ce) [ $(Nb/La)_{NMORB} = 0.6-1.1$ ] and has low LILE/HFSE ratios [ $(Rb/Nb)_{NMORB} = 1.2-5.4$ ] (Figure 6A). Group 1b is generally depleted in LREE relative to HREE [ $(La/Yb)_{NMORB} = 0.7-1.2$ ] and shows no distinct depletion nor enrichment in the MREE relative to HREE [ $(Sm/Yb)_{NMORB} = 0.9-1.2$ ] (Figure 6B). Their geochemical signature is summarized in Table 4.

**Group 2** includes the Alatna river clast samples (VP16-24a, VP16-24c, VP16-24d, VP16-25c, VP16-26e and VP16-26f). Group 2 is enriched in the fluid-mobile LILEs (e.g. Sr, K, Rb and Ba;  $Rb_{NMORB} = 12-39$ ) and all samples show an HFSE depletion (e.g. Ta, Nb) relative to the LREEs (La and Ce) [ $(Nb/La)_{NMORB} = 0.1-0.7$ ] and elevated LILE/HFSE ratios [ $(Rb/Nb)_{NMORB} = 26-122$ ] (Figure 7A). Group 2 displays slightly depleted REE abundances relative to N-MORB (normalized abundances  $<1$ ) but generally show a small enrichment in the LREEs (La and Ce) (Figure 7B). Group 2 have  $(LREE/HREE)_N$  ratios varying from slightly enriched to enriched [ $(La/Yb)_{NMORB} = 1.9-6.1$ ] and slightly enriched  $(MREE/HREE)_N$  ratios [ $(Sm/Yb)_{NMORB} = 1.1-2.3$ ]. Their geochemical signature is summarized in Table 4.

**Group 3** includes the Alatna river clast samples (VP16-23a, -23d, -24e, -24f, -25f, -25g and -26b). Group 3 is enriched in the fluid-mobile LILEs ( $Rb_{NMORB} = 18-80$ ) and depleted in the HFSEs relative to the LREEs [ $(Nb/La)_{NMORB} = 0.1-0.4$ ] and has elevated LILE/HFSE ratios [ $(Rb/Nb)_{NMORB} = 9-41$ ] (Figure 7A). The samples have MREE and HREE abundances that are similar, but slightly enriched, relative to N-MORB (Figure 7C). Group 3 samples have  $(LREE/HREE)_N$  ratios varying

from slightly enriched to enriched  $[(La/Yb)_{NMORB} = 1.9-4.5]$  and slightly enriched  $(MREE/HREE)_N$   $[(Sm/Yb)_{NMORB} = 1.2-2.0]$ . Their geochemical signature is summarized in Table 4.

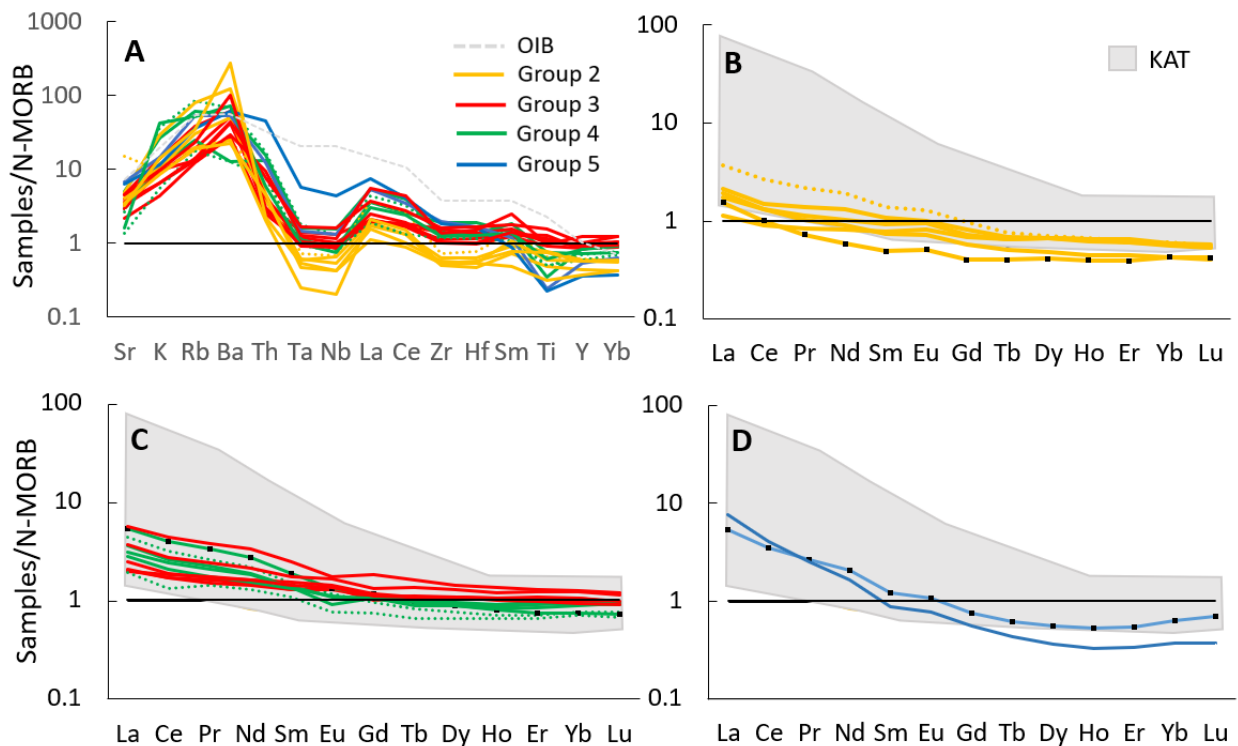


Figure 7. Trace element geochemistry Groups 2, 3, 4, and 5 normalized to N-MORB (after Sun & McDonough, 1989). **A)** Multi-element diagram for Groups 2-5 with LILEs on the left and HFSEs on the right (after Pearce, 1983). Notations of the two “outliers” VP16-25 (Group 5) and VP16-25c (Group 2) have been included. Note that the N-MORB normalized trace element composition of OIB is plotted for reference. **B)** REE compositions of **Group 2** samples. Note that the U-Pb dated sample (**VP16-26f**) is shown with black dots. **C)** REE compositions of the **Group 3** and **Group 4** samples. Note that the U-Pb dated sample (**VP16-23e**) is shown with black dots. **D)** REE composition of **Group 5**. Note that the U-Pb dated sample (**VP16-25a**) is shown with black dots. Shaded region represents REE field of the Koyukuk Arc terrane (**KAT**) from Box & Patton (1989).

**Group 4** includes the Alatna river clast samples (VP16-23e, -23c, -23g, -24b, -25b, -26a). Group 4 is enriched in the fluid-mobile LILEs ( $Rb_{NMORB} = 25-85$ ) and depleted in the HFSEs relative to the LREEs  $[(Nb/La)_{NMORB} = 0.2-0.4]$  and has elevated LILE/HFSE ratios  $[(Rb/Nb)_{NMORB} = 23-69]$  (Figure 7A). The samples have varying REE abundances relative to N-MORB: HREEs are slightly depleted, MREE are similar ( $\sim 1$ ), and the LREEs are enriched (within an order of magnitude) (Figure 7C). Group 3 samples have enriched LREE/HREE ratios  $[(La/Yb)_{NMORB} = 2.7-7.2]$  and enriched  $(MREE/HREE)_N$  ratios  $[(Sm/Yb)_{NMORB} = 1.5-2.5]$ . Their geochemical signature is summarized in Table 4.

**Group 5** includes the Alatna river clast samples (VP16-25a and VP16-25d). Group 5 is enriched in the fluid-mobile LILEs ( $Rb_{NMORB} = 36-53$ ) and depleted in the HFSEs relative to the LREEs and has elevated LILE/HFSE ratios  $[(Rb/Nb)_{NMORB} = 8-40]$ . However, VP16-25a has a more

pronounced HFSE/LREE depletion  $[(\text{Nb}/\text{La})_{\text{NMORB}} = 0.3]$  than VP16-25d which has distinctly higher Ta and Nb concentrations  $[(\text{Nb}/\text{La})_{\text{NMORB}} = 0.6]$  (Figure 7A). Group 5 REE patterns are slightly depleted in MREEs and HREEs, but enriched in the LREEs relative to N-MORB (Figure 7D). Group 5 samples have enriched LREE/HREE and MREE/HREE ratios with VP16-25d displaying a more distinct enrichment  $[(\text{La}/\text{Yb})_{\text{NMORB}} = 20.5; (\text{Sm}/\text{Yb})_{\text{N}} = 2.4]$  than VP16-25a  $[(\text{La}/\text{Yb})_{\text{NMORB}} = 8.5; (\text{Sm}/\text{Yb})_{\text{NMORB}} = 1.9]$ . Their geochemical signature is summarized in Table 4.

Table 4. Summary of trace element signatures for the 5 sample Groups.

Group	Trace element signature	LILE enrichment (Rb <sub>NMORB</sub> )			LILE/HFSE (Rb/Nb) <sub>NMORB</sub>			HFSE/LREE (Nb/La) <sub>NMORB</sub>			LREE/HREE (La/Yb) <sub>NMORB</sub>			MREE/HREE (Sm/Yb) <sub>NMORB</sub>		
		Mean	Min	Max	Mean	Min	Max	Mean	Min	Max	Mean	Min	Max	Mean	Min	Max
1a	E-MORB	<b>15</b>	3	29	<b>5</b>	0.1	7.9	<b>1.3</b>	0.9	2.2	<b>3.5</b>	2.4	5.4	<b>1.8</b>	1.4	2.5
1b	N-MORB	<b>2</b>	1	3	<b>3</b>	1.2	5.4	<b>0.9</b>	0.6	1.1	<b>1.0</b>	0.7	1.2	<b>1.0</b>	0.9	1.2
<b>2</b>	SZ	<b>34</b>	12	39	<b>72</b>	26	122	<b>0.3</b>	0.2	0.7	<b>3.8</b>	1.9	6.1	<b>1.7</b>	1.1	2.3
<b>3</b>	SZ	<b>19</b>	18	80	<b>19</b>	9	41	<b>0.4</b>	0.1	0.4	<b>2.6</b>	1.9	4.5	<b>1.5</b>	1.2	2.0
<b>4</b>	SZ	<b>48</b>	25	85	<b>45</b>	23	69	<b>0.3</b>	0.2	0.4	<b>4.4</b>	2.7	7.2	<b>1.7</b>	1.5	2.5
<b>5</b>	SZ	<b>45</b>	36	53	<b>24</b>	8	40	<b>0.4</b>	0.3	0.6	<b>14.5</b>	8.5	20.5	<b>2.1</b>	1.9	2.4

Notes – Values are normalized to N-MORB of Sun & McDonough (1989).

SZ = subduction zone.

## 6.2 Data correlation to neighboring terranes

The geochemical Groups have trace element chemistry characteristics representing different tectonic environments. Group 1 is enriched in LILEs and lacks a HFSE depletion relative to the LREEs. Group 1 has trace element abundances similar to E-MORB (Group 1a) and N-MORB (Group 1b) and is therefore plotted with the Angayucham terrane (MORB) data of Pallister et al. (1989) (Figure 6B). Group 1a appears transitional between the Jurassic basalt (Jb) and Triassic basalt (Trb) units of the Angayucham terrane (Figure 6B) and display similar LREE enrichment as these rocks (within an order of magnitude). Group 1b has slightly depleted LREE relative to N-MORB and the Angayucham terrane units, however, Group 1b has similar MREE-HREE signatures as the Trb unit.

Groups 2-5 all record enrichment in the LILEs and the LREEs, and depletion in the HFSEs relative to the LREEs, the typical characteristics of subduction zone environments (Kessel et al., 2005; Gerya, 2011). These analyses are therefore plotted with the KAT data of Box & Patton (1989) (Figure 7). Groups 3 and 4 have REE abundances similar to the KAT data (Figure 7C), while Groups 2 and 5 have slightly more depleted REE abundances than the KAT (Figure 7B and 7D). The KAT has a larger range in LREE compositions (up to two orders of magnitude relative to N-MORB) relative to the samples from this study which show LREE enrichments within an order of magnitude. Generally, the REEs of the KAT are similar to Groups 2-5, although the KAT has REEs slightly less depleted and more enriched relative to N-MORB.

### 6.3 Tectonic environment and magma series

The Group 1 samples are MORB tholeiites representing E-MORB (Group 1a) or N-MORB (Group 1b) (Figure 8A). The samples of Groups 2, 3, 4 and 5 are tholeiitic and calc-alkaline. VP16-25d (Group 5) is referred to as calc-alkaline due to its primary mineralogy having signs of being altered (severe sericitization) which can cause it to appear more shoshonitic, and it has normalized REE patterns consistent with its calc-alkaline Group member (VP16-25a).

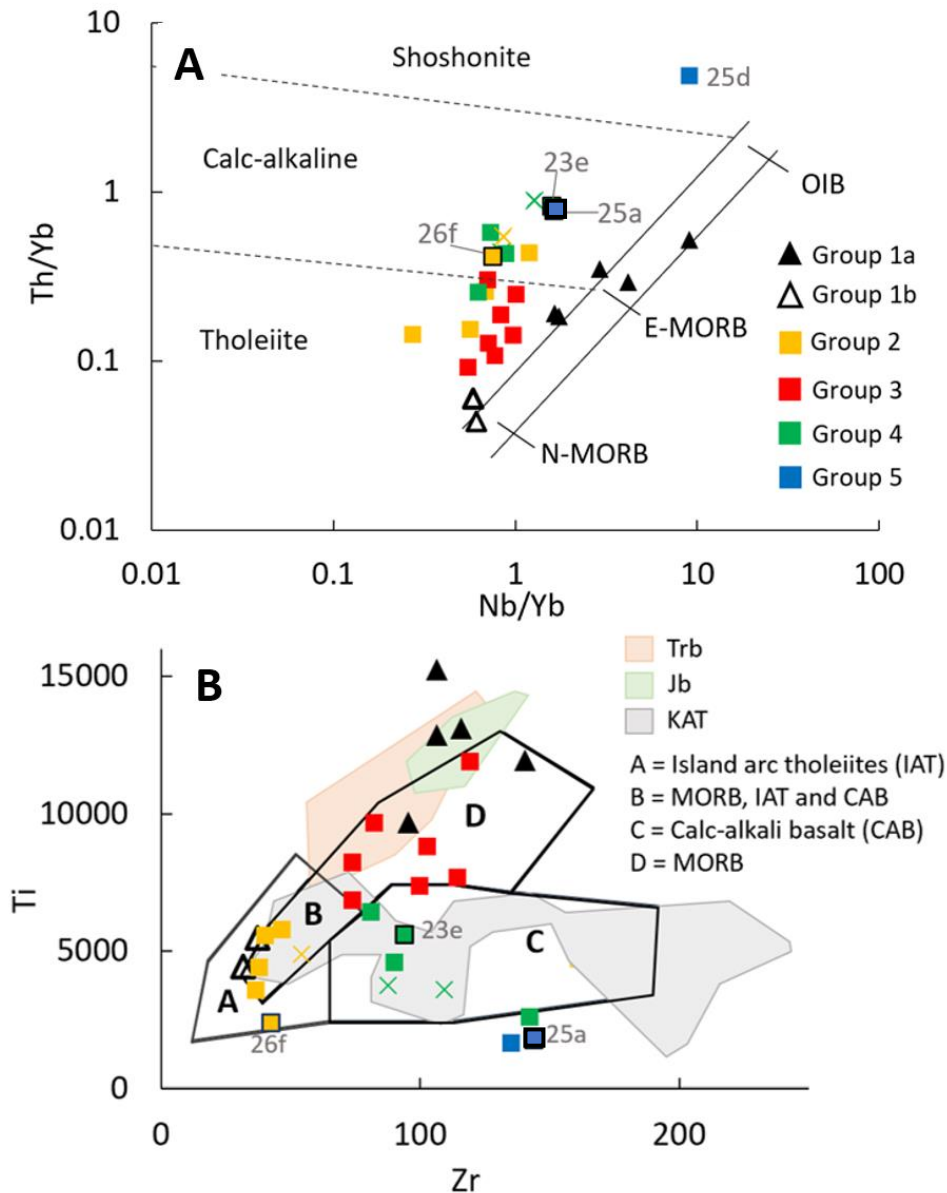


Figure 8. Tectonic discrimination diagrams. **A)** The Th/Yb vs Nb/Yb diagram (after Pearce, 1982) discriminates between different magma series and magmatic evolutionary trends. Note that Group 1a and Group 1b follow the MORB array, while the other Groups represent subduction-related tholeiitic to calc-alkalic trends. **B)** Immobile element diagram to distinguish between island arc vs mid-ocean ridge basalts and related magma series (after Pearce & Cann, 1973). Note that Group 1b (open black triangles), together with Group 2 samples, are similar to island arc tholeiites (IAT, field A).

The same trend is seen in Figure 8B. Group 1a lies in or just above the MORB field. The Group 3 tholeiitic samples lie in the MORB field, though straddling the division to the calc-alkaline field, and Group 2 samples plot in the island arc tholeiite field (IAT) together with Group 1b and straddling the division to the mixed field. Group 4 samples generally plot in the calc-alkaline field while the more evolved rock types of Group 5 and one sample from Group 4 (VP16-23g) lie slightly outside the calc-alkaline field. Note that this diagram was constructed using basaltic rocks which may explain why the more evolved rock types plot outside the calc-alkaline field. Angayucham terrane data from Pallister et al. (1989) and KAT data from Box & Patton (1989) are included in the diagram for comparison. The KAT data is similar to Groups 3, 4 and possibly 5, whilst the Angayucham terrane data (Jb and Trb) is similar to Group 1a and possibly Group 3.

#### 6.4 U-Pb geochronology

The U-Pb zircon analytical results from three igneous samples are presented in Appendix Table D. Representative CL zircon images from these samples are shown together with their  $^{206}\text{Pb}/^{238}\text{U}$  ages in Figure 9. The geochronological data from three samples VP16-23e, VP16-25a and VP16-26f yield concordia ages of  $212.9 \pm 2.2$  Ma,  $193.7 \pm 1.7$  and  $195.1 \pm 1.1$  (95% confidence), respectively (Figure 10). The VP16-25a granodiorite and VP16-26f diorite have ages that overlap within error, whereas the age of the VP16-23e diorite is statistically different from the others.

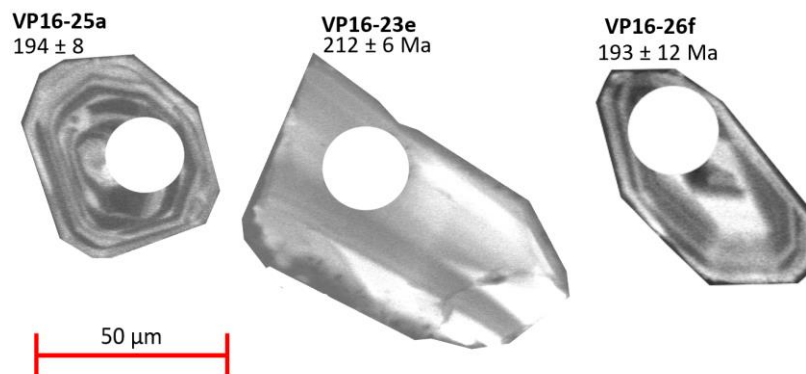


Figure 9. Cathodoluminescence (CL) images of representative zircon from the three KKB conglomerate clasts analysed for U-Pb zircon geochronology. The white circle on each zircon grain represents the 20  $\mu\text{m}$  laser spot (used for all samples) location. Associated errors are  $2\sigma$ . Note the typical growth zoning associated with magmatic zircons (Corfu et al., 2003).

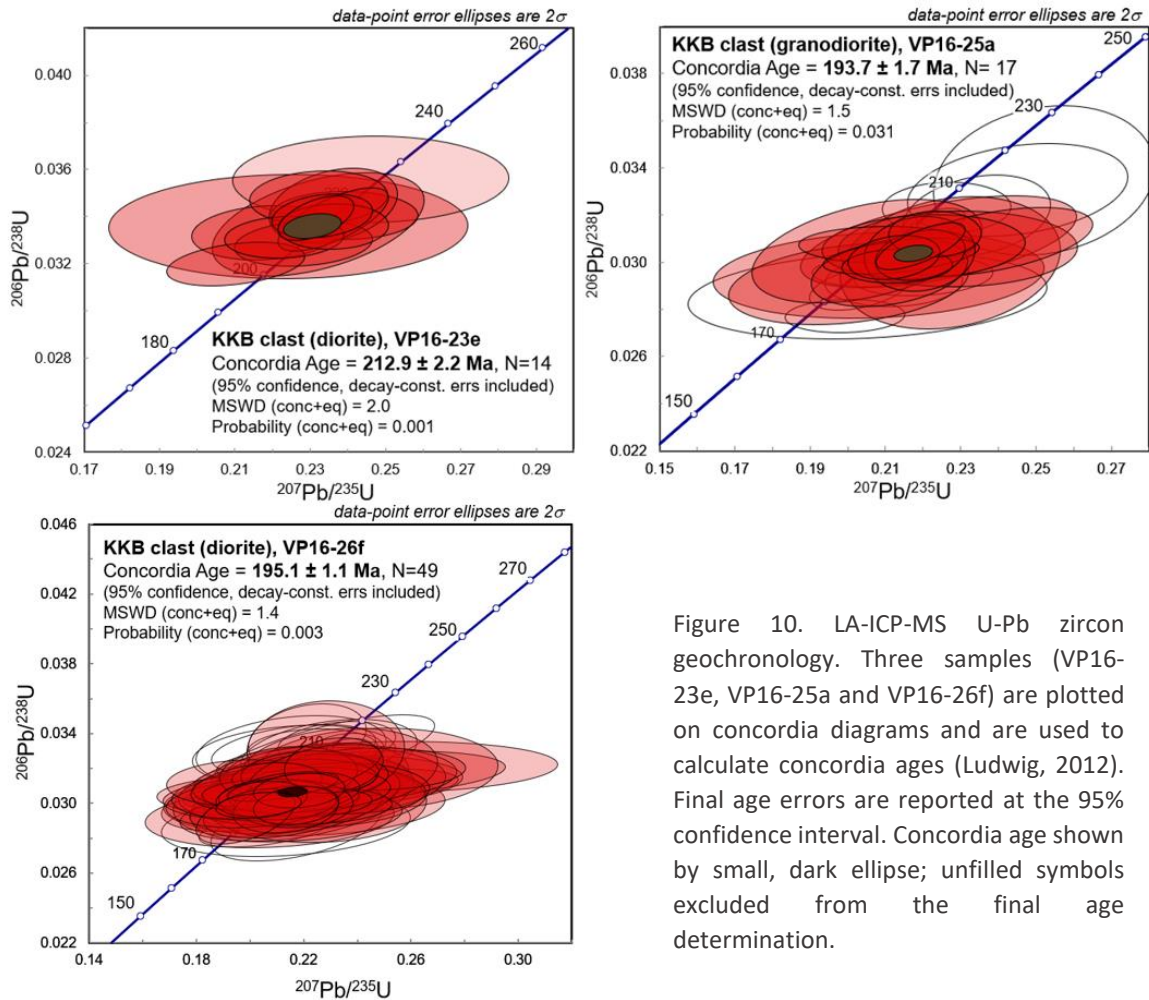


Figure 10. LA-ICP-MS U-Pb zircon geochronology. Three samples (VP16-23e, VP16-25a and VP16-26f) are plotted on concordia diagrams and are used to calculate concordia ages (Ludwig, 2012). Final age errors are reported at the 95% confidence interval. Concordia age shown by small, dark ellipse; unfilled symbols excluded from the final age determination.

## 6.5 Isotope geochemistry

Neodymium isotopic analytical results for 12 igneous samples are given in Table 5. The samples include Group 1a (VP15-10, -13 and VP16-22a), Group 1b (VP16-22c), Group 2 (VP16-24a, -24d, -26f), Group 3 (VP16-23a, -26b), Group 4 (VP16-23g, -24b), and Group 5 (VP16-25d). The measured  $^{143}\text{Nd}/^{144}\text{Nd}$  ratios for the 12 samples define a narrow range from 0.51283 to 0.51309, and from +3.75 to +8.86  $\epsilon\text{Nd}$ . The lowest  $^{143}\text{Nd}/^{144}\text{Nd}$  ratios are represented by the samples of Group 1a. Samples of Groups 1b, 2, 3, 4 and 5 have similar  $^{143}\text{Nd}/^{144}\text{Nd}$  ratios and are generally within analytical error, with the exception of the Group 5 sample (VP16-25d) which has a slightly lower  $^{143}\text{Nd}/^{144}\text{Nd}$  ratio.

Initial  $^{143}\text{Nd}/^{144}\text{Nd}$  ratios have been calculated using an age of 200 Ma, the approximate age of the three dated samples. Due to the slow decay rate of  $^{147}\text{Sm}$  to  $^{143}\text{Nd}$  (half life  $T_{1/2} = 1.06 \times 10^{11}$ ) and the relatively young age of the samples, the difference between initial  $^{143}\text{Nd}/^{144}\text{Nd}$  ratios and measured ratios (present day) is small (c. 0.03-0.06 %). The epsilon values calculated

at the time  $t = 200$  Ma ( $\epsilon Nd_{(t)}$ ) vary from +4.39 to +9.38. Group 1a have the lowest initial epsilon values between +4.39 to +6.34 and Group 1b has a slightly higher initial epsilon value of +7.59. Group 2 have initial epsilon values varying between +8.79 to +9.16 and Group 3 have initial epsilon values varying between +8.56 to +8.67. Group 4 have initial epsilon values varying between +8.70 to +9.38 and Group 5 has an initial epsilon value slightly lower than the other volcanic arc Groups of +7.78.

Table 5. Neodymium isotope data.

Lithology	Sample	Group	$^{143}\text{Nd}/^{144}\text{Nd}$	$\pm$	$\epsilon Nd$	$^{147}\text{Sm}/^{144}\text{Nd}$	$(^{143}\text{Nd}/^{144}\text{Nd})_t$	$\epsilon Ndt$	$f(\text{Sm}/\text{Nd})$
Microgabbro	VP15-10	1a	0.512830	0.000009	3.75	0.1716	0.512605	4.39	-0.20
Microgabbro	VP15-13	1a	0.512951	0.000009	6.11	0.1876	0.512705	6.34	-0.05
Gabbro	VP16-22a	1a	0.512898	0.000009	5.07	0.1687	0.512677	5.79	-0.14
Basalt	VP16-22c	1b	0.513085	0.000009	8.72	0.2409	0.512770	7.59	0.22
Microgabbro	VP16-23a	3	0.513088	0.000009	8.78	0.201	0.512825	8.67	0.02
Granodiorite	VP16-23g	4	0.513030	0.000009	7.65	0.1555	0.512826	8.70	-0.21
Gabbro	VP16-24a	2	0.513075	0.000009	8.52	0.1863	0.512831	8.79	-0.05
Gabbro	VP16-24b	4	0.513092	0.000009	8.86	0.1765	0.512861	9.38	-0.10
Microgabbro	VP16-24d	2	0.513054	0.000009	8.11	0.1701	0.512831	8.80	-0.14
Granite	VP16-25d	5	0.512924	0.000009	5.58	0.1106	0.512779	7.78	-0.44
Gabbro	VP16-26b	3	0.513064	0.000009	8.31	0.1871	0.512819	8.56	-0.05
Diorite	VP16-26f	2	0.513076	0.000009	8.54	0.1728	0.512850	9.16	-0.12

Notes - Age corrections (t) were made using an age of 200 Ma for all samples. Absolut errors (2 sigma) are given by the external precision judged from the La Jolla standard. Total error propagation leads to +/- half an epsilon. All values have been normalized to  $^{146}\text{Nd}/^{144}\text{Nd} = 0.7219$ . Epsilon values have been calculated using the present-day CHUR ratio of  $^{143}\text{Nd}/^{144}\text{Nd} = 0.512638$  of Goldstein et al. (1984).

Lead isotopic analytical results for the 12 igneous samples are given in Table 6 and represent a pilot study. The results show that 5 of the 12 samples have similar lead isotopic compositions: VP16-24a, VP16-24d, VP16-26f (group 2); VP16-23a, VP16-26b (group 3). Group 2 and 3 have lead isotopic compositions that vary between 18.74-18.86, 15.53-15.58 and 38.04-38.39 for  $^{206}\text{Pb}/^{204}\text{Pb}$ ,  $^{207}\text{Pb}/^{204}\text{Pb}$  and  $^{208}\text{Pb}/^{204}\text{Pb}$ , respectively. The remaining 7 samples include: VP15-10, -13, VP16-22a, -22b (Group 1a); VP16-22c (Group 1b); VP16-23g, -24b (Group 4) and VP16-25d (Group 5).

Group 1a samples display an unusual spread in their lead isotopic compositions with  $^{206}\text{Pb}/^{204}\text{Pb}$  and  $^{208}\text{Pb}/^{204}\text{Pb}$  ratios ranging from 18.20 to 20.12 and 37.96 to 39.26, respectively, at a nearly constant  $^{207}\text{Pb}/^{204}\text{Pb}$  value (15.60 to 15.64). The two samples from Group 4 also display a spread between their  $^{206}\text{Pb}/^{204}\text{Pb}$  and  $^{208}\text{Pb}/^{204}\text{Pb}$  ratios which vary from 19.32 to 20.24 and 37.96 to 39.26, respectively, at  $^{207}\text{Pb}/^{204}\text{Pb}$  values of 15.54 to 15.63. Since acid leaching was not performed prior to the analyses, scatter within Group 1a and Group 4 isotopic ratios could be an artifact related to lead contamination and future lead isotope processing will apply leaching experiments. Since the N-MORB sample of Group 1 and the Group 5 sample are the only samples analyzed from their respective Groups, the data cannot

reliably be interpreted and the possibility of these ratios being modified by lead contamination cannot be ignored. However, the samples of Groups 2 and 3 have isotopic compositions that are consistent within Groups and their Pb isotopic values are considered semi-reliable.

Table 6. Lead isotope data.

Lithology	Sample	Group	$^{206}\text{Pb}/^{204}\text{Pb}$	$\pm$	$^{207}\text{Pb}/^{204}\text{Pb}$	$\pm$	$^{208}\text{Pb}/^{204}\text{Pb}$	$\pm$
Microgabbro	VP15-10	1a	18.20	0.006	15.64	0.007	38.42	0.025
Microgabbro	VP15-13	1a	18.92	0.020	15.60	0.020	38.45	0.068
Gabbro	VP16-22a	1a	20.12	0.018	15.61	0.011	39.86	0.041
Basalt	VP16-22c	1b	19.67	0.005	15.63	0.004	38.97	0.015
Microgabbro	VP16-23a	3	18.79	0.006	15.56	0.008	38.25	0.028
Granodiorite	VP16-23g	4	19.32	0.017	15.54	0.015	37.96	0.052
Gabbro	VP16-24a	2	18.74	0.009	15.54	0.008	38.17	0.026
Gabbro	VP16-24b	4	20.24	0.012	15.63	0.006	39.26	0.023
Microgabbro	VP16-24d	2	18.92	0.013	15.54	0.013	38.39	0.042
Granite	VP16-25d	5	20.28	0.011	15.63	0.005	39.08	0.021
Gabbro	VP16-26b	3	18.86	0.006	15.58	0.006	38.37	0.025
Diorite	VP16-26f	2	18.83	0.007	15.53	0.009	38.04	0.026

Notes - Absolut errors (2 sigma) are given by the external precision judged from the NBS-981 standard.

## 7. Discussion

### 7.1 Age, petrogenesis, and tectonic environment.

This investigation into igneous conglomerate clasts and mafic outcrop samples from the KKB recognizes five distinct chemical Groups (Table 7).

**Group 1a** consists of tholeiites with E-MORB chemistry and enriched  $(\text{La}/\text{Yb})_N$  ratios (Table 7). Group 1a lacks the subduction zone signature as it has low  $(\text{LILE}/\text{HFSE})_N$ , no relative depletion in  $\text{HFSE}_N$  to  $\text{LREE}_N$  (normalized ratios c. 1) and low-moderate LILE enrichments (e.g.  $\text{Rb}_N$ ) (Table 7). The E-MORB chemistry and the positive initial  $\epsilon\text{Nd}$  values suggests that the Group 1a samples have been derived from a depleted mantle source with an enriched component. The lead isotopic data is not considered to be meaningful due to unusual spread and inconsistency between samples within the group. No age has been obtained for Group 1a.

**Group 1b** consists of tholeiites with N-MORB chemistry and non-enriched  $(\text{La}/\text{Yb})_N$  ratios (c. 1) (Table 7). Group 1b lacks the subduction zone signature since it has low  $(\text{LILE}/\text{HFSE})_N$ , no depletion in  $\text{HFSE}_N$  relative to  $\text{LREE}_N$  (normalized ratios c. 1) and no distinct LILE enrichment (e.g.  $\text{Rb}_N$ ) (Table 7). The N-MORB chemistry and the positive initial  $\epsilon\text{Nd}$  suggests that Group 1b samples have been derived from a depleted mantle source. The one sample analyzed for

lead isotopes is not enough to conclude whether the lead isotopic data is meaningful. No age has been obtained for this Group.

Table 7. Geochemical and geochronological summary of the sample Groups.

Group	Magma Series	(La/Yb) <sub>N</sub>	LILE-enrichment (Rb <sub>N</sub> )	Trace element characteristics	Initial εNd	Pb	Age	Mantle source	Tectonic setting
Group 1a solid black	Tholeiitic	3.5	15	Low (LILE/HFSE) <sub>N</sub> ; (HFSE/LREE) <sub>N</sub> (c. 1);	+4.39 +6.34	?	?	DM + enriched comp.	Spreading ridge
Group 1b open black	Tholeiitic	1.0	2	Low (LILE/HFSE) <sub>N</sub> ; (HFSE/LREE) <sub>N</sub> (c. 1);	+7.59	?	?	DM	Spreading ridge
Group 2 yellow	Tholeiitic	3.8	34	High (LILE/HFSE) <sub>N</sub> ; Low (HFSE/LREE) <sub>N</sub> ;	+8.79 +9.16	MORB	195 Ma	DM + SZ comp.	Island arc
Group 3 red	Tholeiitic	2.6	19	High (LILE/HFSE) <sub>N</sub> ; Low (HFSE/LREE) <sub>N</sub> ;	+8.56 +8.67	MORB	?	DM + SZ comp.	Island arc
Group 4 green	Calc-alkalic	4.4	48	High (LILE/HFSE) <sub>N</sub> ; Low (HFSE/LREE) <sub>N</sub> ;	+8.70 +9.38	?	213 Ma	DM + SZ comp.	Island arc
Group 5 blue	Calc-alkalic	14.5	45	High (LILE/HFSE) <sub>N</sub> ; Low (HFSE/LREE) <sub>N</sub> ;	+7.78	?	194 Ma	DM + SZ comp.	Island arc

Notes – Values are normalized to N-MORB of Sun & McDonough (1989). SZ comp. = subduction zone component. Initial εNd has been calculated at time t=200 Ma.

**Group 2** consists of island arc tholeiites (some transitional to calc-alkaline) with subduction zone chemistry indicated by high (LILE/HFSE)<sub>N</sub> ratios, depletion in HFSE<sub>N</sub> relative to LREE<sub>N</sub> and enriched LILE (e.g. Rb<sub>N</sub>) contents (Table 7). Group 2 samples have depleted HREE<sub>N</sub> and HFSE<sub>N</sub> abundances (<1) and moderately enriched (La/Yb)<sub>N</sub> ratios (Table 7). Group 2 have positive εNd values and lead isotopic ratios that are similar to MORB. The isotopic composition suggests that the Group 2 samples have been derived from a depleted mantle source. The U-Pb zircon geochronology resulted in an age of 195 Ma, thus Group 2 is assumed to be Early Jurassic in age.

**Group 3** consists of tholeiites with subduction zone chemistry displayed by the high (LILE/HFSE)<sub>N</sub>, depletion in HFSE<sub>N</sub> relative to LREE<sub>N</sub> and moderately enriched LILE (e.g. Rb<sub>N</sub>) contents (Table 7). Group 3 samples have HREE<sub>N</sub> and HFSE<sub>N</sub> abundances similar to N-MORB (c. 1) and have slightly enriched (La/Yb)<sub>N</sub> ratios (Table 7). Group 3 also have positive initial εNd values and lead isotopic ratios that are similar to MORB and a depleted mantle source. The isotopic composition suggests that Group 3 samples have been derived from a depleted mantle source. No ages have been obtained for Group 3.

**Group 4** consists of calc-alkaline samples with subduction zone chemistry displayed by the high  $(LILE/HFSE)_N$ , relative depletion in  $HFSE_N$  to  $LREE_N$  and enriched LILE (e.g.  $Rb_N$ ) contents (Table 7). Group 4 samples have  $HREE_N$  and  $HFSE_N$  abundances that are similar/slightly enriched, relative to N-MORB (c. 1) and have enriched  $(La/Yb)_N$  ratios (Table 7). Group 4 have positive initial  $\epsilon Nd$  values indicative of a depleted mantle source. The lead isotopic data is not considered to be meaningful due to unusual spread and inconsistency between samples within the group. The U-Pb zircon geochronology resulted in an age of 213 Ma, thus Group 4 is assumed to be Late Triassic in age.

**Group 5** consists of calc-alkaline samples with subduction zone chemistry displayed by the high  $(LILE/HFSE)_N$ , depleted  $HFSE_N$  relative to  $LREE_N$  and enriched LILE (e.g.  $Rb_N$ ) contents (Table 7). Group 5 samples have depleted  $HREE_N$  ( $<1$ ) and enriched  $HFSE_N$  ( $>1$ ) abundances and enriched  $(La/Yb)_N$  ratios (Table 7). Group 5 has a positive initial  $\epsilon Nd$  value indicative of a depleted mantle source. The one sample analyzed for lead isotopes is not enough to conclude whether the lead isotopic data is meaningful. The U-Pb zircon geochronology age is 194 Ma, thus Group 5 is assumed to be Early Jurassic in age.

*Volcanic arc samples.* The subduction signature displayed by the island arc Groups 2, 3, 4 and 5 is formed when subduction-related fluids, generated via devolatilization reactions during subduction of the hydrothermally altered slab and sediments, are released to the mantle wedge; these fluids transfer fluid-mobile elements, such as the LILEs and also the LREEs, U, Pb and Th (Kessel et al., 2005). These subduction fluids lower the mantle solidus which promotes partial melting in the mantle wedge (also known as flux-melting) and produces magmas with elevated LILE and LREE (including U, Pb and Th) contents relative to HFSEs and HREEs, which are not mobilized by the subduction fluids. The elements that occur in elevated concentrations in arc magmas are commonly called slab-derived or non-conservative components (e.g. Ba, Rb, K, Sr, La, Ce, U, Pb and Th) (Metcalf & Shervais, 2008). Since the HFSEs and the HREEs are not mobilized by subduction fluids, the concentration of these elements in arc rocks mainly reflect the composition of the mantle wedge from which they were derived. Consequently, these Groups of elements are sometimes called conservative mantle wedge-derived (or conservative components (e.g. Nb, Ta, Zr, Hf, Ti, Dy, Y, Yb and Lu) (Hastie et al., 2007).

**Groups 3 and 4** have similar conservative (mantle wedge-derived) element concentrations of N-MORB composition as displayed by the multi-element and REE-diagrams (Figure 7A, 7C). This implies that these Groups were derived from a similar mantle-wedge, i.e. N-MORB composition. In the Th/Yb vs Nb/Yb diagram (Figure 8A) Groups 3 and 4 define a vertical trend with similar Nb/Yb ratios but increasing Th/Yb ratios. Since both Nb and Yb are incompatible and conservative mantle wedge-derived elements, the ratio Nb/Yb ratio should not be affected by the addition of subduction fluids into the mantle wedge (Hastie et al., 2007). However, Th becomes fluid-mobile at higher temperatures (c. 450-650°C) and the Th/Yb ratio

may increase when the subducting slab reaches the higher temperature environment associated with greater mantle depths (Hastie et al., 2007). Consequently, Th/Yb is used to distinguish between the generally dry, shallow melting associated with tholeiitic magmas (such as Group 3) and the generally deeper and more hydrous melting associated with calc-alkaline magmas (such as Group 4) (Hastie et al., 2007; Metcalf & Shervais, 2008).

The vertical trend in Figure 8A implies that Groups 3 and 4 were derived from a common mantle-wedge but have been affected by various degrees of fluid-flux and/or different percentages of partial melting. Differences in subduction fluid input between tholeiitic Group 3 and calc-alkaline Group 4 is also indicated by differing degrees of LILE enrichment ( $Rb_N$ ) (Table 7). Group 3 have relatively lower LILE enrichment suggestive of a lower fluid-flux and shallower melting which is typical of tholeiitic magmas. Group 4 have relatively higher LILE enrichment consistent with a higher fluid-flux at greater depths which is a characteristic of calc-alkaline magmas. Thus, the tholeiitic chemistry of Group 3 and the calc-alkalic chemistry of Group 4 suggests that these Groups were derived from an island arc setting with a mantle-wedge compositionally similar to N-MORB prior to wedge hydration. The tholeiites of Group 3 would represent shallow melting in the mantle wedge close to the trench and the calc-alkaline Group 4 would represent deeper and more hydrous melting further from the trench, which is a common trend for magma evolution in island arcs (Wilson, 2007). No age data were obtained for Group 3, but similarities in geochemistry between the two Groups suggests that Group 3 should also be Triassic (213 Ma) in age.

**Group 2** and **Group 5** have conservative element concentrations similar to each other and both have HREE contents that are depleted relative to N-MORB as shown in the multi-element and REE-diagrams (Figure 7A, 7B and 7D). The depleted tholeiitic chemistry of Group 2 and the HREE depleted calc-alkalic chemistry of Group 5 suggests that these Groups were derived from different parts of a mantle wedge already depleted in incompatible elements, such as a mantle that has experienced a previous melt extraction event (Metcalf & Shervais, 2008). In this scenario the island arc tholeiites of Group 2 represent shallow melting in the depleted mantle wedge close to the trench and the calc-alkalic Group 5 would represent deeper and more hydrous melting further from the trench. This is verified by the Th/Yb vs Nb/Yb diagram (Figure 8A) where Group 5 samples show higher Th/Yb ratios than Group 2, indicating that their magmas have been affected by a greater degree of fluid-flux and/or smaller percentages of partial melting. Group 5 also differs from Group 2 in having higher Nb/Yb ratios which may be explained by differences in the vertical and/or lateral composition of the mantle wedge or by smaller degrees of partial melting (Metcalf & Shervais, 2008). The difference in subduction fluid input between tholeiitic Group 2 and calc-alkalic Group 5 is also indicated by the Groups having different degrees of LILE enrichment ( $Rb_N$ ) (Table 7). Group 2 have relatively lower LILE enrichment suggestive of a lower fluid-flux and shallower melting which is typical of tholeiitic magmas. Group 5 have relatively higher LILE enrichment consistent with a higher fluid-flux at greater depths which is a characteristic of calc-alkaline magmas. The depleted nature of

Groups 2 and 5 together with their Jurassic age (c. 195 Ma, within error), relative to Groups 3 and 4 (213 Ma), indicates that they cannot be co-genetic with the Triassic Groups.

*MORB samples.* **Group 1** differs from Groups 2-5 by having chemistry of rift-related magmatism (MORB) rather than subduction-related magmatism. This is obvious in the lack of the subduction zone signature (depleted HFSE<sub>N</sub> and HREE<sub>N</sub> relative to enriched LILE<sub>N</sub> and LREE<sub>N</sub>; Figure 6A). The lack of/relatively low LILE enrichment (Rb<sub>N</sub>) of Group 1 indicates no subduction-related fluid input into their genesis. The slightly higher LILE enrichment of Group 1a can be explained by partial melting of an enriched mantle source. The anomalous peaks in barium (Ba<sub>N</sub>) seen in all Groups, including the subduction related ones, is likely due to secondary hydrothermal alteration which has affected all samples. **Group 1a** and **Group 1b** differ from each other in their incompatible trace element concentrations as Group 1a is enriched in trace elements relative to N-MORB and Group 1b has incompatible trace element contents slightly depleted relative to N-MORB (Figures 6A and 6B). The MORB chemistry is also indicated in the Th/Yb vs Nb/Yb diagram (Figure 8A) in which Group 1 samples spread along the MORB-array, from N-MORB (Group 1b) to E-MORB (Group 1a). The variation in the Nb/Yb ratios seen for some of the samples of Group 1a may be explained by differences in the vertical and/or lateral mantle wedge composition or by different degrees of partial melting (Metcalf & Shervais, 2008).

The two MORB types represented by Group 1 samples are commonly inferred to originate from two different mantle sources in the published literature, with N-MORB compositions representing partial melts of the uppermost depleted mantle associated with the formation of basalts at mid-ocean ridges (Fitton, 2007). E-MORBs are believed to constitute the lower enriched mantle and are generally associated with mantle plumes and the formation of ocean island basalts and seamounts (Hémond et al., 2006). However, it has been suggested that the upper mantle is heterogeneous and that both N-MORB and E-MORB are commonly found at mid-ocean ridges and seamounts (Fitton, 2007; Gale et al., 2013).

## 7.2 Mantle source(s)

The lead isotopic data for Groups 1a, 1b, 4 and 5 is not considered to be meaningful due to either a large spread or inconsistency of data between the Groups. Groups 2 and 3 have lead isotopic data that is at least consistent within each Group, and are regarded as semi-reliable.

*Volcanic arc samples.* The consistency of lead data within Groups 2 and 3 is displayed on isotope correlation diagrams (Figure 11), in which data from several tectonic environments (continental- and island-arcs, MORB and OIB) and isotopic reservoirs (depleted mantle, DM; enriched mantle type-I, EMI; enriched mantle type-II, EMII; high- $\mu$  mantle, HIMU) are included for reference. Groups 2 and 3 plots together and have isotopic compositions that are

consistently similar to the Aleutian arc and Pacific MORB in all three Pb-projections (Figure 11). In Figure 12A and 12B, Groups 2 and 3 plots slightly on the northern hemisphere reference

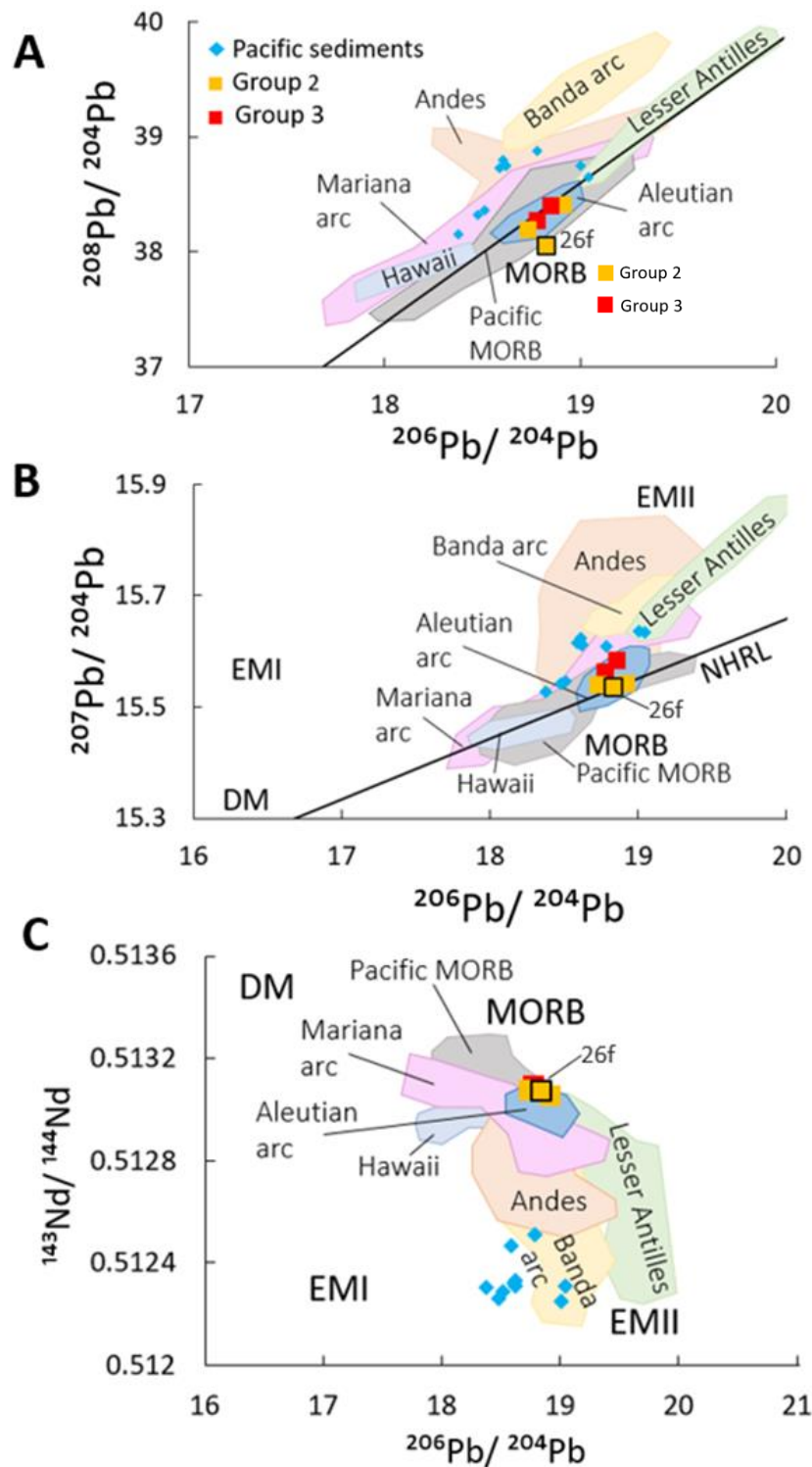


Figure 11. Mantle sources from lead and neodymium isotopes. **A)**  $^{208}\text{Pb}/^{204}\text{Pb}$  vs  $^{206}\text{Pb}/^{204}\text{Pb}$  correlation diagram showing the data with respect to the NHRL and MORB (values from Hart, 1984; Zindler & Hart, 1986). **B)**  $^{207}\text{Pb}/^{204}\text{Pb}$  vs  $^{206}\text{Pb}/^{204}\text{Pb}$  correlation diagram showing the data with respect to the NHRL and the isotopic reservoirs EMI, EMII, DM and HIMU (values from Zindler & Hart, 1986). **C)**  $^{143}\text{Nd}/^{144}\text{Nd}$  vs

$^{207}\text{Pb}/^{204}\text{Pb}$  correlation diagram showing the data with respect to the isotopic reservoirs and rock types from common tectonic environments (MORB, volcanic arcs and OIBs). Reference data from Pacific MORB, Mariana arc, Aleutian arc, Andes, Hawaii, Lesser Antilles, Banda arc and Pacific sediments have been obtained from the GEOROC database (Ishizuka et al., 2010; Elburg et al., 2005; Singer et al., 2007; Hanano et al., 2010; Muñoz et al., 2010; Chiaradia et al., 2009; Labanieh et al., 2012; Hauff et al., 2003 and White et al., 1987). Note that Pacific sediments, continental arc (Andes) and island arcs with large sedimentary input (Banda arc and Lesser Antilles) display a mixing line between MORB and EMII, and that island arcs with minor sedimentary input (such as Marianas and Aleutian arc) also plot on a similar mixing line but closer to MORB.

line (NHRL) and have similar lead isotopic composition as MORB. Pronounced mixing trends are not visible between these isotopic mantle reservoirs, although Group 3 is slightly elevated towards the EMII reservoir (Figure 11B). Overall, the isotopic compositions of the samples (MORB-like) indicates little or no sediment input or contamination by old continental crust, denoting that the Triassic and Jurassic volcanic arc Groups originate from a mantle source consistent with an intra-oceanic island arc setting.

The positive initial  $\epsilon\text{Nd}$  (+7.8 to +9.4) of the volcanic arc Groups 2, 3, 4 and 5 denotes a depleted mantle source origin (Faure & Mensing, 2005). These isotopic values are similar to modern intra-oceanic island arc systems in the Pacific Ocean, such as the Aleutian arc (+7.4 to +8.9  $\epsilon\text{Nd}$ ; Jicha et al., 2004) and the Mariana arc (+6.9 to +8.79  $\epsilon\text{Nd}$ ; Stern et al., 2006) which is consistent with an inferred island arc developed on MORB-type oceanic crust. The vertical trends associated with increasing fractionation factors ( $f^{\text{Sm}/\text{Nd}}$ ) at a nearly constant initial  $\epsilon\text{Nd}_{(t)}$  shown by Groups 2 and 4 (Figure 12), indicates that these magmas were unaffected by open system processes such as assimilation/contamination from old continental crust. The vertical trends also suggest that magmas within the individual Groups might be related by a closed system process such as crystal fractionation. The small variation in the initial  $\epsilon\text{Nd}_{(t)}$  of the Group 3 samples indicate that their magmas might not be related by a closed system process such as crystal fractionation, but rather by different degrees of partial melting of a common melt source. Group 5 shows no variation since there is only data from one sample.

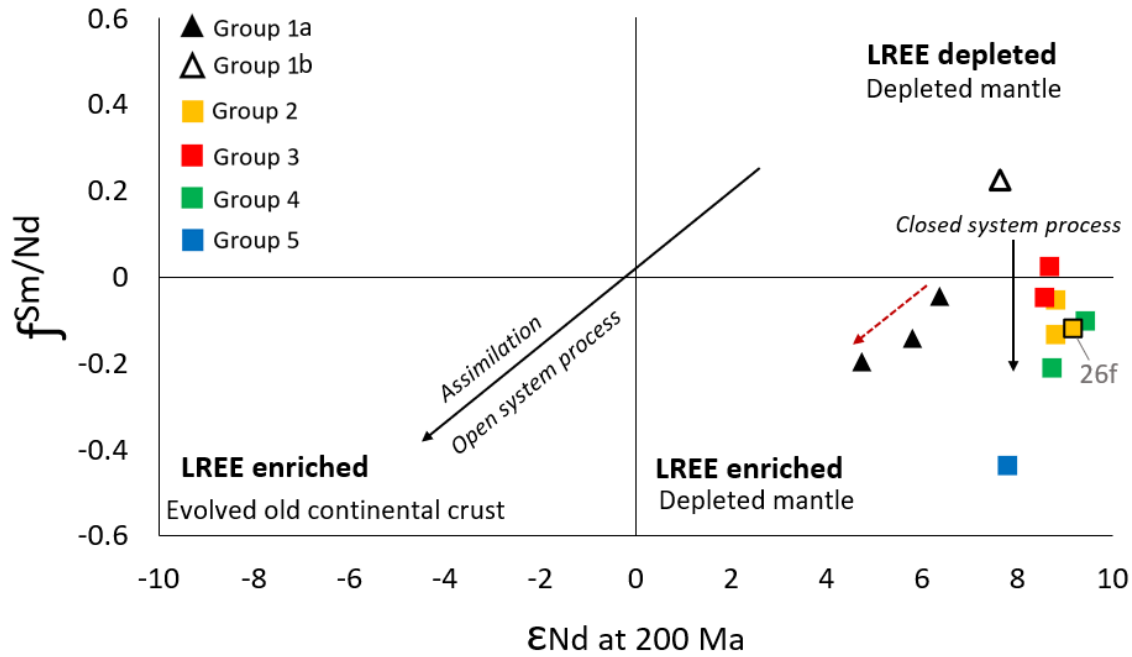


Figure 12.  $f_{Sm/Nd}$  vs  $\epsilon Nd(t)$  diagram modified from Zachariah et al. (1997). Initial epsilon values calculated at time  $t=200$  Ma. On this diagram closed system processes form a vertical array, distinct from open system processes (e.g. magma mixing and crustal assimilation). Note that the samples within Groups 2 and 3 define closed systems (vertical trends), while Groups 4 and 1a has not been a closed system (indicated by red arrow). Groups 1b and 5 show no variation.

**MORB samples.** Similarities in minor and trace element chemistry between the Alatna outcrop samples and the Koyukuk River clasts indicate a strong correlation between them and since both include samples with N-MORB and E-MORB chemistry it can be proposed that the Group 1 magmas were derived from a compositionally heterogeneous mantle source. The positive initial  $\epsilon Nd$  values of Group 1a (+4.39 to +6.34) and Group 1b (+7.59) indicate a depleted mantle source origin and these isotopic values are similar to what has been obtained from modern seamounts in the Pacific Ocean, such as the Darwin Rise seamounts (+2.0 to +7.8  $\epsilon Nd$ ; Janney & Castillo, 1999) and the Emperor Hawaiian seamounts (+5.63 to +9.91  $\epsilon Nd$ ; Regelous et al., 2003). The higher initial  $\epsilon Nd$  value of Group 1b is consistent with its N-MORB chemistry (depleted mantle) and the relatively lower initial  $\epsilon Nd$  value of Group 1a is consistent with its E-MORB chemistry (mantle with an enriched component). This is supported by the  $f_{Sm/Nd}$  vs (initial)  $\epsilon Nd(t)$  diagram (Figure 12) in which Group 1b plots in the upper-right LREE depleted-depleted mantle quadrant consistent with its depleted N-MORB chemistry, and Group 1a plots in the lower-right LREE enriched-depleted mantle quadrant consistent with its enriched E-MORB chemistry. Group 1a displays a trend to lower initial  $\epsilon Nd$  with decreasing fractionation factor values. The non-vertical trend implies that Group 1a magmas have not been a closed system; it may indicate that contamination by an old isotopically enriched source might have affected these magmas, but it could also reflect compositional variation in the mantle or different degrees of partial melting. Group 1b shows no variation since there is only data from

one sample. The lack of reliable lead isotope data for Group 1 prevents further investigation of possible mixing between the isotopic mantle reservoirs.

### 7.3 Correlation(s) to potential sources

*Relationship to the KAT.* All samples from Groups 2, 3, 4 and 5 (Alatna river conglomerate clasts) record a subduction zone signature, i.e.- elevated  $LILE_N$  and  $LREE_N$ , plus relative depletions in the  $HFSE_N$  and  $HREE_N$ , and have isotopic compositions consistent with genesis in an intra-oceanic island arc setting. This indicates that the samples of Groups 2, 3, 4 and 5 in this study were formed in a tectonic setting similar to what has been proposed for the KAT (e.g. Box & Patton, 1989). Immobile elements and N-MORB normalized REE diagrams show that these 'island arc' Groups also have minor and trace element concentrations similar to the KAT. However, the Late Triassic – Early Jurassic ages of samples from this study are distinctly older than the Middle Jurassic to Early Cretaceous KAT (KAT Units 2 – 4). Despite some similarities in the trace element signatures of the KAT and sample Groups 2-5, the age difference argues strongly against the hypothesis that these KKB clasts are erosional products of the KAT. The oldest part of the KAT (KAT Unit 1) was suggested to be pre-Middle Jurassic in age on the basis of poorly constrained fossil ages (Box & Patton, 1989), however, the lack of a subduction signature such as elevated  $LILE_N$  and  $LREE_N$ , plus relative depletions in the  $HFSE_N$  and  $HREE_N$ , makes Unit 1 unlikely to be the source terrane of the volcanic arc samples in this study.

*Relationship to the Angayucham terrane.* Group 1 samples (Alatna river outcrop and the Koyukuk river conglomerate clasts) lack the subduction zone signature of depleted  $HFSE_N$  and  $HREE_N$  relative to elevated  $LILE_N$  and  $LREE_N$ . The N-MORB and E-MORB chemistry of Group 1 suggests that these samples were formed in an extensional (sea-floor spreading) setting, similar to what has been proposed for the Angayucham terrane (e.g. Pallister et al., 1989). Immobile elements and N-MORB normalized REE diagrams show that the Group 1 samples have minor and trace element concentrations similar to the Angayucham terrane (Jurassic and Triassic units). Also, samples VP16-22a, VP16-22b (Group 1a), and VP16-22c (Group 1b) were collected from an outcrop with a geological description that matches the Angayucham terrane, so despite the lack of absolute age control for Group 1, the geological setting and geochemistry are consistent with the Angayucham terrane. Thus the similarities in trace element chemistry between the Koyukuk river clasts and the Alatna river (Angayucham) outcrop samples suggests that the former were likely eroded from the later, and not from the KAT. This also implies that the Angayucham terrane is comprised of both E-MORB and N-MORB magmatism. The lack of existing isotopic data from the Angayucham terrane prevents a correlation with the Nd data from this study. However,  $\epsilon Nd$  values of Group 1a and Group 1b are similar to what has been obtained from existing seamounts in the Pacific Ocean, which agrees with Pallister et al. (1989) who interpreted the chemistry of Angayucham terrane as similar to seamount basalts (e.g. Pallister et al., 1989).

## 7.4 Triassic-Jurassic island arc magmatism

*Triassic magmatism.* The whole-rock and isotope geochemistry suggests that the samples from Groups 3 and 4 represent tholeiitic and calc-alkalic Triassic magmatism formed in a relatively mature island arc setting. Since calc-alkalic magmas are known to be produced in the later stages of island arc development when steady-state subduction has been established, they are a characteristic feature of a mature island arc (Escuder Viruete et al., 2006; Wilson, 2007). The Triassic age (213 Ma) clearly predates the Jurassic arc magmatism and is older than any previously reported ages for island arc affinity rocks in the region, such as the KAT (Figure 13). They also predate the Brooks Range ophiolite, which Box et al. (2019) previously suggested could represent the forearc to the KAT. This suggests that Groups 3 and 4 represent debris eroded from a Triassic island arc, and not from the KAT.

*Jurassic magmatism.* The whole-rock and isotope geochemistry suggests that the samples from Groups 2 and 5 represent tholeiitic to calc-alkalic Jurassic magmatism formed from melting of an already depleted mantle wedge. Their c. 195 Ma age is similar to those reported for gabbroic clasts from the KKB conglomerate by O'Brien et al. (2017) which predates both the KAT and the Brooks Range ophiolite (Figure 13). This is consistent with Groups 2 and 5 representing debris eroded from an older Jurassic island arc (as previously proposed in O'Brien et al., 2017), and not from the KAT.

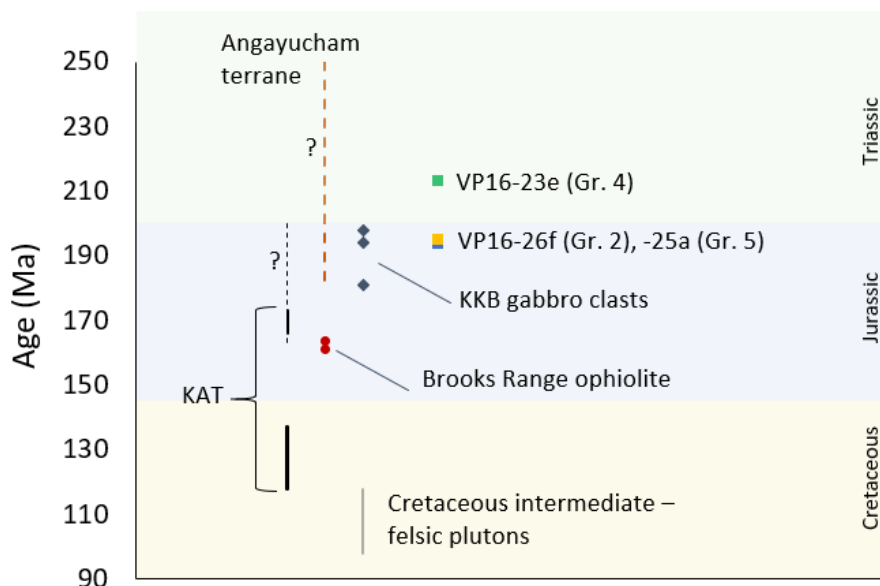


Figure 13. Age summary. Ages of igneous terranes near the KKB. Note that the U-Pb ages of this study are similar to ages of KKB gabbro clasts in O'Brien et al. (2017). Dashed lines represent the poorly constrained age data of the Angayucham terrane (fossil ages from Pallister et al., 1989). KAT age data (K-Ar ages from Box & Patton, 1989) - dashed lines represents the poorly constrained age data of Unit 1 (fossil ages). Brooks Range ophiolite (U-Pb ages of Box et al., 2019). Cretaceous intermediate to felsic plutons (U-Pb and K-Ar ages of Miller, 1989 and Roeske et al., 1995, 1998).

*Triassic-Jurassic island arc setting.* The Jurassic magmatism of Groups 2 and 5 postdates the Triassic arc magmatism (Groups 3 and 4), thus these two sets of Groups represent at least two magmatic events. However, the similarity in their tectonic formational environment (oceanic island arc setting) and isotope geochemistry (similar initial  $\epsilon\text{Nd}$  values) suggests that there may be a link between the Jurassic Groups and the Triassic Groups. The depleted nature of the Jurassic Groups suggests they formed by continued melting of a mantle wedge that was already depleted due to earlier melt extractions, such as the mantle wedge from which the Triassic magmas were derived. Thus, it may be implied that Groups 2, 3, 4 and 5 belong to the same island arc system, which due to slab rollback progressed from Triassic tholeiitic and calc-alkalic island arc magmatism to Jurassic tholeiitic and calc-alkalic magmatism. Subduction zones are not fixed in space and slab rollback occurs when the subducting plate retreats from the overriding plate - this can be caused by several factors such as changes in convergence rate between the overriding and subducting plates, increasing age/density of the subducting oceanic plate and/or increasing slab length (e.g. Royden, 1993; Schellart, 2005; Ring et al., 2010). When a subduction zone retreats the subduction induced magmatism will follow and this can cause the evolutionary pattern of an island arc system to go from tholeiitic to calc-alkalic magmatism and then return to tholeiitic and calc-alkalic magmas. This hypothetical scenario (Figure 14) might explain the Triassic-Jurassic island arc magmatism documented by the KKB conglomerate clasts.

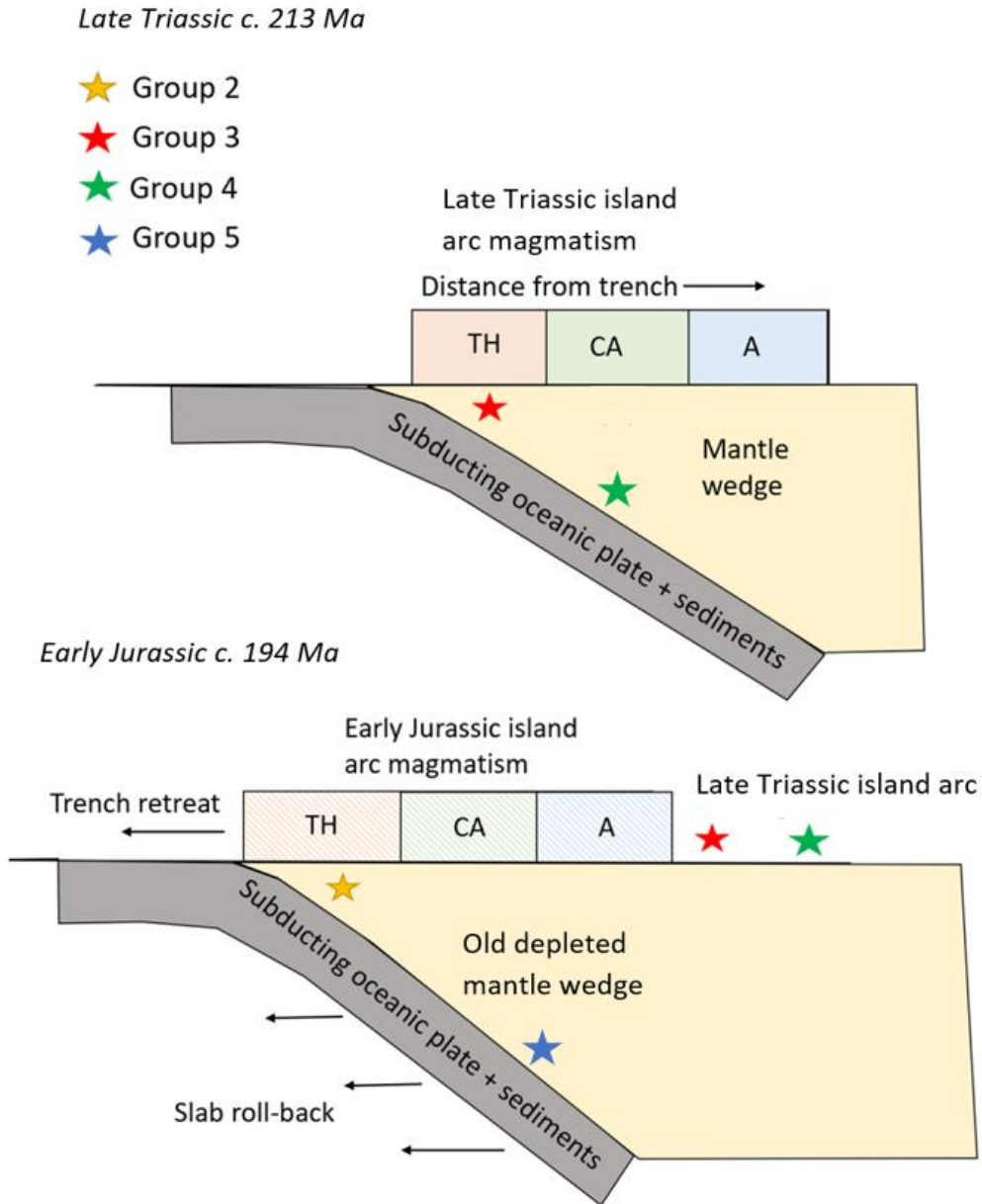


Figure 14. Schematic cross-section of a model for a retreating subduction zone. A Late Triassic arc initiates at c. 213 Ma (Group 3 and Group 4) producing tholeiitic and calc-alkalic magmatism. The mantle wedge is depleted by melt extraction related to the Triassic arc. At c. 194 Ma in the Early Jurassic, slab roll-back/retreat results in an arc shift, generating the more depleted tholeiitic and calc-alkalic/alkalic magmatism of Group 2 and 5, respectively. Note the relative positions of the Groups with distance from the trench and the approximate depth of melting. Subduction polarity is unknown. The figure is adapted from Wilson (2007).

## 7.5 KKB source terranes

It seems clear that Group 3 tholeiites and Group 4 calc-alkaline samples represent a relatively mature island arc of Late Triassic age and is unlikely to be related to the KAT. Groups 2 and 5 might represent continued depleted island arc magmatism of the same mantle wedge and subduction system as for the Triassic island arc. The Early Jurassic ages of Groups 2 and 5 are too old to be related to either the KAT or the Brooks Range ophiolite (previously inferred to be the forearc to the KAT). The results from this study support the tectonic model of Miller & Hudson (1991) and O'Brien et al. (2017), who proposed that a Triassic – Jurassic island arc system collided with the North American continental margin and initiated the formation of the Brooks Range fold and thrust belt. The missing source terrane of the conglomerate clasts from this and O'Brien et al.'s (2017) study may be buried beneath the basin or could have been totally stripped away by erosion, leaving only the buried clasts behind. The poorly constrained ages for the Angayucham terrane (Group 1), the missing source terrane to the Late Triassic- Early Jurassic island arc material (Group 2-5), and the differences in tectonic formation environments makes it difficult to infer a possible relationship between these source terranes.

Further research, including better age constraints and isotopic analyses, on the Angayucham terrane is needed to get a better understanding of its genesis and relationship with the Triassic-Jurassic island arc. This could be accomplished by analyzing the small zircons found in the Group 1 samples for U-Pb geochronology (too small to be analyzed with LA-ICP-MS) using a high-resolution technique such as secondary ion mass spectrometry (SIMS), which can reduce the spot size diameter (ion beam) down to only 10  $\mu\text{m}$ . From the lead isotopic data in this study it is suggested that future analyses are likely to be improved by acid leaching to avoid lead contamination and ambiguous data.

## 8. Conclusions

The aim of this study was to test the hypothesis that the clasts in the Cretaceous Kobuk Koyukuk basin conglomerate are erosional products of the Middle Jurassic to Early Cretaceous Koyukuk Arc terrane. Integration of whole-rock and isotope geochemistry, together with U-Pb zircon geochronology, suggests following:

- Whole-rock geochemistry indicates that the mafic igneous conglomerate clasts from the Kobuk Koyukuk basin sampled along the Koyukuk River are likely erosional products from the Angayucham terrane and confirm that the KKB clasts require at least two different source terranes.
- The KKB conglomerate clasts sampled along the Alatna River represent at least two episodes of arc magmatism, one of Late Triassic age and another of Early Jurassic age.
- The KKB conglomerate clasts do not correlate with the known ages of the Koyukuk Arc terrane (Box & Patton, 1989) and thus the hypothesis that the Kobuk Koyukuk igneous clasts are erosional products of the Late Jurassic- Early Cretaceous Koyukuk Arc terrane is rejected.
- The Late Triassic and Early Jurassic island arc magmatism documented by the KKB conglomerate clasts is consistent with the tectonic models of Miller & Hudson (1991) and O'Brien et al. (2017) which indicate a Jurassic-Triassic island arc colliding with the North American passive margin.
- Further research into the Angayucham terrane is needed to understand its genesis and possible relationship to the Triassic-Jurassic island arc terrane. High resolution techniques such as SIMS could be used for U-Pb dating of the small and few zircons present in mafic rocks.

## Acknowledgements

I would like to thank following people for helping me accomplish this master thesis: my supervisor Victoria Pease for the, as always, professional guidance and for giving me the opportunity to continue working on this exciting area; my co-supervisor Emelie Axelsson for helping me complete the zircon geochronology, teaching me how to manage the stubborn LA-ICP-MS and for being the best possible support; Kerstin Lindén at the Swedish Museum of Natural History for taking the time helping me with the SEM preparation; Stephen Box at the United States Geological Survey for the helpful communications and for letting me take part of new age data from the Brooks Range ophiolite and Koyukuk Arc terrane; Arne Lif, Krister Junghahn, Otto Hermelin, Elisabeth Däcker and other personnel at the Department of Geological Sciences at Stockholm University and of course all my classmates. Finally, thanks to my boyfriend Daniel Hellman for putting up with me during all the ups and downs, and for always believing in me.

This work has received additional funding from the Ymer-80 foundation and the Stockholm Geologists Foundation with contribution from the Gavelin fund.

## References

- Armstrong, R. L., Forbes, R. B., Evans, B. W., and Thurston, S. P. (1986). Rb-Sr and K-Ar study of Metamorphic rocks of the Seward Peninsula and Southern Brooks-Range, Alaska: Mem. Geol. Soc. Am., v. 164, p. 185-203.
- Bailie, R., Gutzmer, J. and Rajesh, H. (2011). Petrography, geochemistry and geochronology of the metavolcanic rocks of the Mesoproterozoic Leerkrans Formation, Wilgenhoutsdrif Group, South Africa – back-arc basin to the Areachap volcanic arc. *South African Journal of Geology*, V. 114 (2), p. 167-194.
- Box, S.E., Moore, T.E., Aleinikoff, J.N., Wirth, K.R., Wang, D. and Nelson, S.W. New zircon U-Pb ages and Hf isotopes from Brooks Range ophiolite and Koyukuk arc, the upper plate of the Brookian orogen [abstract]. In: Cordilleran Section - 115th Annual Meeting; 2019. Abstract nr: 329067
- Box, S.E., and Patton, W.W., Jr. (1989). Igneous history of the Koyukuk terrane, western Alaska: Constraints on the origin, evolution, and ultimate collision of an accreted island arc terrane: *Journal of Geophysical Research*, v. 94, p. 15,843–15,867, <https://doi.org/10.1029/JB094iB11p15843>
- Chiaradia, M., Müntener, O., Beate, B. and Fontignie, D. (2009). Adakite-like volcanism of Ecuador: lower crust magmatic evolution and recycling. *Contributions to Mineralogy and Petrology*, V.158(5), p.563–588.
- Christiansen, P. P. & Snee, L. W. (1994). Structure, metamorphism, and geochronology of the Cosmos Hills and Ruby Ridge, Brooks Range schist belt, Alaska: *Tectonics*, v.13, p. 193–213.
- Corfu, F., Hanchar, J.M., Hoskin, P. W. O. and Kinny, P. (2003). Atlas of zircon textures, *in* Hanchar, J. M., and Hoskin, P. W. O., eds., *Zircon: Reviews in Mineralogy and Geochemistry*, Mineralogical Society of America, 53, p. 468-500.
- Cox, K. G., Bell, J. D. and Pankhurst, R. J. (1979). *The interpretations of igneous rocks*. George, Allen and Unwin, London.
- DePaolo, D. J., & Wasserburg, G. J. (1976). Nd isotopic variations and petrogenetic models. *Geophysical Research Letters*, v. 3 (5), p.249-252.
- Elburg, M., Foden, J., van Bergen, M. and Zulkarnain, I. (2005). Australia and Indonesia in collision: geochemical sources of magmatism. *Journal of Volcanology and Geothermal Research*, V. 140(1-3), p.25-47. doi: 10.1016/j.jvolgeores.2004.07.014
- Ellam, R. (2016). *Isotopes: A Very Short Introduction*. 1st ed. Oxford University Press, p.108.
- Escuder Viruete, J., Díaz de Neira, A., Hernáiz Huerta, P., Monthel, J., Senz, J., Joubert, M., Lopera, E., Ullrich, T., Friedman, R. and Mortensen, J. (2006). Magmatic relationships and ages of Caribbean Island arc tholeiites, boninites and related felsic rocks, Dominican Republic. *Lithos*, V. 90(3–4), p. 161–186.
- Faure, G. (1986). *Principles of isotope geology*. 2nd ed. New York, N.Y.: Wiley, p. 309-335.
- Faure, G., & Mensing, T. M. (2005). *Isotopes Principles and Applications*. 3rd ed., New Jersey: John Wiley & Sons, INC., p. 40-42, 218-221.

Fitton, J. (2007). The OIB paradox. In: G. Foulger and D. Jurdy, ed., *Plates, plumes, and planetary processes*, 1st ed. Colorado: The Geological Society of America, Inc., p.387-407.

Fredriksson, C. (2017). *A Geochemical Study of Conglomerate Clasts from the Yukon-Koyukuk Basin and Their Tectonic Origin*. Undergraduate. Stockholm University.

Gale, A., Dalton, C., Langmuir, C., Su, Y. and Schilling, J. (2013). The mean composition of ocean ridge basalts. *Geochemistry, Geophysics, Geosystems*, V. 14(3), p.489-518.

Gerya, T. (2011). Intra-oceanic Subduction Zones. In: D. Brown and P. Ryan, ed., *Arc-Continent Collision*, 1st ed. Berlin: Springer-Verlag Berlin Heidelberg, p. 23-51.

Gottschalk, R. R., Oldow, J.S., and Avé Lallemant, H.G. (1998). Geology and Mesozoic structural history of the south-central Brooks Range, Alaska, in Oldow, J.S., and Avé Lallemant, H.G., eds., *Architecture of the Central Brooks Range Fold and Thrust Belt, Arctic Alaska*: Boulder, Colorado, Geological Society of America Special Paper 324.

Greene, A., DeBari, S., Kelemen, P., Blusztajn, J. and Clift, P. (2006). A Detailed Geochemical Study of Island Arc Crust: the Talkeetna Arc Section, South–Central Alaska: *Journal of Petrology*, v. 47(6), p.1051-1093.

Hanano, D., Weis, D., Scoates, J., Aciego, S. and DePaolo, D. (2010). Horizontal and vertical zoning of heterogeneities in the Hawaiian mantle plume from the geochemistry of consecutive postshield volcano pairs: Kohala-Mahukona and Mauna Kea-Hualalai. *Geochemistry, Geophysics, Geosystems*, V. 11(1). doi: 10.1029/2009GC002782

Harris, R. (2004). Tectonic evolution of the Brooks Range ophiolite, northern Alaska: *Tectonophysics*, v. 392 (1-4), p. 143-163. doi: 10.1016/j.tecto.2004.04.021

Harris, R.A., (1995). Geochemistry and tectonomagmatic affinity of the Misheguk massif, Brooks Range ophiolite, Alaska: *Lithos*, v. 35, p. 1–25, [https://doi.org/10.1016/0024-4937\(94\)00048-7](https://doi.org/10.1016/0024-4937(94)00048-7)

Harris, R.A. (1992). Peri-collisional extension and the formation of Oman-type ophiolites in the Brooks Range and Banda arc. In: L.M. Parsons, B.J. Murton and P. Browning (Editors), *Ophiolites and Their Modern Oceanic Analogues*. Geol. Soc. London, Spec. Publ., 60, p. 301-325.

Hart, S. R. (1984). A large-scale isotope anomaly in the southern hemisphere mantle. *Nature*, 309, p. 753-757.

Hastie, A., Kerr, A., Pearce, J. and Mitchell, S. (2007). Classification of Altered Volcanic Island Arc Rocks using Immobile Trace Elements: Development of the Th–Co Discrimination Diagram. *Journal of Petrology*, V. 48(12), p. 2341-2357.

Hauff, F., Hoernle, K. and Schmidt, A. (2003). Sr-Nd-Pb composition of Mesozoic Pacific oceanic crust (Site 1149 and 801, ODP Leg 185): Implications for alteration of ocean crust and the input into the Izu-Bonin-Mariana subduction system. *Geochemistry, Geophysics, Geosystems*, V. 4(8).

Hémond, C., Hofmann, A., Vlastélic, I. and Nauret, F. (2006). Origin of MORB enrichment and relative trace element compatibilities along the Mid-Atlantic Ridge between 10° and 24°N. *Geochemistry, Geophysics, Geosystems*, V. 7 (12), p.1-22.

- Hoiland, C. W., Miller, E. L., & Pease, V. (2018). Greenschist facies metamorphic zircon overgrowths as a constraint on exhumation of the Brooks Range metamorphic core, Alaska: *Tectonics*, v. 37, p.3429–3455. <https://doi.org/10.1029/2018TC005006>
- Ishizuka, O., Yuasa, M., Tamura, Y., Shukuno, H., Stern, R., Naka, J., Joshima, M. and Taylor, R. (2010). Migrating shoshonitic magmatism tracks Izu–Bonin–Mariana intra-oceanic arc rift propagation. *Earth and Planetary Science Letters*, V. 294(1-2), p.111-122. doi: 10.1016/j.epsl.2010.03.016
- Janney, P. and Castillo, P. (1999). Isotope geochemistry of the Darwin Rise seamounts and the nature of long-term mantle dynamics beneath the south central Pacific. *Journal of Geophysical Research: Solid Earth*, V. 104(B5), p.10571–10589.
- Jicha, B. R., Singer, B. S., Brophy, J. G., Fournelle, J. H., Johnson, C. M., Beard, B. L., Lapen, T. J., and Mahlen, N. J. (2004). Variable Impact of the Subducted Slab on Aleutian Island Arc Magma Sources: Evidence from Sr, Nd, Pb, and Hf Isotopes and Trace Element Abundances. *Journal of Petrology*, V. 45(9), p. 1845–1875.
- Kessel, R., Schmidt, M., Ulmer, P. and Pettke, T. (2005). Trace element signature of subduction-zone fluids, melts and supercritical liquids at 120–180km depth. *Nature*, V. 437(7059), p. 724–727.
- Kubiak, A. (2017). *Provenance of mafic outcrops and igneous clasts in Kobuk-Koyukuk sub-basin conglomerates and basin formation from sample geochemistry*. Undergraduate. Stockholm University.
- Labanieh, S., Chauvel, C., Germa, A., and Quidelleur, X. (2012). Martinique: a Clear Case for Sediment Melting and Slab Dehydration as a Function of Distance to the Trench. *Journal of Petrology*, 53(12), p.2441-2464. doi: 10.1093/petrology/egs055
- Ludwig, K.R. (2012). Manual for Isoplot 3.75. *Berkeley Geochronology Center Special Publication 5*.
- Mayfield, C. F., TAILLEUR, I. L., MULL, C.G., and SILBERMAN, M.L., Granitic clasts from Upper Cretaceous conglomerate in the northwestern Brooks Range in U.S. Geological Survey in Alaska: Accomplishments during 1977, edited by Johnson, K.M., U.S. Geol. Surv. Circ., 772-B, Bll-B13, 1978.
- McDonough, W. F., & Chauvel, C. (1991). Sample contamination explains the Pb isotopic composition of some Rurutu island and Sasha seamount basalts. *Earth and Planetary Science Letters*, v. 105 (4), p. 397-404.
- Metcalf, R.V. & Shervais, J.W. (2008). Suprasubduction-zone ophiolites: Is there really an ophiolite conundrum? in Wright, J.E., and Shervais, J.W., eds., *Ophiolites, Arcs, and Batholiths: A Tribute to Cliff Hopson*: Geological Society of America Special Paper 438, p. 191–222, doi: 10.1130/2008.2438(07).
- Miller, E. L., & Hudson, T. L. (1991). Mid-Cretaceous extension fragmentation of a Jurassic–Early Cretaceous compressional orogen, Alaska: *Tectonics*, v. 10, p. 781–796, <https://doi.org/10.1029/91TC00044>
- Miller, T.P. (1989). Contrasting plutonic rock suites of the Yukon-Koyukuk Basin and the Ruby geanticline, Alaska: *Journal of Geophysical Research*, v. 94, p. 15,969–15,987, <https://doi.org/10.1029/JB094iB11p15969>

Moore, T. E., Aleinikoff, J. N., and Walter, M. (1993). Middle Jurassic U-Pb age for the Siniktanneyak Mountain ophiolite, Brooks Range, Alaska: Geological Society of America Abstracts with Programs, v. 25, p. 124.

Moore, T. E., & Box, S. E. (2016). Age, distribution and style of deformation in Alaska north of 60°N: Implications for assembly of Alaska: Tectonophysics, v. 691, p. 133–170, <https://doi.org/10.1016/j.tecto.2016.06.025>

Morrison, R., & Murphy, B. (2006). *Environmental forensics*. Amsterdam: Elsevier Academic Press, p.69-70.

Muñoz, J., Troncoso, R., Duhart, P., Crignola, P., Farmer, L. and Stern, C. (2000). The relation of the mid-Tertiary coastal magmatic belt in south-central Chile to the late Oligocene increase in plate convergence rate. *Revista geológica de Chile*, V. 27(2), p.177–203. doi: 10.4067/S0716-02082000000200003

Nilsen, T. H. (1989). Stratigraphy and sedimentology of the mid-Cretaceous deposits of the Yukon-Koyukuk Basin, west central Alaska: Journal of Geophysical Research, v. 94, p. 15,925–15,940, <https://doi.org/10.1029/JB094iB11p15925>

Nilsson, C. (2017). *The geochemical analysis of Yukon-Koyukuk basin clasts and their tectonic origin*. Undergraduate. Stockholm University.

O'Brien, T. M., Miller, E. L., Pease, V., Hayden, L. A., Fisher, C. M., Hourigan, J. K., et al. (2017). Provenance, U-Pb detrital zircon geochronology, Hf isotopic analyses, and Cr-spinel geochemistry of the northeast Yukon-Koyukuk Basin: Implications for interior basin development and sedimentation in Alaska. *GSA Bulletin*, V. 130(5–6), p. 825–847. <https://doi.org/10.1130/B31825.1>

O'Sullivan, P., Murphy, J., & Blythe, A. (1997). Late Mesozoic and Cenozoic thermotectonic evolution of the central Brooks Range and adjacent North Slope foreland basin, Alaska: Including fission track results from the Trans-Alaska Crustal Transect (TACT): Journal of Geophysical Research: Solid Earth, v. 102(B9), p. 20821-20845. doi:10.1029/96jb03411

Pallister, J., Budahn, J., and Murchey, B. (1989). Pillow basalts of the Angayucham terrane: Oceanic plateau and island crust accreted to the Brooks Range. *Journal of Geophysical Research: Solid Earth*, v. 94, p. 15901-15923.

Patton, W. W. Jr., & Box, S. E. (1989). Tectonic setting of the Yukon-Koyukuk Basin and its borderlands, western Alaska. *Journal of Geophysical Research: Solid Earth*, v. 94, p. 15807-15820.

Patton, W.W., Jr., Box, S. E., Moll-Stalcup, E. J., and Miller, T. P. (1994). Geology of west-central Alaska, in Plafker, G., and Berg, H. C., eds., *The Geology of Alaska: Boulder, Colorado, Geological Society of America, The Geology of North America*, v. G-1, p. 241-269.

Patton, W. W., Jr., Wilson, F. H., Labay, K. A., and Shew, N. (2009). Geologic Map of the Yukon-Koyukuk Basin, Alaska: U.S. Geological Survey Scientific Investigations Map 2909, scale 1:500,000, 26 p.

Paton, C., Woodhead, J.E., Hellstrom, J.C., Hergt, J.M., Greig, A., and Mass, R. (2010). Improved laser ablation U-Pb zircon geochronology through robust downhole fractionation correction: *Geochemistry, Geophysics, Geosystems*, v. 11, Q0AA06, <https://doi.org/10.1029/2009GC002618>

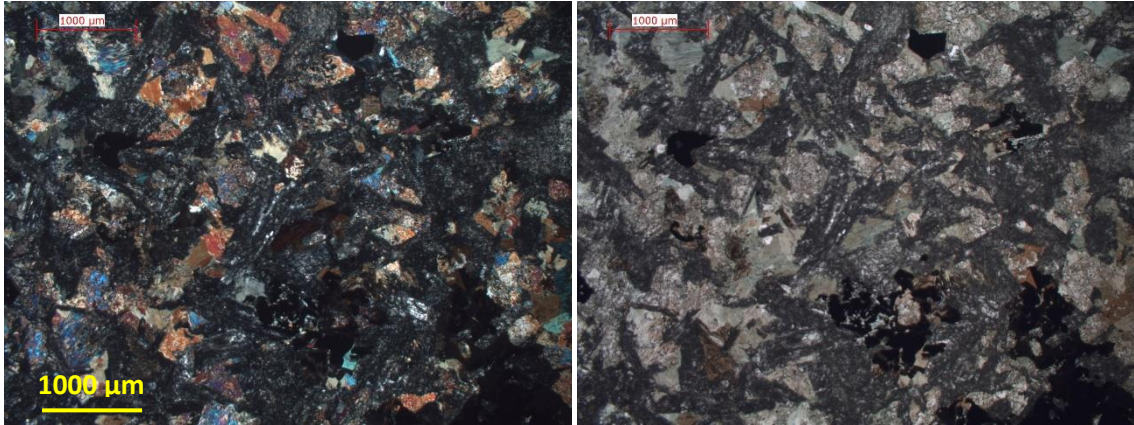
- Pearce, J. & Cann, J. (1973). Tectonic setting of basic volcanic rocks determined using trace element analyses. *Earth and Planetary Science Letters*, V. 19 (2), p. 290-300.
- Pearce, J.A. (1982). Trace element characteristics of lavas from destructive plate boundaries, in Thorpe, R.S., ed., *Andesites: Orogenic Andesites and Related Rocks*: Chichester, UK, John Wiley & Sons, p. 525–548.
- Pearce, J. A. (1996). A users guide to basalt discrimination diagrams. In: Wyman, D. A. (eds) *Trace Element Geochemistry of Volcanic Rocks: Applications for Massive Sulphide Exploration*. Geological Association of Canada, Short Course Notes 12, p. 79-113.
- Petrus, J., & Kamber, B. (2012). VizualAge: A Novel Approach to Laser Ablation ICP-MS U-Pb Geochronology Data Reduction. *Geostandards and Geoanalytical Research*, p. 1-24.
- Plafker, G., Nokleberg, W. J. & Lull, J. S. (1989). Bedrock geology and tectonic evolution of the Wrangellia, Peninsular, and Chugach terranes along the Trans-Alaskan Crustal Transect in the northern Chugach Mountains and southern Copper River basin, Alaska: *Journal of Geophysical Research*, v. 94, p. 4255–4295.
- Regelous, M., Hofmann, A., Abouchami, W. and Galer, S. (2003). Geochemistry of Lavas from the Emperor Seamounts, and the Geochemical Evolution of Hawaiian Magmatism from 85 to 42 Ma. *Journal of Petrology*, V. 44(1), p.113–140.
- Ring, U., Glodny, J., Will, T. and Thomson, S. (2010). The Hellenic Subduction System: High-Pressure Metamorphism, Exhumation, Normal Faulting, and Large-Scale Extension. *Annual Review of Earth and Planetary Sciences*, V. 38(1), p.45-76.
- Roeske, S. M., Dusel-Bacon, C., Aleinikoff, J.N., Snee, L.W., and Lanphere, M.A. (1995). Metamorphic and structural history of continental crust at a Mesozoic collisional margin, the Ruby terrane, central Alaska: *Journal of Metamorphic Geology*, v. 13, p. 25–40, <https://doi.org/10.1111/j.1525-1314.1995.tb00203.x>
- Roeske, S. M., McClelland, W. C., and Koepfele, P. (1998). Late Early Cretaceous transtension in the Ruby terrane, west-central Alaska: *Geological Society of America Abstract Programs*, v. 30 (7), p. 176.
- Rollinson, H. (1993). *Using geochemical data: evaluation, presentation, interpretation*. 1st ed. New York: Routledge, p.233-242.
- Royden, L. (1993). Evolution of retreating subduction boundaries formed during continental collision. *Tectonics*, V. 12(3), p.629–638.
- Schellart, W. (2005). Influence of the subducting plate velocity on the geometry of the slab and migration of the subduction hinge. *Earth and Planetary Science Letters*, V. 231(3–4), p.197-219.
- Schoene, B. (2014). U-Th-Pb Geochronology, in Holland, H. D, & Turekian, K. K., eds., *Treatise on Geochemistry*, v. 4, p. 341-378. Princeton: Elsevier Ltd. DOI: <http://dx.doi.org/10.1016/B978-0-08-095975-7.00310-7>

- Singer, B., Jicha, B., Leeman, W., Rogers, N., Thirlwall, M., Ryan, J. and Nicolaysen, K. (2007). Along-strike trace element and isotopic variation in Aleutian Island arc basalt: Subduction melts sediments and dehydrates serpentine. *Journal of Geophysical Research*, V. 112(B6). DOI: 10.1029/2006JB004897
- Stern, R., Kohut, E., Bloomer, S., Leybourne, M., Fouch, M. and Vervoort, J. (2006). Subduction factory processes beneath the Guguan cross-chain, Mariana Arc: no role for sediments, are serpentinites important? *Contributions to Mineralogy and Petrology*, V. 151(2), p. 202–221.
- Sun, S.S. and McDonough, W.F. (1989). Chemical and isotopic systematics of oceanic basalts; implications for mantle composition and processes. *Magmatism in the ocean basins*. Saunders, A.D. and Norry, M.J. (Editors), Geological Society of London, London, no. 42, p. 313-345.
- Till, A. B., Box, S. E., Roeske, S. M., & Patton, W. W. Jr. (1993). Comment on “Mid-Cretaceous extensional fragmentation of a Jurassic-Early Cretaceous compressional orogen, Alaska” by E. L. Miller and T. L. Hudson. *Tectonics*, v. 12(4), p. 1076–1081. <https://doi.org/10.1029/93TC00671>
- Till, A. B., Schmidt, J. M., & Nelson, S. W. (1988). Thrust involvement of metamorphic rocks, southwestern Brooks Range, Alaska. *Geology*, v. 16(10), p. 930–933. [https://doi.org/10.1130/0091-7613\(1988\)016<0930:TOMRS>2.3.CO;2](https://doi.org/10.1130/0091-7613(1988)016<0930:TOMRS>2.3.CO;2)
- Todd, E., Stracke, A. and Scherer, E. E. (2015). Effects of simple acid leaching of crushed and powdered geological materials on high-precision Pb isotope analyses. *Geochemistry, Geophysics, Geosystems*, v. 16 (7), p. 2276-2302, doi:10.1002/2015GC005804
- Todt, W., Cliff, R., Hanser, A., and Hofmann, A. (1996). Evaluation of a  $^{202}\text{Pb}$  -  $^{205}\text{Pb}$  double spike for high - Precision lead isotope analysis, in Basu, A., and Hart, S., eds., *Geophysical Monograph Series*, V. 95. American Geophysical Union. DOI: 10.1029/GM095
- Toro, J., Cole, F., & Meier, J. (1996).  $^{40}\text{Ar}/^{39}\text{Ar}$  Ages of Detrital Minerals in Lower Cretaceous Rocks of the Okpikruak Formation: Evidence for Upper Paleozoic Metamorphic Rocks in the Koyukuk Arc: US Geological Survey Professional Paper, (1595), p. 169–182.
- Turner, D. L., Forbes, R. B. & Dillon, J. T. (1979). K-Ar geochronology of the southwestern Brooks Range, Alaska: *Canadian Journal of Earth Sciences*, v. 16(9), p. 1789–1804.
- Vogl, J. (2003). Thermal-baric structure and P-T history of the Brooks Range metamorphic core, Alaska: *Journal of Metamorphic Geology*, v. 21(3), p. 269-284. doi: 10.1046/j.1525-1314.2003.00440.x
- White, W., Hofmann, A. and Puchelt, H. (1987). Isotope geochemistry of Pacific Mid-Ocean Ridge Basalt. *Journal of Geophysical Research*, V.92(B6), p.4881- 4893.
- Wilbur, S. C., Siok, J. P., and Mull, C. G. (1987). A Comparison of two petrographic suites of the Okpikruak Formation: A point-count analysis, in *Alaskan North Slope Geology*, v. I, edited by I.Tailleur and P. Weimer, p. 441-447, Pacific Section, Society of Economic Paleontologists and Mineralogists, Bakersfield, Calif., 1987.
- Wilson, B. (2007). *Igneous Petrogenesis a Global Tectonic Approach*. Springer Science & Business Media, p.168.
- Wilson, M. (1989). *Igneous petrogenesis*. Unwin Hyman, London.
- Winchester, J. A., & Floyd, P. A. (1977). Geochemical discrimination of different magma series and their differentiation products using immobile elements. *Chemical Geology*, 20, p. 325-343.

Zachariah, J., Balakrishnan, S. and Rajamani, V. (1997). Significance of Sm-Nd isotope systematics in crustal genesis: A case study of Archaean metabasalts of the eastern Dharwar Craton. *Earth and Planetary Sciences*, V. 106 (4), p.361-367.

Zindler, A. & Hart, S. R. (1986). Chemical geodynamics. *Ann. Rev. Earth Planet. Sci.*, 14, p. 493-571.

## **Appendix A - Thin section descriptions and images.**

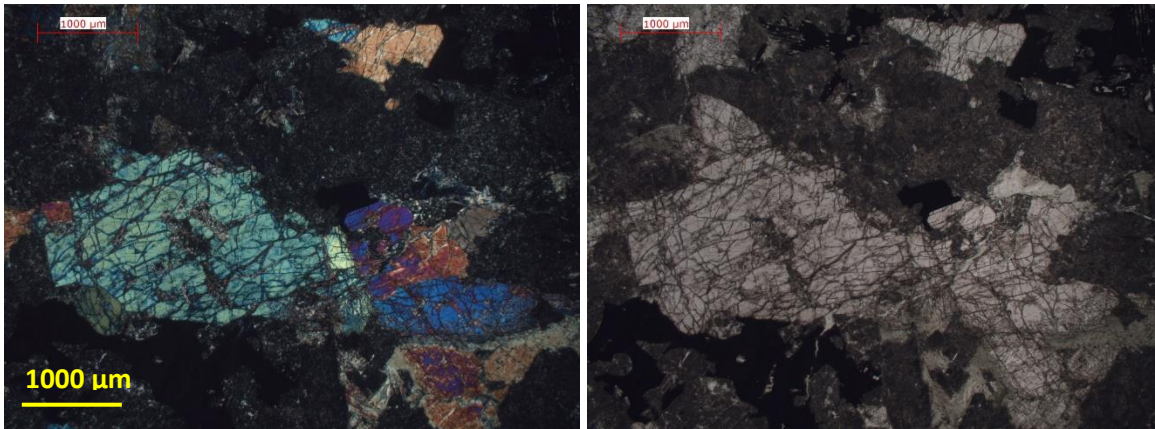


#### **VP15-10 Microgabbro**

**Hand specimen:** Medium grained phaneritic. Melanocratic, overall dark grey with light green patches (filled voids?).

**Thin section mineralogy:** Plagioclase, amphibole (hornblende and actinolite), pyroxene (CPX), opaques, chlorite and sericite.

**Texture and Alteration:** Intergranular texture with randomly oriented plagioclase laths partially enclosed by pyroxene and hornblende. The majority of minerals are anhedral. Heavy alteration of plagioclase to sericite. Uralitization of fractured pyroxene grains by secondary amphibole (actinolite) and chlorite. Voids filled with extremely fine grained unidentified secondary mineral.



#### **VP15-11 Basalt**

**Hand specimen:** Porphyritic with medium grained phenocrysts in a fine-grained aphanitic matrix. Mesocratic, light grey groundmass with light green and dark grey phenocrysts present.

**Thin section mineralogy:** Pyroxene (CPX), serpentine, chlorite, saussurite, amphibole (actinolite), titanite.

**Texture and Alteration:** Porphyritic texture with pyroxene phenocrysts. Pyroxene is commonly fractured and anhedral with serpentine filled cracks, some are completely serpentinized. Uralitization of pyroxene by secondary amphibole actinolite and chlorite. The groundmass is so fine grained it's hard to tell the mineralogy. Titanite is present as a late crystallizing phase with inclusions of the fine-grained groundmass.

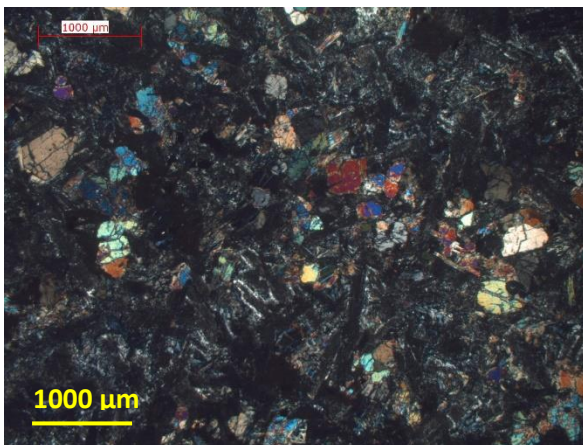


**VP15-12 Basalt**

**Hand specimen:** Medium grained phaneritic, melanocratic. Dark grey colored with areas of light green-white fillings, probably secondary filled vesicles.

**Thin section mineralogy:** Plagioclase, pyroxene (CPX), saussurite/sericite, serpentine, chlorite, amphibole (actinolite), titanite, opaques.

**Texture and alteration:** Subophitic and skeletal texture with large aligned skeletal plagioclase laths that are partially enclosed by pyroxene grains. Skeletal texture indicates fast cooling and disequilibrium, texture typical of volcanic rocks. Heavy sericitization of plagioclase laths. Subhedral titanite grains are present in the sample, some have inclusions of plagioclase which indicate that titanite crystallized later. Chlorite filled voids are present. The pyroxenes are relatively unaltered but are very fractured, and some have serpentine filled cracks and others have started to be replaced by actinolite to a minor degree. Devitrified glass fills interstices.

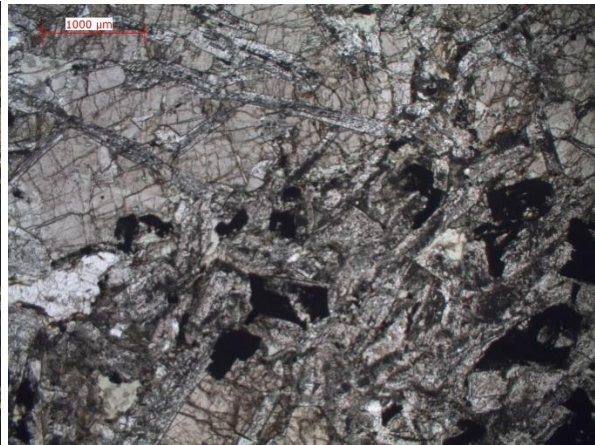
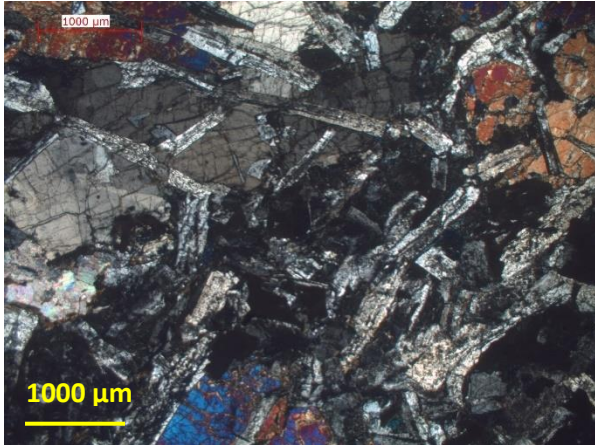


**VP15-13 Microgabbro**

**Hand specimen:** Medium grained phaneritic. Mesocratic, greenish-grey colored.

**Thin section mineralogy:** Plagioclase, pyroxene (CPX), chlorite, amphibole, sericite, amphibole (actinolite), prehnite.

**Texture and alteration:** Intergranular texture with randomly oriented plagioclase laths and small pyroxene grains filling the interstices. Heavy alteration of plagioclase to sericite. Pyroxene is generally fractured and relatively unaltered, some have been partly altered to chlorite and actinolite (uralitization). Prehnite is present in small amounts.

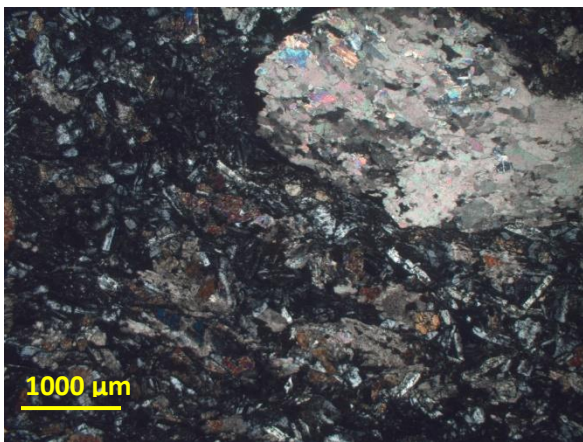


**VP16-22a Gabbro**

**Hand specimen:** Medium grained phaneritic. Mesocratic, light greenish-grey with dark grey spots.

**Thin section mineralogy:** Plagioclase, pyroxene (CPX), chlorite, calcite, sericite, devitrified glass, titanite.

**Texture and alteration:** Sub-ophitic texture with randomly oriented elongated skeletal plagioclase laths partially enclosed by pyroxene. The pyroxene grains are very fractured, some pyroxene grains are larger relative to the others. Plagioclase laths have been altered to sericite. Calcite aggregates fill voids.

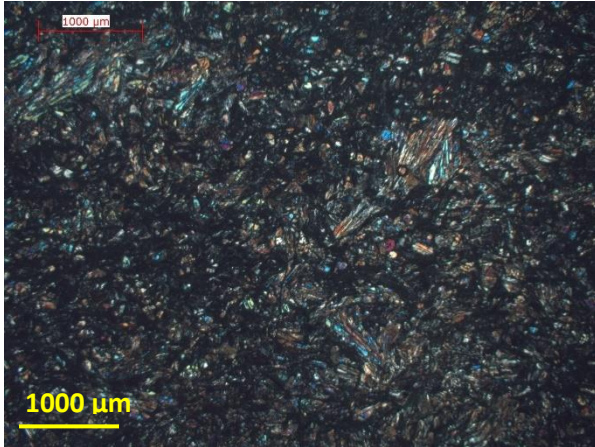


**VP16-22b Basalt**

**Hand specimen:** Medium grained phaneritic. Melanocratic, dark greenish-grey colored.

**Thin section mineralogy:** Plagioclase, pyroxene (CPX), calcite, chlorite, titanite.

**Texture and alteration:** Intergranular texture with secondary calcite filling voids after vesicles (amygdales). Chlorite filled voids are also present. Trachytic texture constituted by oriented skeletal plagioclase laths and small and fractured anhedral pyroxene grains.

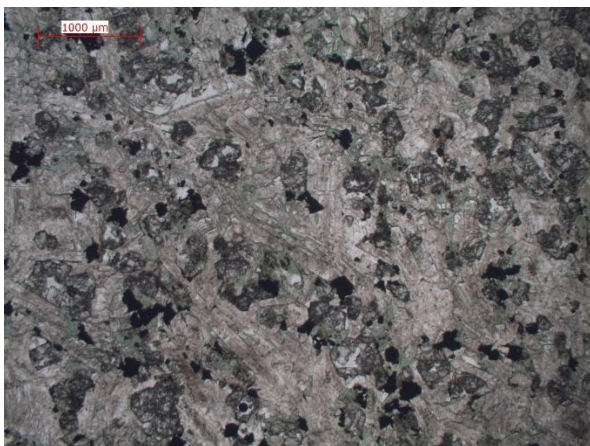
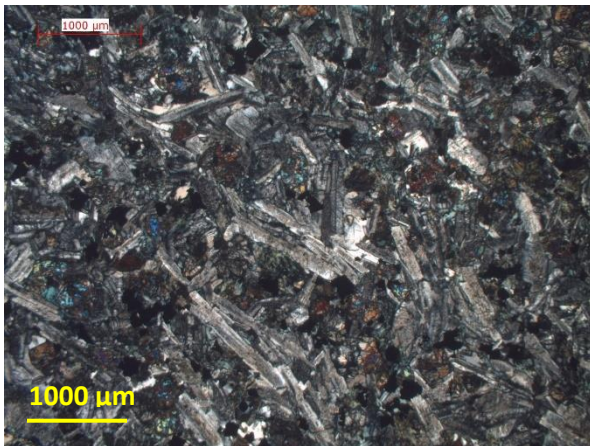


**VP16-22c Basalt**

**Hand specimen:** Fine grained aphanitic. Melanocratic, dark brownish-grey colored.

**Thin section mineralogy:** Pyroxene, plagioclase?

**Texture and alteration:** Skeletal pyroxene and probably some plagioclase indicating fast cooling and disequilibrium. Cryptocrystalline, hard to tell the mineralogy.

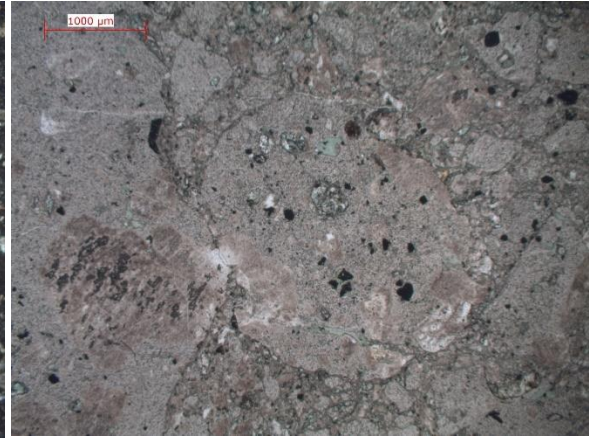
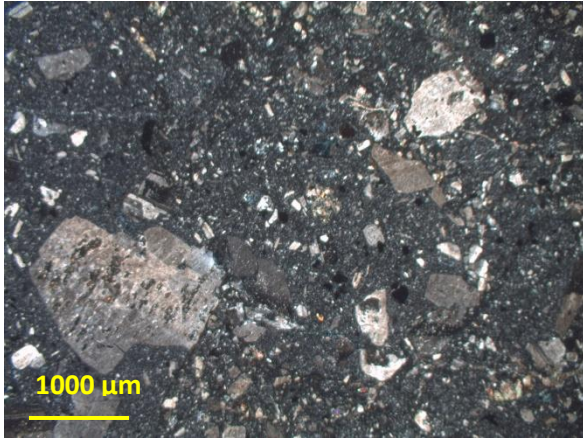


**VP16-23a Microgabbro**

**Hand specimen:** Medium grained phaneritic, melanocratic. Dark grey-pink colored.

**Thin section mineralogy:** Plagioclase, pyroxene (CPX), calcite, opaques, quartz, chlorite, epidote, sericite.

**Texture and alteration:** Equigranular and intergranular texture with trachytic plagioclase laths with small pyroxene grains filling the interstices. The primary mineralogy is dominated by plagioclase and small fractured pyroxene grains. Tiny quartz grains are common. Plagioclase laths are slightly altered to sericite and secondary calcite filled veins are common. Biotite has been completely replaced by chlorite.

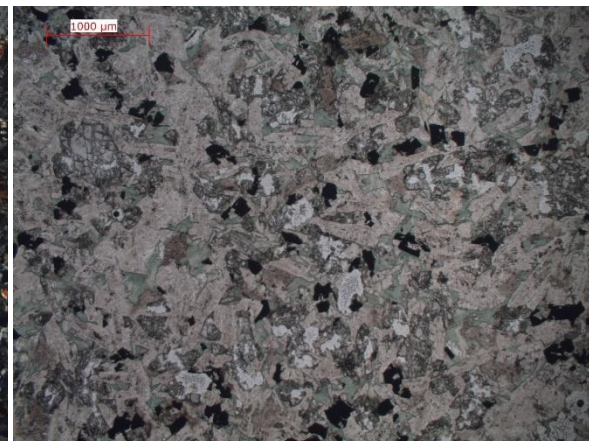
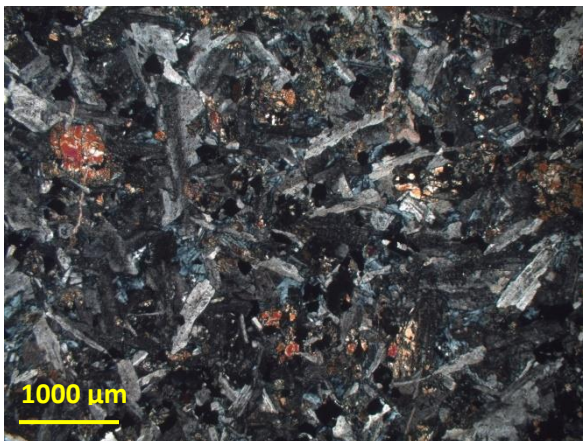


**VP16-23c Volcaniclastic breccia**

**Hand specimen:** Medium grained porphyritic grained with an aphanitic matrix, melanocratic. Dark grey matrix with some larger light pink colored mineral grains.

**Thin section mineralogy:** Plagioclase, alkali-feldspar, quartz, calcite, sericite, chlorite, epidote, opaques.

**Texture and alteration:** Porphyritic sample with an aphanitic matrix. Sub-angular to angular brecciated rock fragments constitute the sample. Subhedral to anhedral angular mineral grains of dominantly feldspars are present in a matrix of tiny quartz grains. Heavy alteration of the feldspar grains into sericite. Some unidentified grains have been completely altered to chlorite and calcite. Tiny epidote, opaque and calcite grains together with calcite filled veins are present in the sample. Chlorite is present in the whole sample where it mainly fills interstitial spaces in the matrix.

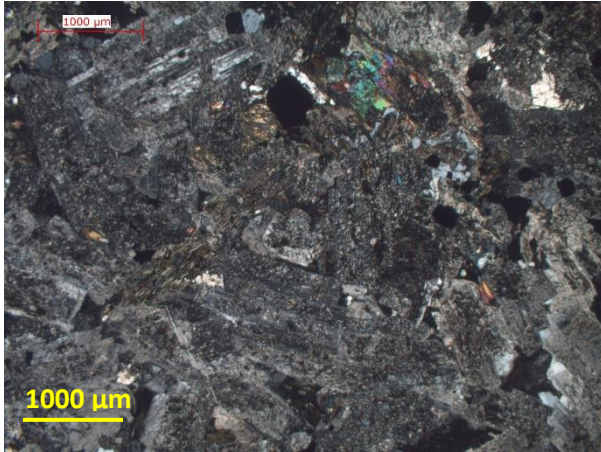


**VP16-23d Microgabbro**

**Hand specimen:** Medium grained phaneritic, melanocratic. Dark grey colored.

**Thin section mineralogy:** Plagioclase, pyroxene, calcite, opaques, chlorite, sericite.

**Texture and alteration:** Intergranular texture with small grains of pyroxene filling interstices in a random network of larger plagioclase laths. Calcite filled veins are very common. Some plagioclase laths have been slightly altered to sericite. Tiny and fractured grains of pyroxene are present in the whole sample. Calcite, sericite and chlorite indicate hydrothermal alteration.

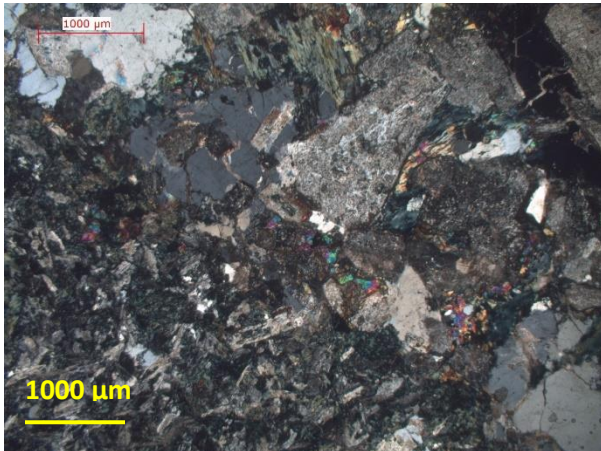


### **VP16-23e Diorite**

**Hand specimen:** Coarse grained phaneritic, mesocratic. Darker mineral grains mixed with light green-grey minerals and light pink colored minerals.

**Thin section mineralogy:** Plagioclase, alkali-feldspar, opaques, chlorite, prehnite, sericite/saussurite, calcite, amphibole, quartz, titanite.

**Texture and alteration:** Equigranular texture dominated by subhedral plagioclase and alkali-feldspar to some extent. Heavy alteration of feldspar grains to sericite. Biotite grains have been totally replaced by chlorite. Calcite veins are common.

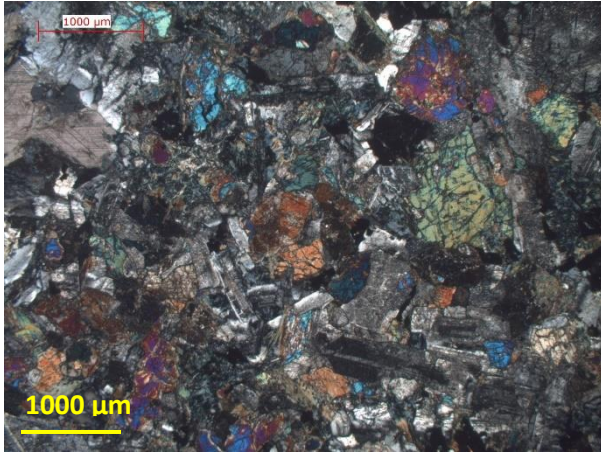


### **VP16-23g Granodiorite**

**Hand specimen:** Coarse grained phaneritic, mesocratic. Light grey with a green-yellowish tint.

**Thin section mineralogy:** Plagioclase, alkali-feldspar, quartz, chlorite, opaques, epidote, sericite, calcite.

**Texture and alteration:** The sample consist of a host rock that have a plutonic equigranular and interlocking texture that hosts an approximately 1 cm small xenolith. The host rock consists of large quartz and feldspar grains. Moderately alteration of feldspars to sericite and biotite has been completely altered to chlorite. The xenolith is fine grained aphanitic and has a felty texture of small randomly oriented plagioclase laths with abundant chlorite. Secondary calcite filled cracks and veins are common.

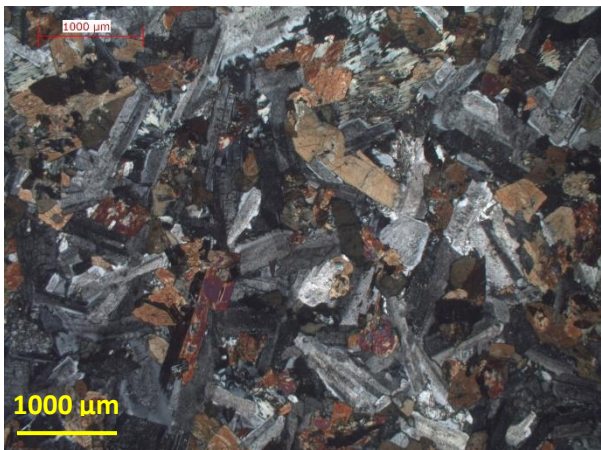


**VP16-24a gabbro**

**Hand specimen:** Medium grained phaneritic. Melanocratic with a dark greenish-grey color.

**Thin section mineralogy:** Plagioclase, pyroxene (CPX), actinolite, calcite, chlorite, quartz, sericite, opaques.

**Texture and alteration:** Equigranular and subophitic texture with randomly oriented plagioclase laths partially enclosed by pyroxene (CPX) grains. Heavy alteration of plagioclase to sericite and fractured pyroxene grains are started to be replaced by actinolite (uralitization) and chlorite. Tiny quartz grains and secondary calcite are common.

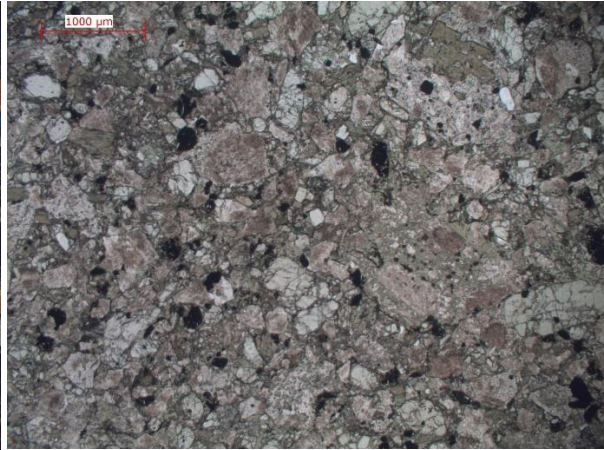
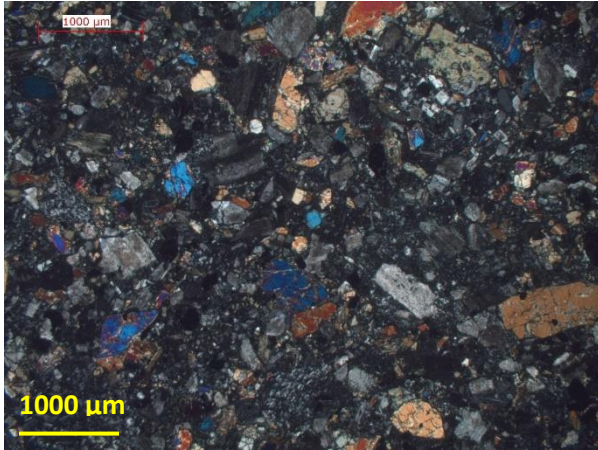


**VP16-24b Gabbro**

**Hand specimen:** Medium grained phaneritic. Melanocratic, dark grey with a yellow tint.

**Thin section mineralogy:** Plagioclase, Alkali-feldspar, amphibole (hornblende and tremolite-actinolite), pyroxene, chlorite, biotite, sericite, opaques, titanite.

**Texture and alteration:** Equigranular rock with randomly oriented plagioclase laths. Moderately alteration of plagioclase and Alkali-feldspar into sericite. Primary hornblendes are common. Fractured pyroxene grains are replaced by amphibole (uralite). The hornblende grains are started to be replaced by chlorite.

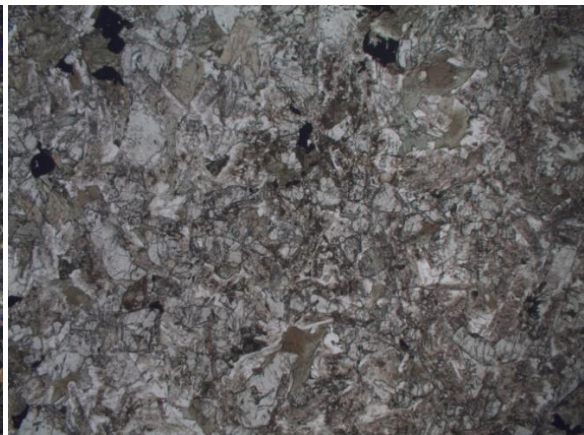
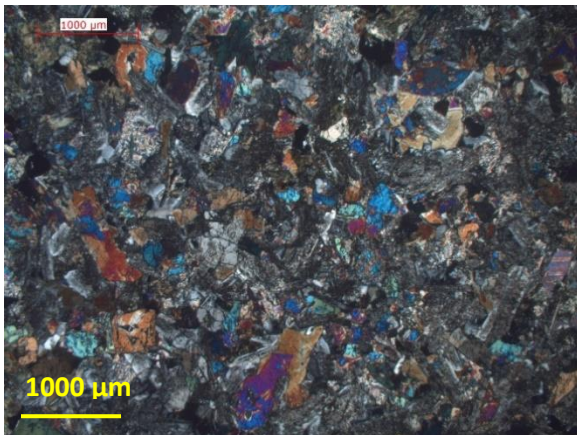


**VP16-24c Basalt**

**Hand specimen:** Medium grained porphyritic, melanocratic. Dark grey matrix with light grey-white phenocrysts.

**Thin section mineralogy:** Plagioclase, alkali-feldspar, pyroxene (CPX), olivine, calcite, sericite, chlorite, chert.

**Texture and alteration:** Porphyritic rock with abundant subhedral to anhedral pyroxene, feldspar and olivine with tiny epidote grains. Chlorite and devitrified glass fill the interstices and calcite veins are present. Moderately alteration of feldspars to sericite. The rock probably formed due to an explosive eruption evidenced by fractured crystals enclosed by lava (now devitrified glass).

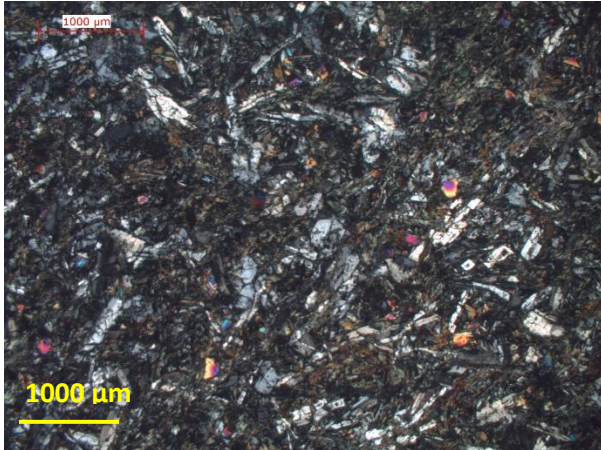


**VP16-24d Microgabbro**

**Hand specimen:** Medium grained phaneritic. Melanocratic that has a dark grey color with a yellowish tint.

**Thin section mineralogy:** Plagioclase, pyroxene (CPX), amphibole (hornblende), chlorite, calcite, opaques, sericite.

**Texture and alteration:** Equigranular and intergranular texture. Heavy seritization of plagioclase. The pyroxenes are fractured. Subhedral-anhedral hornblende are commonly replaced by chlorite at the rims.



**VP16-24e Basalt**

**Hand specimen:** Fine grained aphanitic, melanocratic.

**Thin section mineralogy:** Plagioclase and alkali-feldspar, actinolite, chlorite, opaques, epidote.

**Texture and alteration:** Equigranular and skeletal texture. Skeletal plagioclase indicates fast cooling and disequilibrium (common texture in volcanic rocks). Actinolite, fibrous chlorite and epidote grains are present in the whole sample.

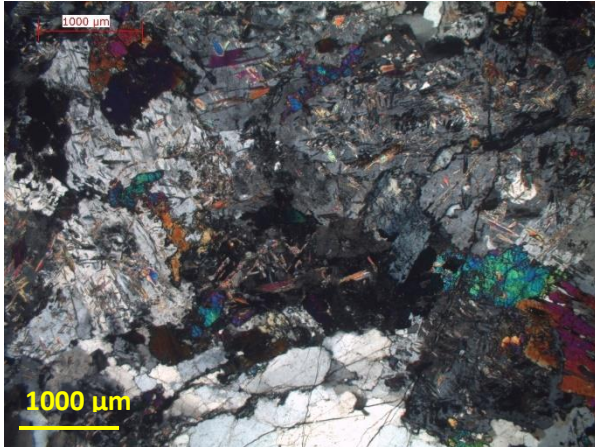


**VP16-24f Gabbro**

**Hand specimen:** Medium grained phaneritic. Melanocratic, darker grey minerals present together with dark green and light grey minerals.

**Thin section mineralogy:** Plagioclase, pyroxene (CPX), amphibole (actinolite), quartz, chlorite, calcite, opaques.

**Texture and alteration:** Equigranular and intergranular texture with randomly oriented plagioclase laths with pyroxenes filling the interstices. Moderate seritization of plagioclase. Fractured pyroxenes are common, some have rims replaced by actinolite (uralitization) and chlorite. Secondary calcite grains are common.

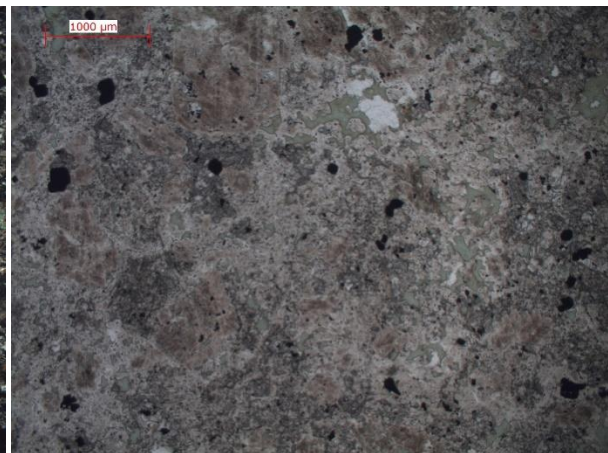
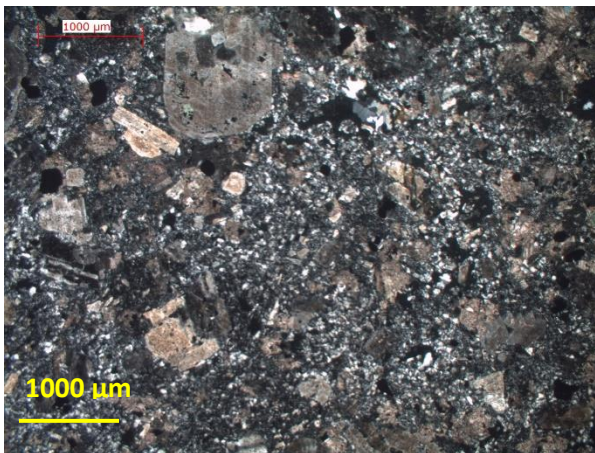


### **VP16-25a Granodiorite**

**Hand specimen:** Coarse grained phaneritic. Mesocratic, yellow/green tint.

**Thin section mineralogy:** Quartz, k-feldspar, plagioclase, clinzoisite/epidote, saussurite, chlorite, amphibole (hornblende), opaques, titanite.

**Texture and alteration:** Allotriomorphic (except for some single euhedral to subhedral amphibole grains). Feldspars are commonly altered to saussurite. Polycrystalline quartz is common. Epidote and clinzoisite are both common in the sample and occur as groups of anhedral grains. Very altered sample. Chlorite occurs in minor amounts when replacing biotite and in spaces between grains.

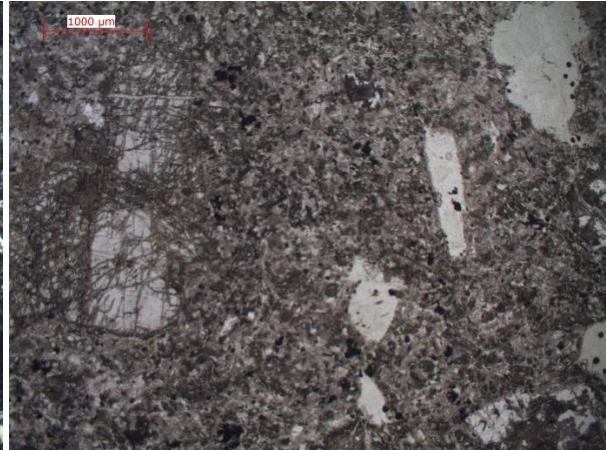
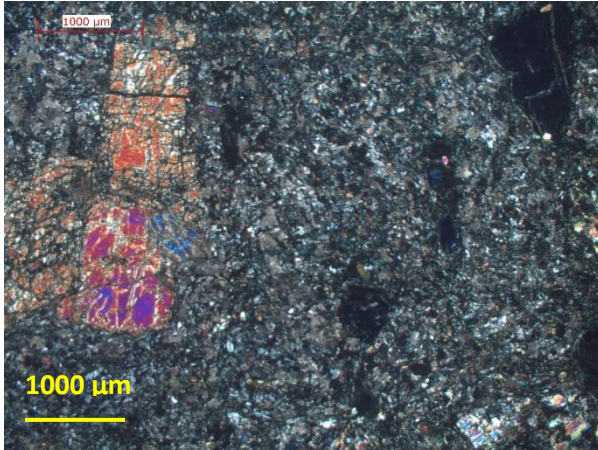


### **VP16-25b Andesite**

**Hand specimen:** Porphyritic texture with a fine grained matrix. Melanocratic with light pink/grey phenocrysts (1-5 mm) in an aphanitic dark grey colored matrix.

**Thin section mineralogy:** Calcite, quartz, feldspar (plagioclase and k-feldspar), chlorite, sericite, devitrified glass (anisotropic, dark in XPL light green in PPL), opaques.

**Texture and alteration:** Glomeroporphyritic texture with glomerophenocrysts of feldspars that has been strongly altered to sericite. Feldspar crystals are commonly embayed due to reaction with the melt (now devitrified glass). Calcite aggregates are common. Tiny quartz grain making up the groundmass together with chlorite and devitrified glass. Enclaves (trachytic texture) with mineralogy distinct from the groundmass indicate that magma mixing might have taken place.

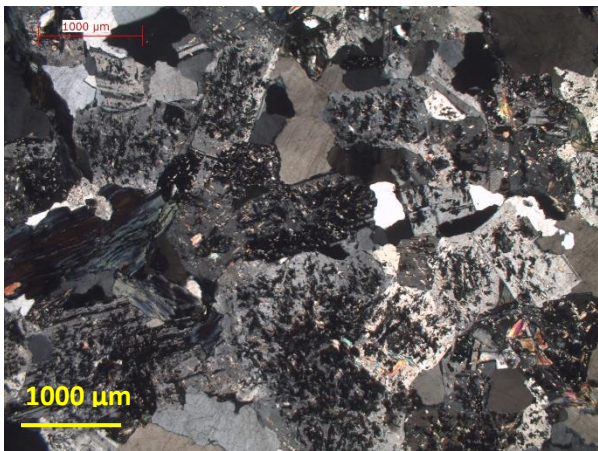


### **VP16-25c Basalt**

**Hand specimen:** Porphyritic texture with an aphanitic matrix. Melanocratic with light green yellowish and dark grey phenocrysts in a grey colored aphanitic matrix.

**Thin section mineralogy:** Pyroxene (CPX), plagioclase, chlorite prehnite, epidote, saussurite, sericite.

**Texture and alteration:** Volcanic rock with porphyritic-aphanitic texture. Fractured pyroxene phenocrysts in a fine grained aphanitic matrix of plagioclase microlites that have been heavy altered to saussurite/sericite, tiny epidote grains and prehnite. Some pyroxene crystals have been completely altered to berlin blue chlorite.

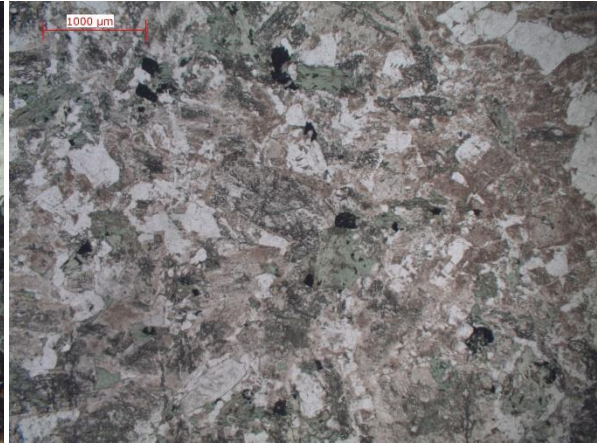
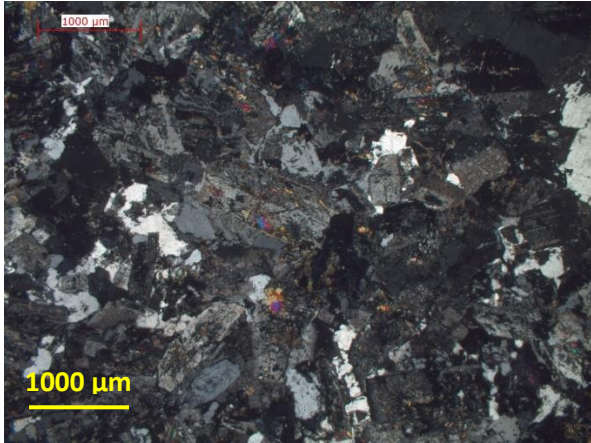


### **VP16-25d Granodiorite**

**Hand specimen:** Coarse grained phaneritic. Leucocratic light grey with a yellow-greenish tint, some dark grey minerals present.

**Thin section mineralogy:** Plagioclase and alkali-feldspar, quartz, amphibole, prehnite, chlorite, epidote, saussurite/sericite, titanite.

**Texture and alteration:** Equigranular, plutonic interlocking texture. Heavy alteration of feldspars to saussurite/sericite. Biotite has been altered to chlorite. Prehnite and epidote commonly occur between larger quartz and feldspar grains.

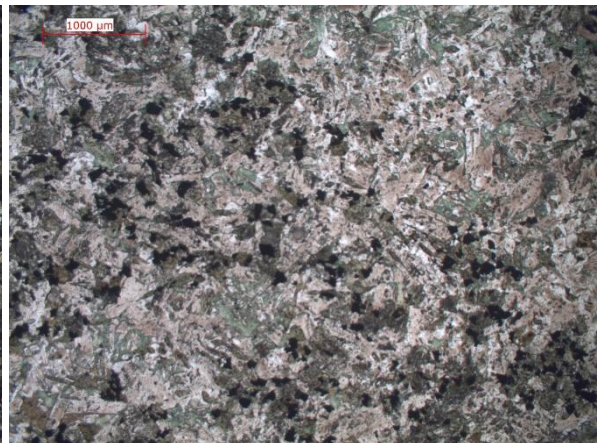
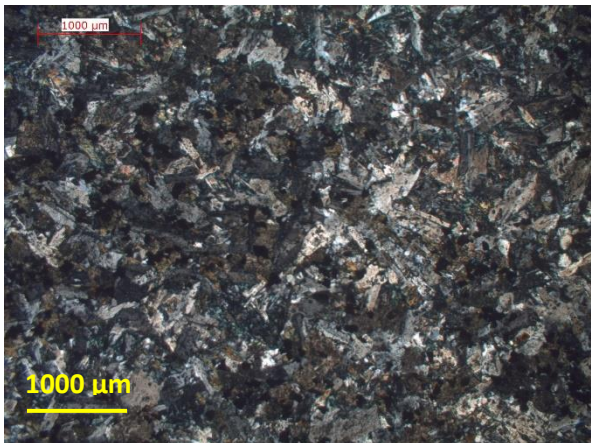


**VP16-25f Diorite**

**Hand specimen:** Medium grained phaneritic. Melanocratic, dark grey with a green tint.

**Thin section mineralogy:** Plagioclase, quartz, opaques, sericite/saussurite, epidote, chlorite.

**Texture and alteration:** Equigranular texture with mostly subhedral to anhedral minerals. Heavy alteration of feldspars to sericite and saussurite. Chlorite present in large amounts replacing an unidentified mineral and anhedral epidote grains occurs between feldspar grains or as inclusions.

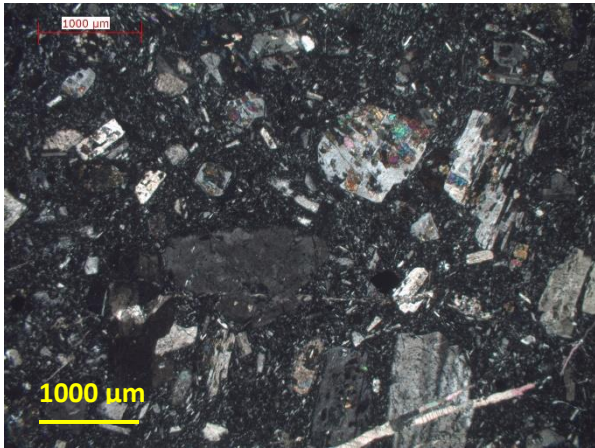


**VP16-25g Basalt**

**Hand specimen:** Fine grained aphanitic. Melanocratic that has a dark grey color with a green tint.

**Thin section mineralogy:** Plagioclase, chlorite, opaques, calcite, epidote, sericite/saussurite.

**Texture and alteration:** Equigranular texture with skeletal plagioclase laths. Tiny grains of epidote are commonly present. Chlorite occurs widespread over the whole sample and secondary calcite filled veins are common. Heavy alteration of plagioclase to sericite/saussurite.

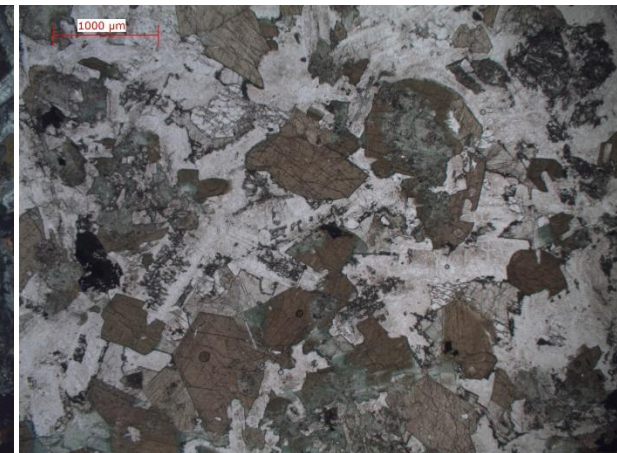
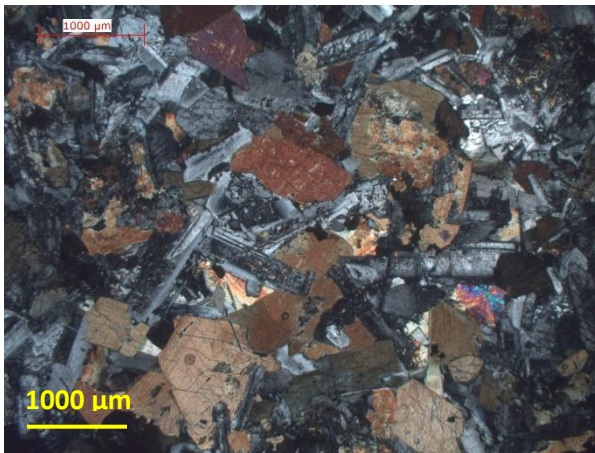


**VP16-26a Andesite**

**Hand specimen:** Medium grained porphyritic with an aphanitic groundmass. Melanocratic that has a dark grey matrix with light grey-pinkish phenocrysts.

**Thin section mineralogy:** Plagioclase and alkali-feldspar, opaques, calcite, epidote, sericite/saussurite.

**Texture and alteration:** Porphyritic with a trachytic matrix. The phenocrysts are primarily composed of feldspars and calcite in a groundmass of plagioclase microlites. Calcite aggregates and calcite filled veins are common. Heavy alteration of feldspars to sericite and saussurite.

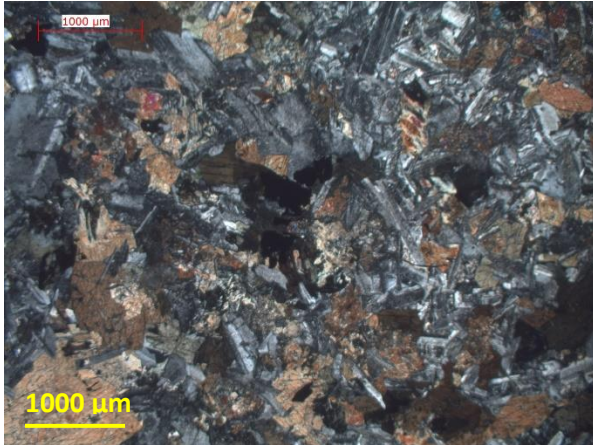


**VP16-26b Gabbro**

**Hand specimen:** Medium grained phaneritic. Melanocratic with a dark grey to light grey-green color.

**Thin section mineralogy:** Plagioclase, amphibole (hornblende and actinolite), opaques, pyroxene, epidote, chlorite, sericite.

**Texture and alteration:** Equigranular texture with randomly oriented plagioclase laths and subhedral primary hornblende. Pyroxenes have been completely replaced by amphibole. The feldspars have been slightly altered to sericite. Some of the hornblende grains are replaced by chlorite at the rims. Epidote occurs between larger plagioclase and hornblende crystals. Inclusions of plagioclase in hornblendes indicate that plagioclase was an earlier crystallizing face.

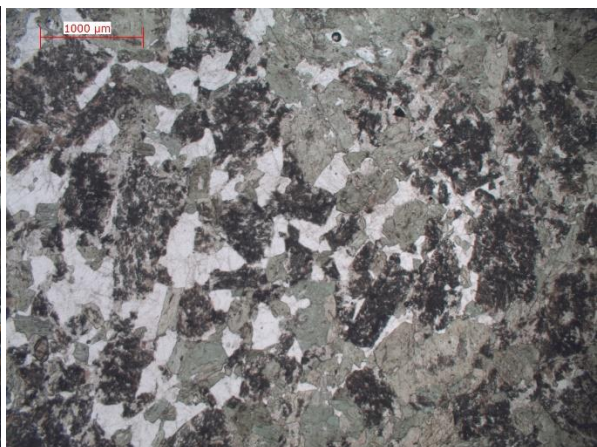
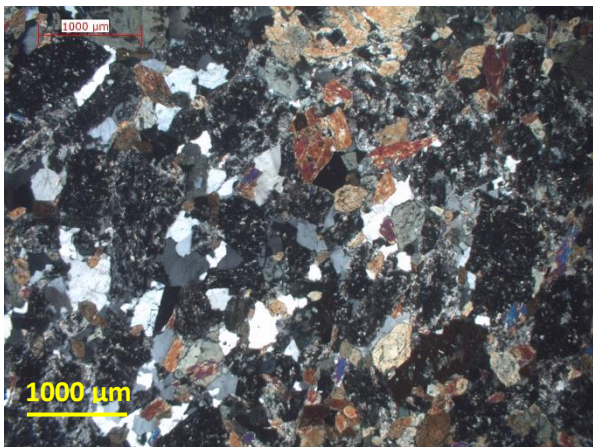


**VP16-26e Gabbro**

**Hand specimen:** Medium grained phaneritic. Melanocratic with a dark grey color, some light grey minerals present.

**Thin section mineralogy:** Plagioclase, amphibole (hornblende and actinolite), chlorite, pyroxene (CPX), opaques, sericite, titanite.

**Texture and alteration:** Equigranular texture with randomly oriented plagioclase laths partially enclosed by primary hornblende and pyroxene. Minor to moderately alteration of plagioclase to sericite. Hornblendes are being partly replaced by chlorite. Amphibole replacement of pyroxene - uralitization (not much pyroxene left).



**VP16-26f Diorite**

**Hand specimen:** Coarse grained phaneritic. Mesocratic, dark grey – white speckled sample.

**Thin section mineralogy:** Amphibole (hornblende and actinolite), plagioclase, quartz, pyroxene, chlorite, sericite, titanite, calcite.

**Texture and alteration:** Inequigranular texture with mostly anhedral mineral grains except from a few subhedral amphiboles. Mineralogy is dominated by amphibole, quartz and plagioclase. Heavy alteration of plagioclase to sericite. Pyroxene and hornblende have been nearly completely replaced by actinolite and chlorite. Polycrystalline quartz is common. Secondary vein filled with calcite is present.

## Appendix B. Analytical parameters and conditions

LA-ICP-MS analytical parameters.

<b>Laboratory &amp; Sample Preparation</b>	<b>U-Pb age analyses</b>
Laboratory name	PetroTectonic Facility, Department of Geological Sciences, Stockholm University
Sample type/mineral	Magmatic zircons
Sample preparation	Conventional mineral separation, c. 20 mm resin mount, c. 0.5 mm polish to finish
Imaging	Cathodoluminescence (CL) 15kV
<b>Laser ablation system</b>	
Make, Model & type	New Wave Research, 193 Excimer
Ablation cell & volume	2-volume cell
Laser wavelength	193 nm
Fluence	c. 7.0 J.cm <sup>-2</sup>
Repetition rate	10 Hz
Ablation duration	40 secs
Spot diameter	20 µm
Carrier gas	100% He in the cell, Ar make-up gas combined using a Y-piece 50% along the sample transport line to the torch.
<b>ICP-MS Instrument</b>	
Make, Model & type	Thermo Xseries II, Q-ICP-MS
Sample introduction	Ablation aerosol
Detection system	Secondary electron multiplier
Masses measured	202-207, 235, 238
<b>Data Processing</b>	
Gas blank	30 second on-peak zero subtracted
Calibration strategy	Plešovice used as primary reference material, FC-5z used as secondaries/validation.
Reference Material info	Plešovice (Sláma et al., 2008) FC-5z (Paces & Miller, 1993)
Data processing package used	Iolite VisualAge (Igor Pro)
Common-Pb correction, composition and uncertainty	No common-Pb correction applied to the data.
Quality control / Validation	Plešovice – Wtd ave <sup>206</sup> Pb/ <sup>238</sup> U age = 337 ± 1.3 Ma (95% confidence limit) FC-5z – Wtd ave <sup>206</sup> Pb/ <sup>238</sup> U age = 1088.6 ± 6.1 Ma (95% confidence limit)

## MC-ICP-MS and TIMS analytical parameters from Vegacenter (NRM).

### Instrument Setting

Mass spectrometer	Nu plasma (II) MC-ICP-MS
Introduction	Aridus II desolvator PFA nebulizer, ~100 $\mu$ L/min uptake rate
<i>Nebulizer gas</i>	35 psi
<i>Sweep gas</i>	~5.5 L/min
Cones	common Ni cones
Torch	glass
Measurement mode	2 blocks of 25 cycles, 10 sec/cycle sample consumption per single analysis: ~800 $\mu$ l , 25 ng Pb on-mass-zero measured for 60sec in 0.3M HNO <sub>3</sub> at the beginning of each sequence washout time: 100 sec transfer time: 80 sec
Sensitivity (total Pb)	~370 V/ppm samples measured at ~30 ppb in 0.3M HNO <sub>3</sub> +10 ppb Tl spike

### Accuracy and external reproducibility

for Pb-isotopes on the NuPlasmas + Aridus II (Vegacenter, NRM) based on repeated analyses (n = 12) of the standard solution **NBS981** (errors in brackets are 2 $\sigma$ )

	<sup>206</sup> Pb/ <sup>204</sup> Pb	<sup>207</sup> Pb/ <sup>204</sup> Pb	<sup>208</sup> Pb/ <sup>204</sup> Pb	<sup>207</sup> Pb/ <sup>206</sup> Pb	<sup>208</sup> Pb/ <sup>206</sup> Pb
<b>Vegacenter</b>	<b>16.9356 (53)</b>	<b>15.4891 (43)</b>	<b>36.701 (15)</b>	<b>0.91459 (21)</b>	<b>2.16701 (82)</b>
<i>Todt et al. (1996)</i> <i>(double spike)</i>	<i>16.9356 (07)</i>	<i>15.4891 (09)</i>	<i>36.701 (03)</i>	<i>0.91459 (04)</i>	<i>2.16701 (13)</i>

LIG#	Sample	C <sub>Sm</sub> (ppm)	C <sub>Nd</sub> (ppm)	<sup>147</sup> Sm/ <sup>144</sup> Nd	<sup>143</sup> Nd/ <sup>144</sup> Nd	Int. prec. 2σm	<sup>145</sup> Nd/ <sup>144</sup> Nd	<sup>143</sup> Nd/ <sup>144</sup> Nd norm. *	Ext. prec. 2σ	ε Nd (T <sub>0</sub> ) norm. *	T <sub>DM</sub> (Ga)
17056	VP15-10	4.736	16.68	0.1716	0.5128439	0.0000026	0.3484176	0.512830	0.000009	3.75	0.79
17057	VP15-13	3.912	12.61	0.1876	0.5129649	0.0000026	0.3484161	0.512951	0.000009	6.11	0.60
17058	VP16-22a	4.818	17.26	0.1687	0.5129118	0.0000030	0.3484169	0.512898	0.000009	5.07	0.53
17059	VP16-22c	1.545	3.878	0.2409	0.5130991	0.0000050	0.3484154	0.513085	0.000009	8.72	0.08
17060	VP16-23a	3.266	9.821	0.2010	0.5131021	0.0000018	0.3484149	0.513088	0.000009	8.78	-
17061	VP16-23g	3.546	13.78	0.1555	0.5130445	0.0000032	0.3484240	0.513030	0.000009	7.65	0.10
17062	VP16-24a	2.207	7.159	0.1863	0.5130894	0.0000018	0.3484173	0.513075	0.000009	8.52	-
17063	VP16-24b	3.195	10.94	0.1765	0.5131058	0.0000037	0.3484235	0.513092	0.000009	8.86	-
17064	VP16-24d	1.748	6.211	0.1701	0.5130677	0.0000037	0.3484197	0.513054	0.000009	8.11	0.06
17065	VP16-25d	2.296	12.55	0.1106	0.5129378	0.0000028	0.3484129	0.512924	0.000009	5.58	0.21
17066	VP16-26b	3.370	10.89	0.1871	0.5130777	0.0000021	0.3484169	0.513064	0.000009	8.31	0.05
17067	VP16-26f	1.157	4.047	0.1728	0.5130903	0.0000036	0.3484164	0.513076	0.000009	8.54	-
-	BCR-2	6.521	28.12	0.1402	0.5126523	0.0000038	0.3484125	0.512638	0.000009	0.00	0.85

T=0 Depleted mantle age calculated according to DePaolo (Nature 291, 1981)

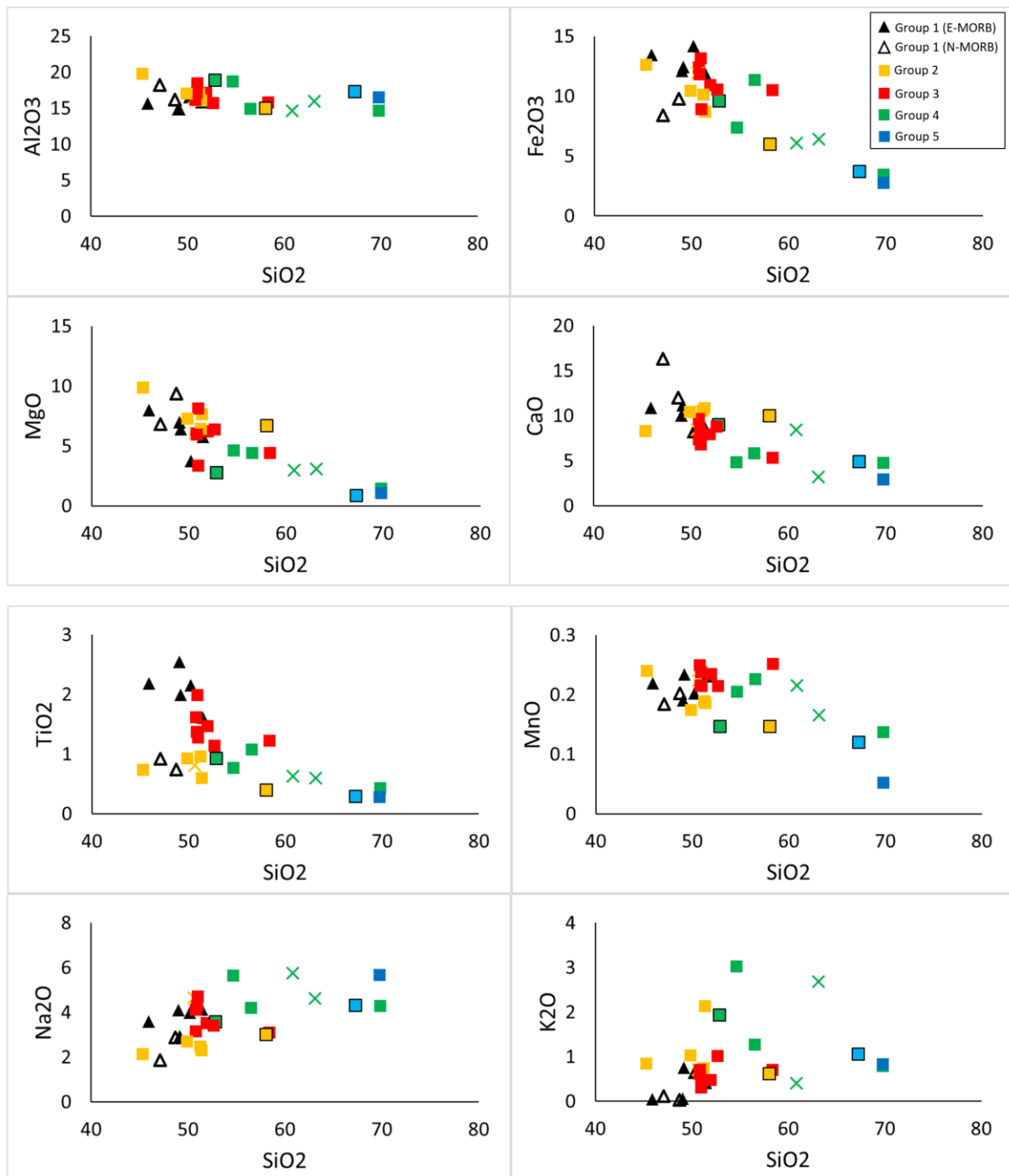
The samples were analysed on a Thermo Scientific TRITON TIMS using total spiking with a mixed <sup>149</sup>Sm/<sup>150</sup>Nd spike. Concentrations and ratios were reduced assuming exponential fractionation. Samarium concentrations were determined in multicollector static mode on rhenium double filaments. Samarium ratios were normalised to <sup>147</sup>Sm/<sup>148</sup>Sm = 1.33386. Neodymium was run in static mode on double rhenium filaments using rotating gain compensation. Calculated ratios were normalised to <sup>146</sup>Nd/<sup>144</sup>Nd = 0.7219. The external precision for <sup>143</sup>Nd/<sup>144</sup>Nd as judged from values for La Jolla standard was 18 ppm.

\* Accuracy correction was applied since the mean <sup>143</sup>Nd/<sup>144</sup>Nd ratio was 0.511867±09 (n=12). Consequently, measured <sup>143</sup>Nd/<sup>144</sup>Nd ratios have been brought in accordance with reference standard measurements by subtraction of 0.3 epsilon units.

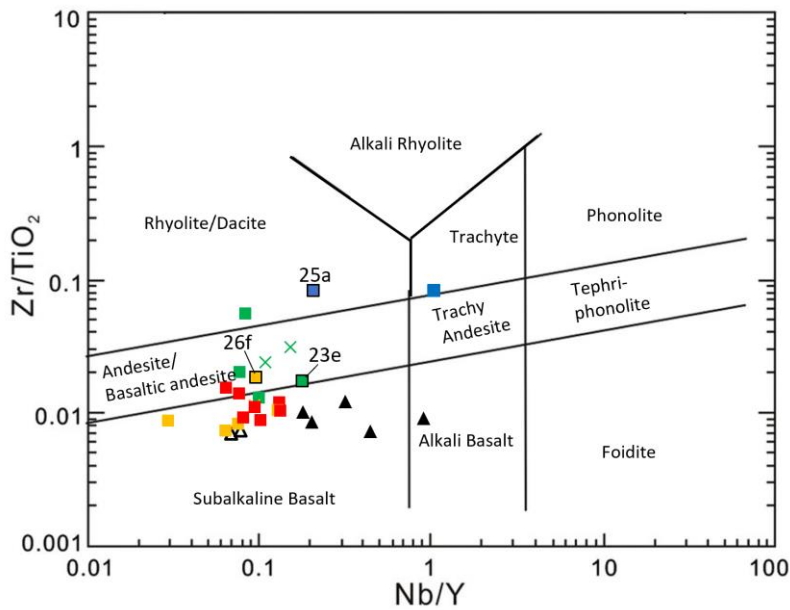
The column blank was recorded to be 0.15 ng.

## Appendix C. Bivariate and rock classification-diagrams

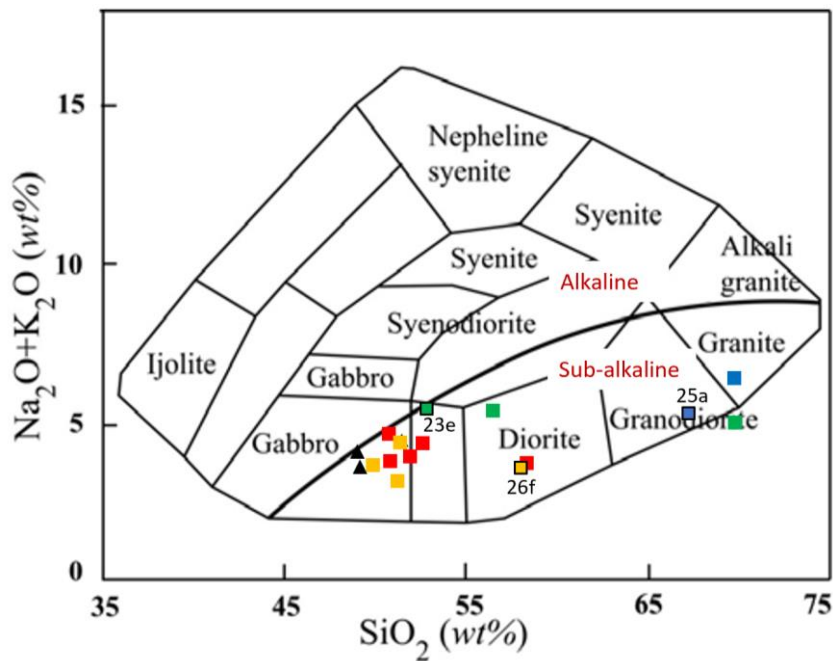
Bivariate diagrams of major oxides plotted against SiO<sub>2</sub>.



Zr/TiO<sub>2</sub> vs Nb/Y classification diagram for altered igneous rocks by Winchester & Floyd (1977). All samples included (volcanic, hypabyssal and plutonic).



Total alkalis versus silica (TAS) classification diagram of plutonic rocks of Cox et al. (1979) adapted by Wilson (1989). The curved solid line divides the sub-alkaline field from the alkaline. Note that only intrusive samples (hypabyssal and plutonic) are included.



## Appendix D. U-Pb data table

Identifier	cPb <sup>1</sup>	U (µg g <sup>-1</sup> )	Pb (µg g <sup>-1</sup> )	Th (µg g <sup>-1</sup> )	U/Th	Data for Tera-Wasserburg plot <sup>2</sup>				Data for Wetherill plot <sup>2</sup>				Dates <sup>2</sup>					% conc <sup>3</sup>		
						<sup>238</sup> U/ <sup>206</sup> Pb	±2SE	<sup>207</sup> Pb/ <sup>206</sup> Pb	±2SE	<sup>207</sup> Pb/ <sup>235</sup> U	±2SE	<sup>206</sup> Pb/ <sup>238</sup> U	±2SE	Rho	<sup>206</sup> Pb/ <sup>238</sup> U	±2SE	<sup>207</sup> Pb/ <sup>235</sup> U	±2SE		<sup>207</sup> Pb/ <sup>206</sup> Pb	±2SE
VP16-23e-1	no	993	97	303	3.0	29.45	0.67	0.0498	0.0025	0.2313	0.0082	0.0340	0.0008	0.536	215	5	211	7	180	110	102
VP16-23e-6	no	539	49	152	3.0	30.17	0.66	0.0489	0.0032	0.2230	0.0130	0.0332	0.0007	0.114	210	5	205	11	130	130	103
VP16-23e-9	no	555	63	174	2.0	28.70	0.77	0.0473	0.0036	0.2320	0.0150	0.0348	0.0009	0.101	221	6	211	12	90	150	105
VP16-23e-17	no	453	57	149	2.0	28.99	1.09	0.0493	0.0034	0.2360	0.0140	0.0345	0.0013	0.310	219	8	215	12	160	140	102
VP16-23e-18	no	63	23	66	1.0	29.76	1.59	0.0504	0.0092	0.2240	0.0390	0.0336	0.0018	0.023	213	12	204	33	230	320	104
VP16-23e-19	no	822	131	367	2.0	29.50	0.96	0.0507	0.0028	0.2360	0.0120	0.0339	0.0011	0.696	215	7	217	9	210	110	99
VP16-23e-36	no	359	44	155	2.0	29.35	0.72	0.0503	0.0039	0.2390	0.0160	0.0341	0.0008	0.000	216	5	216	13	220	150	100
VP16-23e-37	no	755	74	261	2.0	29.36	0.66	0.0493	0.0030	0.2330	0.0110	0.0341	0.0008	0.237	216	5	212	9	150	120	102
VP16-23e-38	no	355	31	119	3.0	31.23	0.75	0.0466	0.0035	0.2100	0.0150	0.0320	0.0008	0.348	204	5	192	13	90	150	106
VP16-23e-39	no	698	72	269	2.0	29.74	0.70	0.0507	0.0033	0.2360	0.0120	0.0336	0.0008	0.059	213	5	214	10	240	140	100
VP16-23e-45	no	407	42	147	2.0	30.40	0.73	0.0505	0.0039	0.2280	0.0150	0.0329	0.0008	0.187	209	5	208	13	220	160	100
VP16-23e-46	no	228	26	91	3.0	28.09	1.18	0.0492	0.0064	0.2460	0.0300	0.0356	0.0015	0.032	226	9	221	25	190	250	102
VP16-23e-52	no	134	19	56	4.0	29.67	1.58	0.0508	0.0052	0.2320	0.0230	0.0337	0.0018	0.467	214	11	211	19	260	220	101
VP16-23e-54	no	144	41	120	2.0	29.99	0.85	0.0469	0.0042	0.2180	0.0160	0.0334	0.0009	0.132	212	6	199	14	50	170	106
VP16-25a-1*	no	491	15	44	12.0	32.79	1.93	0.0483	0.0064	0.2050	0.0250	0.0305	0.0018	0.423	194	11	188	21	100	240	103
VP16-25a-4*	no	813	20	66	12.0	32.57	1.17	0.0508	0.0051	0.2200	0.0220	0.0307	0.0011	0.128	195	7	201	18	250	180	97
VP16-25a-5*	no	567	23	58	10.0	32.68	1.39	0.0525	0.0073	0.2290	0.0260	0.0306	0.0013	0.043	194	8	208	21	300	280	93
VP16-25a-9*	no	625	14	38	14.0	32.36	1.68	0.0513	0.0075	0.2240	0.0300	0.0309	0.0016	0.547	196	10	204	25	270	300	96
VP16-25a-11*	no	424	16	41	9.0	34.36	1.65	0.0490	0.0061	0.2000	0.0260	0.0291	0.0014	0.282	185	9	184	22	160	240	101
VP16-25a-1	no	881	24	464	12.0	32.36	1.26	0.0555	0.0042	0.2380	0.0220	0.0309	0.0012	0.503	196	7	216	17	500	160	91
VP16-25a-2	no	968	25	432	11.0	33.01	0.68	0.0509	0.0037	0.2140	0.0170	0.0303	0.0006	0.480	192	4	196	14	210	140	98
VP16-25a-4	no	703	21	164	10.0	33.48	0.67	0.0525	0.0030	0.2130	0.0120	0.0299	0.0006	0.091	190	4	196	11	310	120	97
VP16-25a-5	no	2112	48	376	12.0	32.96	0.95	0.0523	0.0024	0.2190	0.0098	0.0303	0.0009	0.255	193	5	201	8	286	96	96
VP16-25a-6	no	829	12	85	19.0	33.78	1.37	0.0512	0.0035	0.2110	0.0170	0.0296	0.0012	0.323	188	7	194	15	230	140	97
VP16-25a-10	no	1684	68	289	7.0	33.90	1.72	0.0505	0.0037	0.2080	0.0360	0.0295	0.0015	0.161	187	9	192	26	200	140	98
VP16-25a-16	no	1686	25	71	19.0	33.33	2.56	0.0540	0.0048	0.2270	0.0240	0.0300	0.0023	0.201	190	14	207	19	330	180	92
VP16-25a-17	no	2096	46	141	13.0	33.08	0.84	0.0492	0.0023	0.2121	0.0099	0.0302	0.0008	0.241	192	5	195	8	156	98	98
VP16-25a-19	no	1307	31	102	13.0	32.03	0.82	0.0492	0.0027	0.2230	0.0100	0.0312	0.0008	0.031	198	5	204	9	190	120	97
VP16-25a-25	no	322	19	137	4.0	32.50	0.68	0.0470	0.0045	0.2100	0.0190	0.0308	0.0006	0.012	195	4	192	16	110	180	102
VP16-25a-26	no	825	30	207	7.0	32.56	0.86	0.0517	0.0023	0.2191	0.0097	0.0307	0.0008	0.703	195	5	201	8	277	93	97
VP16-25a-33	no	2318	60	398	9.0	32.89	1.41	0.0502	0.0026	0.2190	0.0120	0.0304	0.0013	0.111	193	8	201	10	220	110	96
VP16-25a-7*	no	1050	21	63	15.0	31.25	1.37	0.0533	0.0041	0.2340	0.0160	0.0320	0.0014	0.266	203	9	213	14	310	160	95
VP16-25a-34	no	774	24	167	7.0	34.25	1.02	0.0521	0.0037	0.2120	0.0150	0.0292	0.0009	0.055	186	6	198	12	260	140	94
VP16-25a-35	no	1511	38	251	8.0	34.55	0.92	0.0494	0.0021	0.2030	0.0110	0.0289	0.0008	0.432	184	5	187	9	162	97	98
VP16-25a-21	no	878	16	55	15.0	33.78	0.56	0.0483	0.0029	0.2050	0.0120	0.0296	0.0005	0.029	188	3	191	10	120	120	99
VP16-25a-12	no	393	24	80	5.0	34.97	1.83	0.0518	0.0061	0.2050	0.0390	0.0286	0.0015	0.196	182	9	188	30	240	220	97
VP16-25a-27	no	1105	25	205	9.0	33.98	0.76	0.0518	0.0038	0.2200	0.0150	0.0294	0.0007	0.199	187	4	205	12	300	150	91
VP16-25a-29	no	977	17	130	12.0	29.85	2.32	0.0518	0.0042	0.2520	0.0240	0.0335	0.0026	0.172	213	16	228	19	260	160	93
VP16-25a-36	no	835	32	146	9.0	31.54	0.50	0.0510	0.0020	0.2225	0.0070	0.0317	0.0005	0.492	201	3	204	6	224	85	99
VP16-25a-3	no	745	16	192	12.0	30.21	1.46	0.0555	0.0060	0.2450	0.0240	0.0331	0.0016	0.279	210	10	221	19	430	240	95
VP16-25a-11	no	882	29	116	8.0	36.05	0.74	0.0522	0.0030	0.1990	0.0130	0.0277	0.0006	0.086	176	4	184	11	280	120	96
VP16-25a-28	no	1093	19	143	13.0	30.93	0.84	0.0478	0.0026	0.2260	0.0140	0.0323	0.0009	0.049	205	6	207	11	100	110	99

\* Data from mount 1 (analysed 051118), other data are from mount 2 (analysed 301118).

<sup>1</sup> Common lead concentration were calculated by using the 202Hg/204Hg natural ratio, and then subtracting the 204Hg from the measured mass 204.

No cPb= 204Pb < 100 cps and Pb/Hg\*100 < 25.

<sup>2</sup> Data not corrected for common lead.

<sup>3</sup> Concordance calculated as (206Pb-238U age/207Pb-235U age)\*100.

*Analyses written in italics have been excluded from final (concordia) age determination.*

Identifier	cPb <sup>1</sup>	U (µg g <sup>-1</sup> )	Pb (µg g <sup>-1</sup> )	Th (µg g <sup>-1</sup> )	U/Th	Data for Tera-Wasserburg plot <sup>2</sup>				Data for Wetherill plot <sup>2</sup>				Dates <sup>2</sup>					% conc <sup>3</sup>		
						<sup>238</sup> U/ <sup>206</sup> Pb	±2SE	<sup>207</sup> Pb/ <sup>206</sup> Pb	±2SE	<sup>207</sup> Pb/ <sup>235</sup> U	±2SE	<sup>206</sup> Pb/ <sup>238</sup> U	±2SE	Rho	<sup>206</sup> Pb/ <sup>238</sup> U	±2SE	<sup>207</sup> Pb/ <sup>235</sup> U	±2SE		<sup>207</sup> Pb/ <sup>206</sup> Pb	±2SE
VP16-26f-13*	no	232	12	31	6.0	34.13	1.40	0.0522	0.0096	0.2150	0.0340	0.0293	0.0012	0.231	188	8	195	29	330	330	96
VP16-26f-2*	no	332	13	35	5.0	33.33	1.56	0.0546	0.0073	0.2210	0.0360	0.0300	0.0014	0.430	191	9	206	27	310	250	92
VP16-26f-14*	no	818	74	263	3.0	33.33	1.22	0.0536	0.0048	0.2160	0.0180	0.0300	0.0011	0.059	191	7	202	16	310	190	94
VP16-26f-1*	no	286	26	75	3.0	33.22	1.88	0.0547	0.0066	0.2190	0.0300	0.0301	0.0017	0.508	191	11	198	25	310	230	96
VP16-26f-35*	no	159	20	71	3.0	33.22	2.10	0.0538	0.0082	0.2240	0.0340	0.0301	0.0019	0.033	191	12	203	28	340	310	94
VP16-26f-11*	no	344	17	43	4.0	33.00	1.42	0.0483	0.0068	0.2110	0.0310	0.0303	0.0013	0.016	192	8	193	26	160	260	100
VP16-26f-30*	no	352	40	138	3.0	33.00	1.09	0.0471	0.0065	0.2040	0.0300	0.0303	0.0010	0.109	193	7	187	25	50	250	103
VP16-26f-26*	no	442	18	79	7.0	33.00	2.18	0.0511	0.0081	0.2190	0.0340	0.0303	0.0020	0.413	193	12	199	28	190	300	97
VP16-26f-25*	no	275	16	50	7.0	32.79	1.61	0.0551	0.0092	0.2240	0.0340	0.0305	0.0015	0.054	194	10	204	28	320	330	95
VP16-26f-29*	no	445	50	159	4.0	32.82	1.06	0.0470	0.0081	0.2090	0.0360	0.0305	0.0010	0.052	194	6	197	28	110	320	98
VP16-26f-21*	no	274	13	51	6.0	32.79	1.83	0.0514	0.0091	0.2130	0.0380	0.0305	0.0017	0.516	194	10	194	31	170	310	100
VP16-26f-6*	no	447	17	44	5.0	32.47	2.32	0.0518	0.0083	0.2150	0.0360	0.0308	0.0022	0.422	195	14	196	29	220	300	99
VP16-26f-8*	no	302	17	42	3.0	32.26	1.14	0.0453	0.0064	0.2020	0.0200	0.0310	0.0011	0.334	197	7	186	17	60	210	106
VP16-26f-42*	no	286	19	71	5.0	31.95	1.63	0.0530	0.0079	0.2300	0.0350	0.0313	0.0016	0.134	199	10	208	30	280	300	96
VP16-26f-33*	no	406	26	86	6.0	31.55	1.09	0.0533	0.0056	0.2220	0.0210	0.0317	0.0011	0.100	201	7	207	19	280	210	97
VP16-26f-4*	no	331	26	65	3.0	31.25	1.86	0.0554	0.0066	0.2330	0.0300	0.0320	0.0019	0.162	203	12	211	24	360	240	96
VP16-26f-27*	no	254	18	69	5.0	31.25	1.86	0.0564	0.0084	0.2470	0.0370	0.0320	0.0019	0.075	203	12	221	30	460	320	92
VP16-26f-12*	no	721	31	75	4.0	31.25	1.17	0.0495	0.0049	0.2240	0.0200	0.0320	0.0012	0.571	203	8	205	16	160	190	99
VP16-26f-38*	no	1189	62	257	5.0	30.21	2.10	0.0509	0.0055	0.2280	0.0240	0.0331	0.0023	0.057	210	14	207	20	210	210	101
VP16-26f-3	no	733	49	94	5.0	32.36	1.26	0.0555	0.0073	0.2350	0.0260	0.0309	0.0012	0.001	196	8	214	22	420	250	92
VP16-26f-9	no	229	31	77	2.0	32.36	1.05	0.0552	0.0058	0.2240	0.0230	0.0309	0.0010	0.042	196	7	203	19	360	210	97
VP16-26f-10	no	334	14	34	6.0	32.31	0.68	0.0497	0.0037	0.2120	0.0170	0.0310	0.0007	0.621	197	4	194	14	150	160	101
VP16-26f-11	no	382	49	105	2.0	31.55	1.09	0.0584	0.0076	0.2400	0.0450	0.0317	0.0011	0.317	201	7	217	29	510	240	93
VP16-26f-13	no	204	20	48	3.0	33.42	0.99	0.0546	0.0065	0.2210	0.0260	0.0299	0.0009	0.071	190	6	201	21	370	220	95
VP16-26f-17	no	223	29	82	2.0	31.95	1.22	0.0521	0.0091	0.2290	0.0410	0.0313	0.0012	0.166	199	8	206	34	350	300	97
VP16-26f-18	no	619	57	188	3.0	33.43	1.02	0.0517	0.0036	0.2170	0.0130	0.0299	0.0009	0.215	190	6	199	11	290	140	95
VP16-26f-19	no	294	23	67	4.0	31.45	1.29	0.0555	0.0075	0.2340	0.0350	0.0318	0.0013	0.034	202	8	217	31	370	280	93
VP16-26f-20	no	587	71	244	2.0	32.50	0.87	0.0498	0.0035	0.2180	0.0140	0.0308	0.0008	0.187	195	5	200	12	180	140	98
VP16-26f-22	no	219	16	64	4.0	31.73	0.87	0.0503	0.0051	0.2200	0.0220	0.0315	0.0009	0.087	200	5	205	17	190	200	98
VP16-26f-24	no	277	28	120	2.0	32.80	0.86	0.0495	0.0054	0.2110	0.0240	0.0305	0.0008	0.000	194	5	193	20	150	200	100
VP16-26f-25	no	313	23	99	4.0	31.55	1.29	0.0466	0.0049	0.2140	0.0210	0.0317	0.0013	0.141	201	8	196	18	50	190	103
VP16-26f-26	no	71	9	32	2.0	31.15	1.16	0.0520	0.0130	0.2510	0.0520	0.0321	0.0012	0.108	203	8	221	41	420	330	92
VP16-26f-30	no	317	15	54	5.0	31.75	1.11	0.0499	0.0054	0.2220	0.0240	0.0315	0.0011	0.151	200	7	203	20	170	200	99
VP16-26f-31	no	129	14	53	2.0	32.79	1.18	0.0460	0.0051	0.2010	0.0250	0.0305	0.0011	0.187	194	7	184	21	20	210	105
VP16-26f-33	no	1369	101	499	3.0	31.06	1.25	0.0495	0.0035	0.2310	0.0150	0.0322	0.0013	0.177	204	8	210	12	160	150	97
VP16-26f-34	no	301	13	48	5.0	33.33	1.67	0.0500	0.0110	0.2200	0.0430	0.0300	0.0015	0.119	191	9	207	35	280	390	92
VP16-26f-35	no	345	43	172	2.0	32.05	1.13	0.0437	0.0056	0.1980	0.0240	0.0312	0.0011	0.083	198	7	182	21	-70	220	109
VP16-26f-39	no	153	13	83	4.0	32.47	1.05	0.0522	0.0090	0.2260	0.0420	0.0308	0.0010	0.493	196	6	215	35	270	290	91
VP16-26f-42	no	119	11	112	3.0	32.65	1.06	0.0493	0.0045	0.2160	0.0200	0.0306	0.0010	0.257	194	6	198	16	130	170	98
VP16-26f-48	no	504	24	419	6.0	33.05	1.04	0.0498	0.0043	0.2100	0.0180	0.0303	0.0010	0.013	192	6	193	15	170	170	100
VP16-26f-37	no	183	19	324	3.0	32.35	1.04	0.0482	0.0057	0.2090	0.0250	0.0309	0.0010	0.124	196	6	190	21	130	220	103
VP16-26f-43	no	163	9	98	5.0	33.33	1.22	0.0476	0.0062	0.1990	0.0250	0.0300	0.0011	0.162	190	7	182	21	60	230	105
VP16-26f-38	no	437	56	412	3.0	33.03	0.91	0.0468	0.0041	0.2040	0.0140	0.0303	0.0008	0.200	192	5	190	13	60	160	101
VP16-26f-15	no	351	17	56	5.0	33.67	1.25	0.0536	0.0049	0.2130	0.0160	0.0297	0.0011	0.215	189	7	195	14	390	180	97
VP16-26f-34*	no	327	17	65	6.0	34.25	1.64	0.0484	0.0085	0.2070	0.0380	0.0292	0.0014	0.158	186	9	188	32	190	350	99
VP16-26f-32	no	194	13	53	3.0	33.19	0.76	0.0510	0.0047	0.2220	0.0190	0.0301	0.0007	0.137	191	4	202	16	200	180	95
VP16-26f-5*	no	574	74	170	2.0	34.13	1.40	0.0525	0.0031	0.1980	0.0150	0.0293	0.0013	0.489	186	8	190	13	300	130	98
VP16-26f-46	no	234	34	439	3.0	31.25	0.98	0.0538	0.0056	0.2460	0.0280	0.0320	0.0010	0.056	203	6	221	22	380	200	92
VP16-26f-45	no	801	139	2200	2.0	33.42	0.68	0.0468	0.0027	0.2030	0.0130	0.0299	0.0006	0.285	190	4	187	11	50	110	102
VP16-26f-16	no	276	28	89	3.0	34.04	1.07	0.0503	0.0043	0.2030	0.0170	0.0294	0.0009	0.051	187	6	186	14	180	170	100
VP16-26f-36	no	177	12	37	4.0	34.72	1.81	0.0500	0.0085	0.2130	0.0380	0.0288	0.0015	0.234	183	10	194	30	210	280	94
VP16-26f-7*	no	267	17	49	4.0	30.40	1.66	0.0500	0.0058	0.2270	0.0340	0.0329	0.0018	0.718	209	11	205	28	210	230	102
VP16-26f-28*	no	562	67	272	3.0	30.21	1.46	0.0458	0.0070	0.2150	0.0290	0.0331	0.0016	0.268	210	10	196	24	60	280	107
VP16-26f-8	no	1075	61	147	4.0	31.12	0.84	0.0528	0.0024	0.2290	0.0100	0.0321	0.0009	0.750	204	5	209	8	300	110	98
VP16-26f-23	no	655	76	310	2.0	30.40	1.48	0.0501	0.0044	0.2290	0.0270	0.0329	0.0016	0.347	209	10	213	24	180	170	98
VP16-26f-47	no	193	18	302	3.0	30.49	1.30	0.0472	0.0067	0.2160	0.0310	0.0328	0.0014	0.204	208	8	197	25	30	270	106
VP16-26f-17*	no	755	58	212	4.0	35.01	1.02	0.0538	0.0042	0.2050	0.0200	0.0286	0.0008	0.470	182	5	192	17	330	160	95
VP16-26f-39*	no	346	15	57	7.0	34.84	1.94	0.0546	0.0069	0.2170	0.0260	0.0287	0.0016	0.462	182	10	197	22	370	240	93
VP16-26f-3*	no	705	90	194	2.0	29.59	1.40														

